Materialwissenschaft

Daniel Dickes

Oxide layer and diffusion zone formation during oxidation of Ti6Al4V and TiZrNbHfTa and their influence on tribological properties

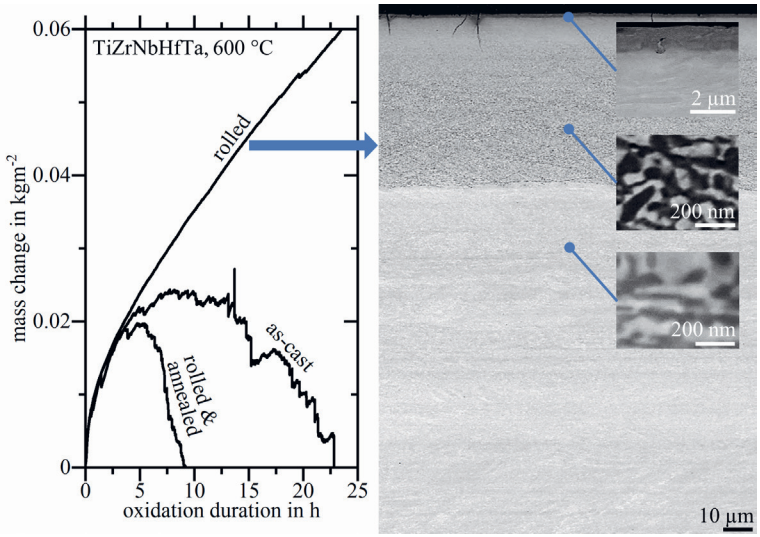

SHAKER VERLAG

Oxide layer and diffusion zone formation during oxidation of Ti6Al4V and TiZrNbHfTa and their influence on tribological properties

Von der Fakultät für Ingenieurwissenschaften

der Universität Bayreuth

zur Erlangung der Würde eines

Doktor-Ingenieur (Dr.-Ing.)

genehmigte Dissertation

von

M. Sc. Daniel Dickes

aus

Mannheim

Erstgutachter: Prof. Dr.-Ing. Uwe Glatzel

Zweitgutachter: PD Dr.-Ing. Mathias Galetz

Tag der mündlichen Prüfung: 16.08.2023

Lehrstuhl Metallische Werkstoffe

Universität Bayreuth

2023

Berichte aus der Materialwissenschaft

Daniel Dickes

Oxide layer and diffusion zone formation during oxidation of Ti6Al4V and TiZrNbHfTa and their influence on tribological properties

Shaker Verlag
Düren 2023

Bibliographic information published by the Deutsche Nationalbibliothek
The Deutsche Nationalbibliothek lists this publication in the Deutsche Nationalbibliografie; detailed bibliographic data are available in the Internet at http://dnb.d-nb.de.

Zugl.: Bayreuth, Univ., Diss., 2023

Printed in Germany.

ISBN 978-3-8440-9293-6
ISSN 1618-5722

Shaker Verlag GmbH • Am Langen Graben 15a • 52353 Düren
Phone: 0049/2421/99011-0 • Telefax: 0049/2421/99011-9
Internet: www.shaker.de • e-mail: info@shaker.de

Preface

"By the time one has finished the last chapter, one can always start anew on earlier chapters in order to keep the information up to date. In this respect the writing is a Sisyphean labour. But, on the more positive side, one continually learns by writing"

Per Kofstadt, Norwegian researcher on high temperature corrosion, in his book "High temperature corrosion", Elsevier, 1988.

Table of contents

List of abbreviations

Abbreviations

APT	atom probe tomography
bcc	body-centered cubic
BSE	backscattered electron
EPMA	electron probe micro analyzer
EDS	energy dispersive X-ray spectroscopy
GDOES	glow discharge optical emission spectrometry
hcp	hexagonal close-packed
HEA	high entropy alloy / high entropy alloys
HM	Martens hardness
ICDD	international center for diffraction data
NRA	nuclear reaction analysis
OECD	organization for economic co-operation and development
OEZ	oxygen-enriched zone
SE	secondary electron
SEM	scanning electron microscope
UHMW-PE	ultra-high-molecular-weight polyethylene
XPS	X-ray photoelectron spectroscopy
XRD	X-ray diffraction analysis
XRF	µX-ray fluorescence analysis

1 Motivation

In their health report [1], the organization for economic co-operation and development (OECD) outlines that life expectancy has continuously increased over the past five decades, being 81 years for a person born in 2019 averaged over all 38 OECD countries. In line with the increasing life expectancy and medical progress, the average number of hip and knee replacement surgeries has increased [1]. In 2021, 172 thousand artificial knee joints were implanted solely in Germany [2]. Amongst these implant recipients, 36 thousand were younger than 60 years [3]. Thus, given the increasing life expectancy, the required service life time of a joint implant has to reach more than 20 years. Such a required long service life is a major challenge since a relative movement between the knee joint components, the femur and the tibia part, occurs during each human step cycle. This relative movement results in wear of the knee joint, with wear being defined as a process of material removal from solid surfaces due to mechanical, thermal, or chemical action [4]. The consequence of accumulated wear over time is damage to the knee joint and the need to replace it. This has to be avoided. Therefore, there is a strong interest in improving the wear behavior of existing implant materials and developing new implant materials.

Titanium alloys are often the implant material of choice due to their excellent corrosion resistance and biocompatibility, a low Young's modulus as required for implants, and high fatigue strength [5]. Popular alloys are commercially pure α-titanium and the α+β-alloy Ti6Al4V [5]. However, these alloys are prone to wear [6–8]. A promising approach to overcome this drawback is oxidation-induced surface hardening. In a previous work at the Metals & Alloys chair, University of Bayreuth, oxidation processes could successfully improve the wear behavior of a ZrNb7 alloy which, similar to titanium alloys, has a high oxygen solubility [9]. During oxidation, a high oxygen solubility allows an oxygen diffusion zone to form underneath a hard oxide layer. Such an oxygen diffusion zone is associated with a gradual hardness decrease towards the substrate. This work aims to investigate the applicability of the previously studied oxidation processes to Ti6Al4V and to understand their influence on tribological properties.

To further adapt the Young's modulus to the one of the human bone, new alloy concepts such as β-titanium alloys like Ti35Nb7Zr5Ta [10] or the high entropy alloy TiZrNbHfTa (20 at.% per element) [11, 12] are in discussion as biocompatible implant materials. With Ti, Zr, and Hf, the high entropy alloy TiZrNbHfTa contains three elements that possess a high oxygen solubility [13–17]. Therefore, TiZrNbHfTa is a promising material for oxidation-induced surface hardening. As for Ti6Al4V, a hard surface oxide layer and a beneath oxygen diffusion zone are expected to form during oxidation, resulting in a gradual hardness decrease from the surface oxide layer towards the substrate. Yet, the oxidation behavior of TiZrNbHfTa is poorly understood. Currently, only catastrophic oxidation, causing deteriorated surfaces, has been observed [18]. This work aims to provide a mechanism describing the oxidation behavior of TiZrNbHfTa. In addition, this work aspires to establish oxidation processes for TiZrNbHfTa that lead to a hard, adherent oxide layer with improved tribological properties.

2 Introduction and state of research

2.1 Tribology

Tribology is the research field covering the interaction of surfaces in relative motion. This includes the study of friction, wear, and lubrication. Friction describes the resistance against a relative motion of two bodies, which a lubricant may reduce. Under dry conditions, friction is quantified by the coefficient of friction μ, defined as the ratio of tangential friction force F_t opposite to the direction of relative motion and the normal force F_n acting between two bodies. [4]

$$\mu = \frac{F_t}{F_n} \tag{1}$$

μ: *coefficient of friction*
F_n: *normal force acting between two bodies*
F_t: *tangential friction force opposite to the direction of relative motion of two bodies*

Wear describes the continuous deterioration of the surface of a body through material loss, in this case, caused by mechanical action [4, 19]. Table 1 lists different wear mechanisms causing such a material loss. The most crucial wear mechanisms are adhesion, abrasion, and corrosion [19]. Together, they make up 80 % of the wear loss encountered for engineering components [19].

Table 1: Mechanisms of wear and their definition according to Menezes et al. [4].

mechanisms	wear due to
adhesion	transfer of material from one surface to another by shearing of solid, welded junctions of asperities
abrasion	hard particles or protuberances along a soft, solid surface
delamination	delamination of thin material sheets beneath the interface in the substrate
erosion	mechanical interaction between a solid surface and a fluid, or impinging liquid or solid particles
fretting	small amplitude oscillatory tangential movement between two surfaces
fatigue	fracture arising from surface fatigue
corrosive/oxidative	sliding in a corrosive/oxidative environment

The wear and friction behavior of bodies exposed to relative movements is not a material property but the response of a so-called tribosystem [4]. A tribosystem includes at minimum two contacting bodies and all environmental factors affecting their interaction [20]. Nevertheless, the surface properties of each body directly affect the wear and friction behavior [19]. Relevant surface properties are surface energy, chemical composition, microstructure, hardness, surface roughness, and other mechanical properties such as fracture

toughness or yield strength [19]. Subsurface properties are also relevant since the relative movement on metals leads to plastic deformation at the surface, causing an immense strain gradient in the subsurface region [4]. Surface engineering aims to enhance the surface and subsurface properties of engineering components, amongst others, concerning their friction and wear behavior [19]. This includes inducing changes in the subsurface region, developing another material layer at the surface, changing the structure of the surface using thermal or mechanical treatments, or adjusting the chemical composition at the surface and in the subsurface region [19].

2.2 Titanium and titanium alloys

2.2.1 Characteristics of titanium alloys

Titanium is a transition element with an atomic number of 22 [21]. It was first discovered in oxidized form in 1791 by William Gregor [5, 21]. The titanium oxides ilmenite ($FeTiO_3$) and rutile (TiO_2) are the dominating mineral resources from which titanium metal is derived by employing the so-called Kroll process [5, 21]. At room temperature, titanium has a hexagonal close-packed (hcp) crystal structure (α-phase) [5] and a density of 4.5 g/cm³ [22]. Above 882 °C, a body-centered cubic (bcc) crystal structure (β-phase) occurs [5]. The addition of alloying elements can either increase or decrease this α/β transformation temperature [5]. The influence of alloying elements on the stability of the α- or β-phase is shown in Figure 1. Typical α-stabilizers are Al, O, or N, while V, Nb, and Ta stabilize the β-phase [5].

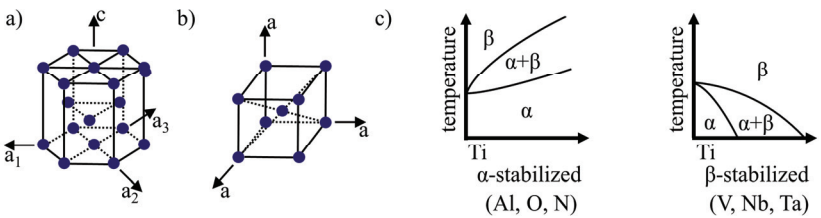

Figure 1: a) hexagonal close-packed titanium α-phase, b) body-centered cubic titanium β-phase, and c) schematic phase diagrams of α- and β-stabilized titanium according to Lütjering and Williams [5].

Dependent on their prevailing composition and microstructure, titanium alloys are classified as commercially pure α-titanium, α-alloys, α+β-alloys, and β-alloys. Commercially pure titanium and α-alloys show an exceptionally high corrosion resistance and deformability, α+β-alloys exhibit a combination of high strength and ductility, and β-alloys have the highest strength in combination with a low Young's modulus, high toughness, and high fatigue strength. Compared to other metals, such as steel or aluminum, titanium alloys possess a low density, a high specific strength, outstanding corrosion resistance, and good biocompatibility. [5]

The excellent biocompatibility is due to the spontaneous formation of a passivating TiO_2-rutile oxide layer in air or blood, enhancing tissue growth [23]. Other beneficial factors are the corrosion resistance against aggressive body fluids or the absence of allergic reactions [23]. On

the downside, titanium alloys exhibit poor tribological behavior, i.e., they have a low surface hardness, often show a high or unstable friction coefficient, and are prone to severe adhesive wear [6, 7].

2.2.2 Characteristics of Ti6Al4V

Ti6Al4V belongs to the class of α+β-alloys and is the most widely used titanium alloy covering applications ranging from structural aircraft parts to joint implants [5]. With 995 °C, the α/β transformation temperature of Ti6Al4V is higher compared to pure titanium at 882 °C [5]. The mechanical properties of Ti6Al4V depend on the thermal history during processing and may exhibit anisotropy [24]. A wrought and annealed Ti6Al4V alloy, with a density of 4.4 g/cm³, has a Young's modulus of 114 GPa, a yield strength of 924 MPa, an ultimate tensile strength of 993 MPa, and an elongation at break of 14 % [22]. The Vickers hardness ranges between 290 HV and 390 HV [8, 25–28].

Ti6Al4V was amongst the first titanium alloys used for implants in the human body [5, 23]. Compared to commercially pure titanium, the spontaneously forming oxide layer is thicker and contains aluminum [29]. While a general superiority of Ti6Al4V over pure titanium for implant applications is not given [30], Ti6Al4V is preferred for applications that require a high fatigue strength, e.g., in artificial hip joints or knee implants [5, 23]. However, the formation of wear debris observed in such tribosystems is critical and has to be avoided, e.g., through a surface treatment [8].

2.3 High entropy alloys

2.3.1 Characteristics of high entropy alloys

According to Yeh et al. [31], high entropy alloys (HEA) are alloys consisting of at minimum five principal elements in equimolar ratio, or at least with the concentration per element being between 5 at.% and 35 at.%. After the first publications on this new material class in 2004 [31, 32], alloys comprising this definition have attracted great research interest in the last decades [33], with more and more new HEA being developed [34]. Four so-called core effects were, to a large extent, made responsible for the characteristic microstructures and material properties of HEA: a "high-entropy effect", a "severe lattice distortion effect", a "sluggish diffusion effect", and a "cocktail effect" [35, 36]. Despite these core effects being subject to controversial discussions [37] or even being proven wrong [38–41], the concept of HEA opened a huge alloy compositional space, including alloys with potentially interesting properties [42]. Many of the so far explored HEA result from a thrive to obtain single-phase solid-solution multicomponent alloys based on the "high-entropy effect" [38]. The idea of this effect is that due to the presence of multiple principal elements in a HEA the entropy of mixing is increased, which favors the formation of a perfectly ordered solid-solution phase instead of intermetallic phases [36]. This is counterintuitive when looking at the phase diagram of conventional binary alloys, e.g., the one of TiAl in Figure 2, where intermetallic phases of stoichiometric composition and superlattice order occur at equimolar alloy composition [36]. The quinary CrMnFeCoNi face-centered cubic alloy, called Cantor alloy, and the TiZrNbHfTa bcc alloy,

called Senkov alloy, are two popular HEA reported to crystallize as single-phase solid solutions [32, 43]. However, the single-phase nature of these alloys is restricted to a limited temperature range [44, 45].

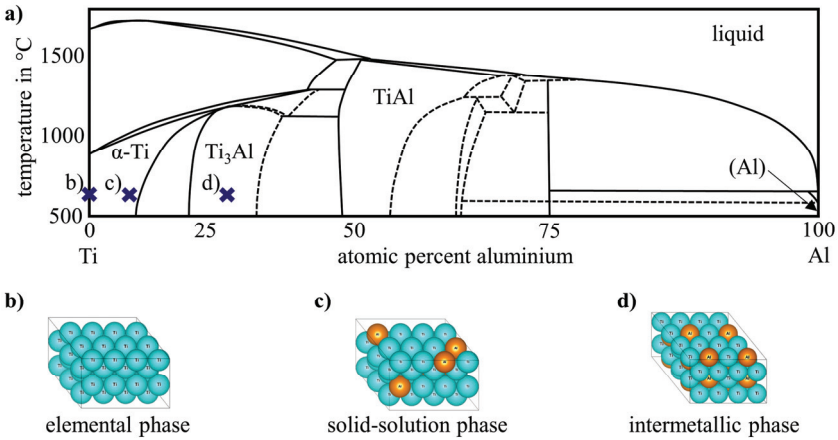

Figure 2: a) simplified TiAl-phase diagram according to Baker et al. [46] based on the work of Murray [47], indicating three competing states in a solid alloy: b) elemental phase, c) solid-solution phase, and d) intermetallic phase.

2.3.2 Characteristics of TiZrNbHfTa

The HEA TiZrNbHfTa, which contains titanium, zirconium, niobium, hafnium, and tantalum in equimolar composition, was first synthesized by Senkov et al. in 2011 via arc-melting [43]. When rapidly cooled down during manufacturing, the alloy is in a fully disordered solid-solution state with a single-phase bcc crystal structure, whereas dendritic structures with microsegregations occur at slower cooling rates [48]. In that case, the dendrite arms are rich in Nb and Ta, while the microsegregations are rich in Ti, Zr, and Hf [48, 49]. Single-phase bcc TiZrNbHfTa is one of only a few refractory high entropy alloys that exhibit ductile tensile behavior at room temperature [50] and hence the ability to be severely plastically deformed, e.g., via cold rolling [51]. The ultrafine-grained microstructure resulting from cold rolling is a desired initial state to control the grain size of TiZrNbHfTa. This is achieved by subsequent annealing, during which recrystallization occurs. The combination of cold rolling and subsequent annealing is commonly deployed to control the microstructure and, hence, tailor the mechanical properties of TiZrNbHfTa [51–58]. An exemplified recrystallized microstructure resulting from annealing cold-rolled TiZrNbHfTa is provided in Figure 3 a) and b).

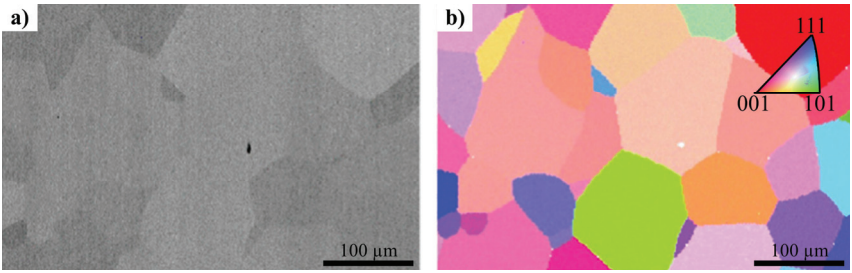

Figure 3: a) microstructure of recrystallized cold-rolled TiZrNbHfTa provided by Easo P. George, Oak Ridge National Laboratory, after 1 h of annealing at 1200 °C with subsequent quenching and b) corresponding color-coded inverse pole figure derived from electron back-scattered diffraction indicating the grain orientation. a) and b) are magnified excerpts adapted from Gadelmeier et al. [58] under CC BY 4.0 license.

Schuh et al. [45] used nanocrystalline TiZrNbHfTa to analyze the stability of the bcc phase at temperatures as low as 300 °C. Due to a high amount of grain boundaries in nanocrystalline TiZrNbHfTa, which act as diffusion pathways, phase transformations can be observed already after short annealing times [45]. The single-phase nature of TiZrNbHfTa turned out to be metastable below 1100 °C [45]. First principle calculations predict the decomposition of the initial bcc phase into another Nb- and Ta-rich bcc phase and a Hf- and Zr-rich hcp phase at 1020 °C [59]. This is in accordance with experiments [45, 60, 61] and the phase diagram calculated via Thermo-Calc and the TC-Ni8 database, as shown in Figure 4. While the depicted bcc1, bcc2, and hcp1 phases are experimentally observed, the predicted hcp2 phase is unlikely to form due to an inhibited phase transformation capability at such low temperatures.

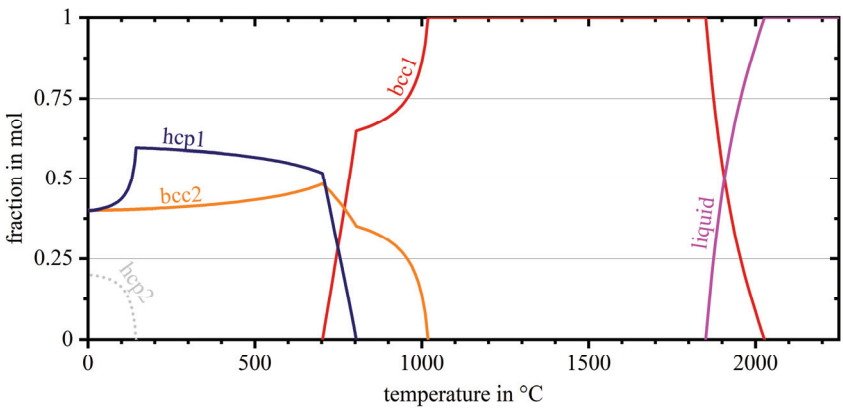

Figure 4: TiZrNbHfTa phase diagram obtained via Thermo-Calc based on the TC-Ni8 database.

In this work, bcc1 refers to an equimolar TiZrNbHfTa bcc phase obtained above 1020 °C. The Nb- and Ta-rich bcc phase that may occur during phase decomposition below 1020 °C is labeled

bcc2 phase. Hcp1 refers to the Hf- and Zr-rich hcp phase resulting from a phase decomposition below 1020 °C. In contrast to the bcc1 phase, the terms bcc2 and hcp1 are not restricted to the description of a precise elemental composition. Any bcc or hcp phases that may occur in addition are consecutively numbered or given a specific name, e.g., bcc(O) or hcp(O) in case of an oxygen-rich phase.

TiZrNbHfTa is currently not used in commercial applications. Nevertheless, it is discussed as a biocompatible material due to its ductility, low Young's modulus, high compressive yield strength, and good fatigue behavior [11, 12]. All elements in TiZrNbHfTa are supposed to be biocompatible [62]. Cold-rolled TiZrNbHfTa has a yield strength of 1202 MPa, an elongation at break of 4.7 %, a Young's modulus of 93.3 GPa, and a hardness of approx. 366 HV [51]. Table 2 sets these mechanical properties in comparison to Ti6Al4V. To the author's knowledge, the tribological behavior of pure TiZrNbHfTa has not yet been investigated. However, TiZrNbHfTa nitride and carbide coatings and amorphous TiZrNbHfTa sputtered on Ti6Al4V lead to improved surface mechanical and wear properties [12, 63, 64].

Table 2: Mechanical properties of TiZrNbHfTa in comparison to Ti6Al4V.

property	TiZrNbHfTa	Ti6Al4V
yield strength	1202 MPa [51]	924 MPa [22]
Young's modulus	93.3 GPa [51]	114 GPa [22]
elongation at break	4.7 % [51]	14 % [22]
hardness	366 HV [51]	290 HV - 390 HV [8, 25–28]

2.4 Oxidation

2.4.1 Oxidation of metals and alloys

In terms of a metal reacting with gaseous oxygen, the oxidation reaction is expressed as [65]:

$$iM + \frac{j}{2}O_2 = M_iO_j \tag{2}$$

i,j: *stoichiometric numbers*
M: *metallic element*
O_2: *molecular oxygen*
M_iO_j: *metal oxide*

The formation of a metal oxide is thermodynamically favored if the oxygen partial pressure, i.e., the contribution of oxygen to the overall pressure based on its amount fraction [66], is larger than the dissociation pressure of the oxide [65]. This dissociation pressure depends on the standard Gibbs free energy of formation of the oxide and the temperature [65]. In addition, the activity of the metal and the metal oxide have to be considered if not present as pure components at standard state, yielding [65, 67]:

$$p_{diss} = \left(\frac{a_{M_iO_j}}{a_M{}^i}\right)^{\frac{j}{2}} e^{\frac{2\Delta G^0(M_iO_j)}{jRT}} \quad (3)$$

p_{diss}: *oxide dissociation pressure*
i,j: *stoichiometric numbers*
a_{MiOj}: *activity of the metal oxide*
a_M: *activity of the metal*
ΔG^0: *standard Gibbs free energy*
M: *metallic element*
M_iO_j: *metal oxide*
R: *universal gas constant*
T: *temperature*

A common way to represent the stability of a metal oxide related to oxygen partial pressure, temperature, and standard Gibbs free energy is the Ellingham-Richardson diagram. By looking at the lines corresponding to specific oxidation reactions, it is assessable if and which oxides form at a given temperature and oxygen partial pressure [68]. Figure 5 shows a schematic Ellingham-Richardson diagram of oxidation reactions relevant to this work based on calculated Gibbs free energy data [69]. One can quickly identify that at 1000 °C, the dissociation pressure of HfO_2 is lower than that of Nb_2O_5, making Nb_2O_5 the less stable oxide.

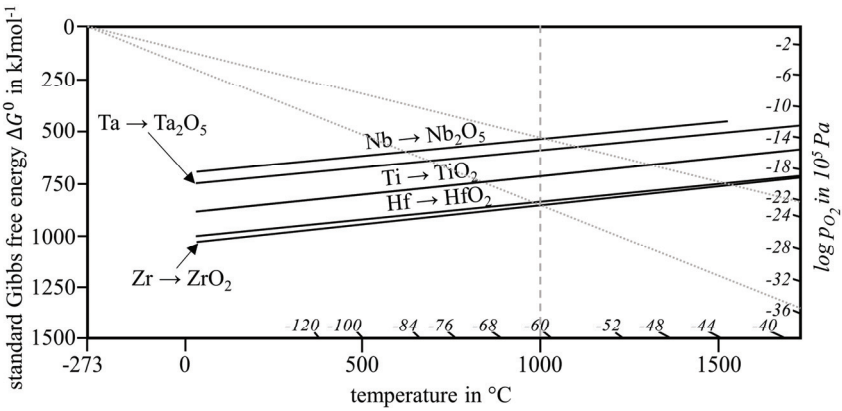

Figure 5: Approximated schematic Ellingham-Richardson diagram of selected oxidation reactions derived from calculated Gibbs free energy data [69].

Figure 6 a) visualizes the process steps during the oxidation of metals. Firstly, oxygen from the surrounding atmosphere is adsorbed at the metal surface. Next, oxides nucleate, followed by lateral growth of the oxides. This process is accompanied by oxygen diffusion towards and dissolution of oxygen into the metal. Subsequently, a compact oxide layer forms and grows while oxygen continues to diffuse into the metal, where it interstitially dissolves or forms internal oxides. Depending on the ratio of oxide volume compared to the volume of metal from which the oxide is formed, known as the Pilling-Bedworth ratio, tensile growth stresses (ratio < 1) or compressive growth stresses (ratio > 1) arise in the oxide layer. [65]

The rate at which an oxide layer forms can be expressed as oxide layer thickness evolution or area-specific mass change over time. Common rate equations are logarithmic, linear, and parabolic, as shown in Figure 6 b). Since the oxidation reaction rate depends on multiple factors, e.g., temperature, surface preparation, or elapsed reaction time, other rate equations or combinations of the logarithmic, linear, or parabolic rate equation are also possible. [65]

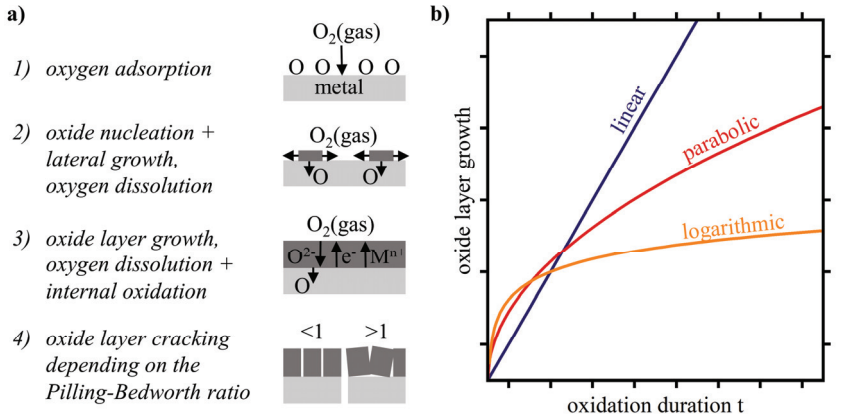

Figure 6: a) schematic representation of processes encountered during oxidation according to Kofstad [65], and b) illustration of common rate equations describing the time-dependent evolution of oxide layer thickness or area-specific mass change due to oxidation.

High-temperature oxidation of metals is often a diffusion-controlled process due to inward oxygen diffusion through the oxide layer. Therefore, it is best described by the parabolic rate equation [65]:

$$s^2 = k_s \cdot t \qquad \left(\frac{\Delta m}{A}\right)^2 = k_m \cdot t \tag{4}$$

s: *thickness of oxide layer*
k_s, k_m: *rate constants*
t: *oxidation duration*
$\Delta m/A$: *mass change per specimen surface*

The rate constants show a temperature dependency following the Arrhenius equation [65]:

$$k_s = k_{s0} \cdot e^{\frac{-Q_s}{RT}} \qquad k_m = k_{m0} \cdot e^{\frac{-Q_m}{RT}} \tag{5}$$

k_s, k_m: *rate constants*
k_{s0}, k_{m0}: *pre-exponential factors*
Q_s, Q_m: *activation energies of layer growth and mass change*
R: *universal gas constant*
T: *temperature*

Assuming volume consistency of the specimen in the case of inward-growing oxide layers, the rate constants k_m and k_s can be converted into each other. Combining the oxide layer thickness- and mass change-related rate equations (4) yields equation (6). According to equation (6), experimental time- and temperature-dependent mass change and oxide layer thickness values can be used to derive a density change $\Delta\rho(T)$ in the volume affected by oxygen ingress. For a given temperature, this density change acts as a conversion factor between the rate constants k_m and k_s.

$$\frac{\frac{\Delta m(t,T)}{A}}{s(t,T)} = \frac{\sqrt{k_m(T)\cdot t}}{\sqrt{k_s(T)\cdot t}} \Rightarrow \Delta\rho(T) = \sqrt{\frac{k_m(T)}{k_s(T)}} \tag{6}$$

$\Delta m(t,T)/A$: *time and temperature-dependent mass change per specimen surface*
$s(t,T)$: *time and temperature-dependent thickness of oxide layer*
$k_s(T)$, $k_m(T)$: *temperature dependent rate constants*
t: *oxidation duration*
$\Delta\rho(T)$: *temperature-dependent density change*

As indicated in Figure 6 a), oxygen dissolution into the metal accompanies the oxide layer formation during high-temperature oxidation. Driven by an oxygen concentration difference between the specimen surface and the substrate, oxygen diffuses towards the substrate following Fick's first law of diffusion [70]:

$$J = -D\frac{dc}{dx} \tag{7}$$

J: *diffusion flux*
D: *diffusion coefficient*
c: *concentration*
x: *location on a length scale*

At higher temperatures, the oxygen diffusion is accelerated due to the temperature dependency of the diffusion coefficient D, which is given as [65]:

$$D = D_0 \cdot e^{\frac{-Q_d}{RT}} \tag{8}$$

D: *diffusion coefficient*
D_0: *pre-exponential factor*
Q_d: *activation energy of diffusion*
R: *universal gas constant*
T: *temperature*

Based on Fick's second law of diffusion, stating that the change of concentration in a defined volume is the difference between inward and outward diffusion flux, the oxygen concentration in a semi-infinite solid with constant surface oxygen concentration can be described according to equation (9) [70]. Assuming that oxide layer growth is negligible, this equation represents the oxygen concentration-depth profile of an oxygen diffusion zone forming during oxidation.

$$c(x,t) = -(c_{x=0} - c_{x=\infty}) \cdot \mathrm{erf}\left(\frac{x}{2\sqrt{Dt}}\right) + c_{x=0} \tag{9}$$

c(x,t): *time-dependent, local concentration*
$c_{x=0}$: *constant concentration at the gas-metal interface*
$c_{x=\infty}$: *constant concentration in the metal substrate*
x: *location on a depth length scale from the gas-metal interface*
D: *diffusion coefficient*
t: *time*

Figure 7 visualizes Fick's first and second law of diffusion and schematically shows the evolution of an oxygen concentration-depth profile in a semi-infinite solid metal over time.

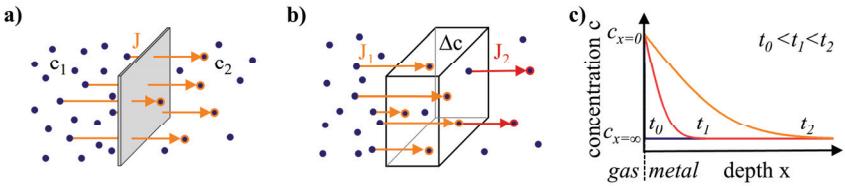

Figure 7: a) visualization of the diffusion flux representing the number of atoms penetrating a unit area per unit time due to a concentration difference, b) the concentration change per time unit in a volume due to the difference of inbound and outbound flux, and c) time-dependent oxygen concentration-depth profiles in a semi-infinite solid metal according to equation (9).

In the case of an alloy containing different metallic elements, inward oxygen diffusion can also cause the selective oxidation of alloy components within the metal. This phenomenon is termed internal oxidation. Internal oxidation occurs if, due to the inward oxygen diffusion, the oxygen partial pressure in the metal gets higher than the oxide dissociation pressure of one or several oxides corresponding to one or several elements of the alloy, as defined in equation 3 on page 8 [65].

2.4.2 Oxidation-induced surface hardening

Oxidation of metals in an oxidizing, gaseous atmosphere at elevated temperatures, sometimes also called thermal oxidation, is often undesired since it has detrimental effects on the metal. It can lead to a loss of material or a reduction of its load-bearing capability [65]. However, oxidation can be a valuable method for surface hardening. This is because metal oxides are typically harder than the metal on which they are formed [22, 71]. In addition, oxygen inward diffusion leads to a hardness increase in the subsurface region because the oxygen concentration in a metal is often assumed to correlate with the hardness in a linear way [28, 72, 73]. In this case, the hardness-depth profile in an oxygen diffusion zone can be expressed by equation (10), similar to equation (9). According to a recent study by Vaché et al. [74], a parabolic relationship more accurately represents the correlation between oxygen concentration and hardness in titanium alloys, leading to equation (11).

$$h(x,t) = -(h_{x=0} - h_{x=\infty}) \cdot \mathrm{erf}\left(\frac{x}{2\sqrt{Dt}}\right) + h_{x=0} \tag{10}$$

$$h(x,t) = -(h_{x=0} - h_{x=\infty}) \cdot \sqrt{1 - \mathrm{erf}\left(\frac{x}{2\sqrt{Dt}}\right)} + h_{x=0} \tag{11}$$

h(x,t): *time-dependent, local hardness*
$h_{x=0}$: *hardness at the gas-metal interface*
$h_{x=\infty}$: *hardness in the metal substrate*
x: *location on a depth length scale starting from the gas-metal interface*
D: *diffusion coefficient*
t: *time*

The formation of an oxygen diffusion zone is especially pronounced for elements exhibiting a high oxygen solubility, such as titanium, zirconium, and hafnium. Their temperature-dependent maximum oxygen solubility limit is 33 at.% [13], 35 at.% [15], and 22 at.% [17], as detailed in Table 3.

Table 3: Temperature-dependent maximum oxygen solubility limits according to Ti-O, Zr-O, Nb-O, Hf-O, and Ta-O phase diagrams available in the literature.

element	**O solubility limit (hcp)** concentration in at.%	**O solubility limit (bcc)** concentration in at.%
Ti	33 (0 °C - 1771 °C) [13]	8 (1743 °C) [13]
Zr	31 (2071 °C) [14]	10 (1968 °C) [14]
	35 (2065 °C) [15]	11 (1970 °C) [15]
Nb	-	9 (1915 °C) [75]
Hf	21 (2180 °C) [16]	3 (2250 °C) [17]
	22 (2200 °C) [17]	5 (2000 °C) [16]
Ta	-	6 (1880 °C) [76, 77]

Figure 8 shows different oxidation processes that can be applied to elements and alloys possessing a high oxygen solubility [9, 78, 79]. The most straightforward concept is a single-step process consisting of oxidation in air. An oxide layer forms while an oxygen-diffusion zone is barely present. In a two-step process, a vacuum heat treatment step is added. The oxide layer is reduced if the oxygen partial pressure at the oxide-metal interface gets lower than the oxide dissociation partial pressure during the vacuum heat treatment step. A pronounced oxygen diffusion zone with a gradual hardness decrease forms upon oxygen inward diffusion of the released oxygen. This process is also called oxygen boost diffusion [80]. A three-step process with an additional oxidation in air leads to the formation of an oxide layer on top of the pronounced oxygen diffusion zone created with the two-step process. A similar result is expected if the oxidation is performed in an atmosphere with reduced oxygen partial pressure.

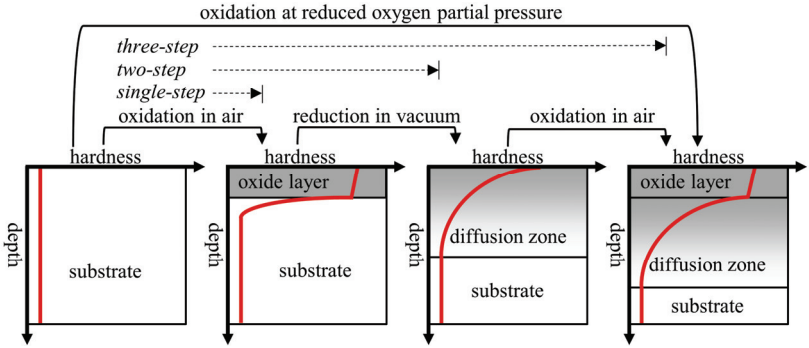

Figure 8: Visualization of a single-step, two-step, and three-step oxidation process and oxidation at reduced oxygen partial pressure with their resulting hardness-depth profiles.

2.4.3 Oxidation of Ti6Al4V

Single-step oxidation of Ti6Al4V in air is well explored and often performed in the temperature range between 600 °C to 850 °C with oxidation durations mainly of a few hours and rarely hundreds of hours [8, 26, 81–97]. The oxide layer thickness increases at higher temperatures and oxidation durations [81, 82, 86, 93]. This goes along with an increase in porosity [86, 92] and surface roughness [84, 92, 94], while the oxide layer adhesion on the substrate decreases and spallation occurs [8, 86, 92]. The formed oxide layer mainly consists of TiO_2 in the form of anatase or rutile, dependent on the process parameters [26, 84, 92, 95]. Al_2O_3 layers may occur upon prolonged oxidation durations [82]. Oxygen diffusion zones forming underneath the oxide layer during single-step oxidation typically are much lower than 100 µm [8, 81, 83-85]. Nevertheless, a positive impact on surface hardness and wear resistance has been reported [8, 26, 84–88, 91, 96, 97]. The reaction kinetics during the single-step process follows a linear to parabolic rate law, dependent on the oxidation temperature and duration [82]. Under the assumption of parabolic behavior, the kinetics of mass change due to oxide formation and oxygen dissolution can be modeled using equation (4) on page 9 with k_{m0}=4.9·10^5 kg²m^{-4}s^{-1}and Q_m=232 kJmol^{-1} [98]. Based on multiple studies and following equation (8) on page 10, oxygen diffusion in Ti6Al4V during oxidation is characterized by D_0=3.83·10^{-5} m^{2}s^{-1} and Q_d=200 kJmol^{-1} [98].

Two-step oxidation of Ti6Al4V was first introduced by Dong et al. in 2000 [80]. The vacuum heat treatment step following single-step oxidation proved to work best at 850 °C with typical durations ranging from 30 min to 60 h [25, 28, 80, 99, 100]. Due to the oxygen released during the reduction of the oxide layer, oxygen diffusion zone depths of more than 100 µm are achieved with the two-step process [80, 99–101]. This results in an increased surface hardness and better wear resistance compared to untreated Ti6Al4V [99, 100].

Three-step oxidation of Ti6Al4V has only been investigated by Bacroix et al. [99]. According to their work, combining air oxidation above 800 °C for 30 min, vacuum treatment at 850 °C

for 20 h, and air oxidation at 620 °C for 30 min leads to an oxygen diffusion zone of approx. 600 µm and an improved wear resistance [99].

The oxidation of Ti6Al4V at reduced oxygen partial pressure has been investigated by Du et al. [102]. At an oxygen partial pressure of 10^{-18} Pa created in an H_2/H_2O atmosphere, a multi-layered TiO_2 oxide layer with an intermediate Al_2O_3 layer forms at a parabolic growth rate [102]. Studies on the surface hardness and wear behavior of Ti6Al4V oxidized at reduced oxygen partial pressure are not published to the author's knowledge. The formation of an oxygen diffusion zone during oxidation at reduced oxygen partial pressure is neither described in the literature.

2.4.4 Oxidation of TiZrNbHfTa

Studies on the oxidation behavior of TiZrNbHfTa or similar alloys are rare. Single-step oxidation of as-cast TiZrNbHfTa with a dendritic microstructure leads to pesting or catastrophic oxidation and disintegration of the metal into oxide powder in the temperature range of 700 °C to 1300 °C [18]. This is attributed to the formation of low-density mixed oxides failing to form a protective oxide layer [18]. Oxide powder derived from the oxidation of cold-rolled TiZrNbHfTa at 800 °C only contained the monometallic oxides TiO_2, ZrO_2, Nb_2O_5, HfO_2, and Ta_2O_5 [11]. These oxides are also identified on TiZrNbHfTa and $Ti_{1.5}ZrNb_{0.5}Hf_{0.5}Ta_{0.5}$ oxidized in air at ambient temperature [64, 103–105].

Figure 9 a) shows a micrograph of as-cast TiZrNbHfTa after 1 h of oxidation at 700 °C. Underneath an oxide layer rich in cracks, Chang et al. [18] assume an oxygen diffusion zone. In contrast, Sheik et al. [106] report internal oxidation underneath an oxide layer formed on $Ti_{1.5}ZrNb_{0.5}Hf_{0.5}Ta_{0.5}$. Nevertheless, they also observe catastrophic oxidation in the temperature range of 600 °C to 1000 °C [106], as visible in Figure 9 b). According to their work, fast oxygen ingress through interstitial diffusion along the grain and sub-grain boundaries could be responsible for the occurrence of catastrophic oxidation [106]. Due to the catastrophic oxidation behavior of TiZrNbHfTa, no oxide layer growth kinetics data or oxygen diffusion coefficient information is available in the literature to the author's knowledge.

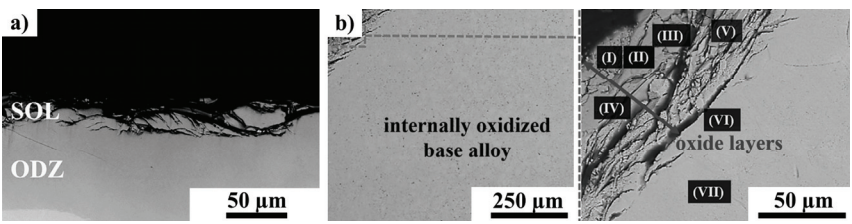

Figure 9: a) micrographs of a cracked surface oxide layer (indicated via SOL) on an assumed oxygen diffusion zone (indicated via ODZ) after oxidation of TiZrNbHfTa at 700 °C for 1 h [18] and b) a cracked oxide layer on top of a region of internal oxidation after oxidation of $Ti_{1.5}ZrNb_{0.5}Hf_{0.5}Ta_{0.5}$ at 800 °C for 5 h [106]. a) and b) are reprints of Chang et al. [18] and Sheik et al. [106] with permission from John Wiley and Sons, WILEY-VCH Verlag © 2018, and Elsevier, Elsevier © 2018.

The description of the observed subsurface phenomena, i.e., the formation of an “oxygen diffusion zone” [18] versus the occurrence of “internal oxidation” [106], is an unambiguous terminology. As Figure 6 (page 9) points out, oxygen diffuses towards the substrate in both cases. In the substrate, oxygen can be present in dissolved state, meaning in the form of interstitial atoms in the metal lattice, and/or lead to the formation of internal oxides.

To distinguish between these two scenarios, the following terminology is used in this work:

- oxygen diffusion zone: subsurface region in which diffused oxygen is entirely dissolved, meaning incorporated in the metal lattice as interstitial atoms
- oxygen-enriched zone: subsurface region in which diffused oxygen is present in the form of internal oxides, a combination of internal oxides and interstitial oxygen, or if the presence of solely interstitial oxygen is not experimentally confirmed

Furthermore, the terms subsurface region and substrate in this work are defined as follows:

- subsurface region: region underneath a surface oxide layer, or the air-specimen interface if no surface oxide layer is present, until the substrate
- substrate: part of the specimen that exhibits constant material properties, e.g., an identical microstructure, over a considerable length scale and is not affected by oxygen ingress

3 Research questions

The state of research on oxidation of the commercially available Ti6Al4V and TiZrNbHfTa, which has only been known for a few years, is significantly different regarding the level of understanding of these two material systems. While oxidation-induced surface hardening using the single-step and the two-step process is well described for Ti6Al4V, less is known about the impact of the three-step process and oxidation at reduced oxygen partial pressure. For TiZrNbHfTa, oxidation-induced surface hardening has not been studied because, so far, only catastrophic oxidation has been observed. Therefore, the focus of the research questions differs between the two material systems. For Ti6Al4V, it is on comparing the oxidation process-dependent surface properties, while a fundamental understanding of the oxidation processes of TiZrNbHfTa needs to be established in the first place.

Ti6Al4V:

- In what way do the different oxidation processes affect the characteristic surface properties?
- Compared to the single-step process, can three-step oxidation and oxidation at reduced oxygen partial pressure improve oxide layer adhesion?
- Which oxidation process leads to the best wear behavior?

TiZrNbHfTa:

- Under which experimental conditions can single-step oxidation lead to the formation of an adherent oxide layer and what is the influence of microstructure on the oxidation behavior?
- What is the reaction kinetics of oxide layer growth and mass change during single-step oxidation?
- Is two-step oxidation of TiZrNbHfTa possible, and can a pronounced gradual hardness decrease due to an oxygen diffusion zone be achieved similar to Ti6Al4V?
- How do single-step and two-step oxidation affect the characteristic surface properties, and can they be further improved by a three-step process or oxidation at reduced oxygen partial pressure?
- Can oxidation of TiZrNbHfTa lead to superior tribological properties compared to Ti6Al4V?

4 Materials and experimental methods

4.1 Material preparation

Ti6Al4V specimens are prepared from 2 mm thick commercial sheet material, fulfilling the AMS 4911 standard. A guillotine shear is used to cut centimeter-sized specimens from the sheet material. Heat treatments in order to alter the as-received material properties before experiments are not performed.

TiZrNbHfTa is not commercially available and hence manufactured on a laboratory scale. Three different manufacturing routes are deployed to investigate the influence of microstructure on the oxidation behavior of TiZrNbHfTa. All initial TiZrNbHfTa specimens are single-phase bcc, as confirmed by experimental analysis (section 5.2.1).

As-cast TiZrNbHfTa is manufactured by Christian Gadelmeier, Metals & Alloys, University of Bayreuth. In a Bühler vacuum arc-melting system, the pure constituent elements are melted to an ingot on a cooled copper plate. To ensure homogeneity, the ingot is flipped and remelted five times. The ingot is then wire-cut into approx. 1 mm thick slices using an AgieCharmilles Cut 200 SP. The final specimens are prepared either by wire cutting or using a precision cut-off machine.

Rolled TiZrNbHfTa is kindly provided by Easo P. George, Material Science and Technology Division, Oak Ridge National Laboratory. As described elsewhere [58], an arc-melted ingot is first drop-casted, then homogenized for 48 h at 1200 °C under vacuum, and finally cold-rolled at room temperature. A sheet of approx. 1 mm thickness is obtained, yielding a thickness reduction of approx. 90 % compared to the initial ingot. Specimens from the rolled sheet are either prepared by wire cutting or using a cut-off machine.

Rolled & annealed TiZrNbHfTa is obtained by heat-treating specimens from the rolled TiZrNbHfTa sheet. The specimens are encapsulated in an evacuated quartz glass tube and inserted into a preheated furnace at 1200 °C for 1 h. Subsequently, the glass tubes are quenched in cold water.

Figure 10 shows the available amount of material obtained from each manufacturing route. Before further use, all specimens are ground down to P1200 SiC grinding paper and cleaned in an ethanol ultrasonic bath to ensure a consistent surface quality.

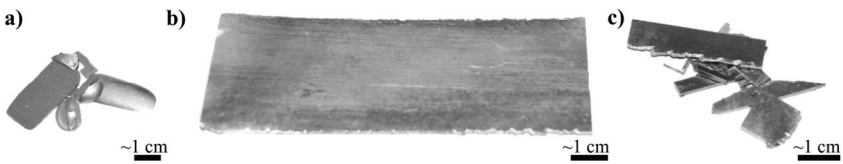

Figure 10: Images of a) slices of a former as-cast TiZrNbHfTa knob, b) rolled TiZrNbHfTa sheet material, and c) pieces to become rolled & annealed TiZrNbHfTa.

4.2 Oxidation processes

4.2.1 Oven setups

Single-step oxidation requires simple high-temperature oxidation in laboratory air. By default, this process is executed in a Rhode ME 8/13 heat treatment furnace. The oven is preheated for a minimum of 8 h to obtain a stable and homogeneous temperature distribution in the oven chamber. Specimens are inserted in the preheated oven and removed from the oven for air-cool down after their respective oxidation duration. As shown in Figure 11, specimens exceeding a length and width of 1 cm are placed upright in a specimen holder to enable air contact at all flat sides, while smaller specimens are inserted in an open quartz glass tube. Oxidation of selected TiZrNbHfTa specimens is combined with thermogravimetric analysis. In this case, the oxidation is performed in synthetic air (air flow: 50ml/min) after heating the specimen to the desired temperature at a heating rate of 20 K/min. One experiment series to compare the oxidation behavior of as-cast, rolled, and rolled & annealed TiZrNbHfTa is executed with a NETSCH STA 449F3 using inert gas during the heat-up phase. A second experiment series is performed in order to determine the kinetics of mass change during single-step oxidation with a NETZSCH STA 449F5 using artificial air during the heat-up period.

Following high-temperature oxidation in air, a reduction step is required to realize the two-step process. For this purpose, the oxidized specimens (at maximum 40 mm x 10 mm x 2 mm) are encapsulated in evacuated quartz-glass tubes of a volume of approx. $2.4 \cdot 10^{-5}$ m³, as shown in Figure 11 c). At an achieved pressure of 30 Pa in the glass tube, measured via a pressure gauge during the evacuation process, the amount of oxygen in the encapsulated volume is $\sim 1 \cdot 10^{-9}$ kg, which limits further oxidation and allows the reduction of the oxide layer. For heat treatment, the encapsulated Ti6Al4V specimens are inserted in the preheated Rhode heat treatment furnace and removed from the oven for an air-cool down after the desired duration. Glass tubes with TiZrNbHfTa specimens are inserted in a preheated Nabertherm LHT 04/18 heat treatment furnace, allowing higher temperatures. In this case, the glass tubes are thrown into cold water directly after the removal from the oven chamber to quench the specimens.

The additional final oxidation step in the three-step process is carried out in the same oven setup as the single-step process.

Figure 11: a) pictures of a specimen holder for oxidation in air of larger specimens, b) an open quartz-glass tube for oxidation in air of smaller specimens, and c) an encapsulated specimen in a sealed quartz-glass tube for oxide reduction under vacuum.

Figure 12 shows the oven setup for oxidation at reduced oxygen partial pressure, as described by Wenderoth et al. [107]. Ar-2%H_2 gas is guided into a water-containing impinger at a gas

flow of 2 l/min. The water in the impinger is held at constant temperature with the help of a tempered bath. Fine gas bubbles in the water, created by a frit in the impinger, cause an enrichment of the Ar-2%H_2 gas flow with a defined amount of H_2O before entering the glass tube in the tube furnace chamber. There, H_2O may dissociate following the equilibrium reaction:

$$H_2 + \frac{1}{2}O_2 \leftrightharpoons H_2O \tag{12}$$

The temperature-dependent oxygen partial pressure in the glass tube can therefore be calculated with the following equation [107]:

$$p_{O_2} = \left(\frac{p_{H_2O}}{n_{H_2} \cdot (p_{atm} - p_{H_2O})} \cdot k_0 \cdot e^{\frac{-\Delta G^0}{RT}}\right)^2 \tag{13}$$

p_{O2}: *oxygen partial pressure*
p_{H2O}: *water partial pressure*
n_{H2}: *hydrogen fraction in initial gas flow*
p_{atm}: *atmospheric pressure*
k_0: *constant*
ΔG^0: *standard Gibbs free energy*
R: *universal gas constant*
T: *temperature*

Specimens for oxidation at reduced oxygen partial pressure are placed in the glass tube and set under gas flow for 20 min at room temperature before the tube is inserted into the preheated tube furnace chamber for the desired oxidation duration. Cool down is again performed outside the furnace chamber at room temperature under continued gas flow.

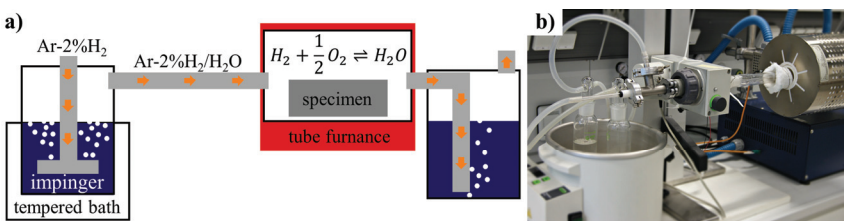

Figure 12: a) schematic gas flow in the oven setup for oxidation at reduced oxygen partial pressure and b) actual implementation.

Table 4 lists the oxygen partial pressures for the oxidation temperatures studied in this work approximated according to equation (13).

Table 4: Oxygen partial pressures obtained for different oven chamber temperatures.

temperature in °C	**600**	**650**	**750**	**850**
oxygen partial pressure in Pa	10^{-19}	10^{-18}	10^{-15}	10^{-13}

4.2.2 Process parameters

Since the oxidation behavior of Ti6Al4V is well described in the literature, the focus of a set of screening experiments is to establish suitable process parameters for the four different oxidation processes. Goal is to obtain specimens for a comparative study of the oxidation process-dependent surface properties. Table 5 shows the experiments conducted to identify under which conditions an adherent oxide layer forms on Ti6Al4V during oxidation in air or at reduced oxygen partial pressure and which duration is required to dissolve such an oxide layer under vacuum conditions.

Table 5: Experiments and process parameters for screening experiments on Ti6Al4V.

process step	temperature in °C	duration in h	purpose
oxidation in air	680 - 780	0.5 - 64	determine the parameter regime leading to an adherent oxide layer, i.e., absence of spallation
reduction in vacuum	850	1 - 8	determine the time to dissolve a ~2.5 µm thick oxide layer
O partial pressure	650 - 850	2 - 8	determine the parameter regime leading to an adherent oxide layer, i.e., the absence of spallation

In contrast to Ti6Al4V, the oxidation behavior of TiZrNbHfTa is not yet intensively investigated. As a first step, the influence of microstructure on the oxidation behavior during single-step oxidation is analyzed by comparing as-cast, rolled, and rolled & annealed material. The rolled material is then further studied in a broader temperature range, as shown in Table 6. Additionally, the two-step process and oxidation at reduced oxygen partial pressure are also realized for rolled TiZrNbHfTa.

Table 6: Experiments and process parameters for the characterization of the oxidation behavior of TiZrNbHfTa.

process step	temperature in °C	duration in h	purpose
oxidation in air	600	0 - 24	characterize and compare the oxidation behavior of as-cast, rolled, and rolled & annealed material
oxidation in air	550 - 650	0 - 24	detailed characterization of the oxidation behavior of rolled material
reduction in vacuum	1200	1	demonstrate that the two-step process is feasible for TiZrNbHfTa; characterization of the obtained surface and subsurface region
O partial pressure	600	24, 48	check if thicker adherent oxide layers or oxygen diffusion zones can be obtained with this process

Table 7 shows the process parameters used to realize the comparative study covering the single-step, two-step, and three-step processes and oxidation at reduced oxygen partial pressure

applied to Ti6Al4V. Specimens treated according to these process parameters are used to compare the oxidation process-dependent characteristic surface properties of Ti6Al4V, like the elemental composition, the morphology of a potential oxide layer, or the formation of an oxygen diffusion zone. Additionally, the tribological properties are assessed and set in contrast to rolled TiZrNbHfTa treated with the single-step and two-step process, as specified in Table 7. The surface morphology obtained during Ti6Al4V oxidation at reduced oxygen partial pressure requires a grinding post-processing step to remove needle-shaped oxide grains detrimental to the tribological performance. This is particularly important regarding a potential use in artificial knee joints and is performed before all tribological tests except ball-on-disk tribometer testing.

Table 7: Process parameters used for a comparative study of the effect of different oxidation processes on the surface properties of Ti6Al4V and TiZrNbHfTa

	Ti6Al4V				**TiZrNbHfTa**		
process	three-step			O partial pressure (+grinding)			
	two-step						
	single-step				single-step	two-step (+quenching)	
duration in h	16	6	16	2	8	24	1
temperature in °C	680	850	680	850	600	550	1200
atmosphere	air	vacuum	air	$Ar/H_2/H_2O$	air	air	vacuum
pressure in Pa	$1 \cdot 10^5$	$4 \cdot 10^3$	$1 \cdot 10^5$	$p_{O2} \approx 1 \cdot 10^{-13}$	$1 \cdot 10^5$	$1 \cdot 10^5$	$4 \cdot 10^3$

4.3 Material characterization

4.3.1 Metallographic preparation

The specimens of interest are cut into pieces using a precision cut-off machine, uncovering the cross-section to be investigated. Subsequently, the pieces are embedded in a conductive thermoplastic matrix material using an ATM OPAL X-PRESS hot mounting press. The mounted specimens are then wet-ground down to a minimum of P500 SiC grinding paper on a manually operated Struers LAboPol-21 grinder. After cleaning the mounted specimens in ethanol using an ultrasonic bath, an ATM SAPHIR 560 automated polishing machine is deployed to execute a series of polishing steps. These steps comprise polishing with 9 µm, 6 µm, and 3 µm diamond suspension, and polishing with an ATM Eposil F SiO_2 oxide particle suspension mixed with H_2O_2 (≈3:1). After each polishing step, the mounted specimens are cleaned in an ultrasonic bath using ethanol or water, depending on if diamond suspension or oxide particle suspension was previously used.

4.3.2 Microscopy

The specimen analysis via microscopy includes imaging of the specimen surfaces and cross-sections. A Keyence VHX-7100 digital optical microscope is used to generate overview images

of the wear traces resulting from knee joint wear testing. A Zeiss 1540 EsB Cross Beam scanning electron microscope (SEM) is used to obtain high-resolution images. In a SEM, the specimen is irradiated with a focused electron beam which generates secondary electron (SE) and backscattered electron (BSE) signals that can be detected [108]. SE imaging is used to analyze the surface morphology since it is associated with a high topography contrast. BSE imaging is used to investigate the microstructure since it provides a material contrast that allows to identify different phases. Imaging is done with an electron high tension voltage of 2 kV to 8 kV. The working distance is chosen between 4.5 mm and 7.5 mm at an aperture size of 60 µm.

4.3.3 Chemical analysis and crystallographic characterization

A Thermo Noran System Six energy dispersive X-ray spectroscopy (EDS) detector integrated into the SEM device is used to obtain elemental mappings. The incident SEM electron beam generates X-ray photons in the irradiated specimen volume, which have an element-specific energy and hence can be used to localize and quantify the present elements [108]. The default electron high tension voltage for elemental mappings of Ti6Al4V is 8 kV. The one for TiZrNbHfTa is 15 kV. The working distance is approx. 7.5 mm.

Alternative to EDS, a Jeol JXA-8100 electron probe micro analyzer (EPMA) is used to obtain qualitative oxygen concentration mappings of oxidized TiZrNbHfTa specimens. The working principle is similar to EDS except that wavelength-dispersive X-ray spectrometers spectrally separate the X-rays before targeting a detector [109]. This is advantageous to unambiguously identify oxygen having element-specific X-ray photon energies close to the ones of titanium. The EPMA measurements shown in this work are kindly provided by Beyza Öztürk, DECHEMA-Forschungsinstitut.

An Orbis PC µX-ray fluorescence analysis (XRF) device is deployed to determine the elemental composition of as-cast, rolled, and rolled & annealed TiZrNbHfTa after manufacturing. This method uses an X-ray source instead of an electron beam to locally excite the specimen, generating X-ray photons of element-specific characteristic energy used for quantitative analysis [110]. For a bulk composition analysis of TiZrNbHfTa, this method is preferred over EDS and EPMA since it provides averaged information over a larger analysis volume.

The concentration of oxygen and nitrogen in as-cast, rolled, and rolled & annealed TiZrNbHfTa in the initial state is determined with a Horiba EMGA 620 W/C carrier hot gas extraction device. Three cubes per as-cast, rolled, and rolled & annealed material are prepared from bulk material using a wire-cut electrical discharge machine. Each cube has a mass of approx. 0.038 g and is ground and cleaned in ethanol before the measurements. Neue Materialien Fürth GmbH was commissioned to execute the measurements. The oxygen and nitrogen concentration in TiZrNbHfTa is then calculated from the average relative mass fraction of O and N in the respective cubes.

A Spectruma GDA-alpha glow discharge optical emission spectrometry (GDOES) device with a 2.5 mm anode and a CCD-optic is used to obtain elemental concentration-depth profiles, specifically the oxygen concentration-depth profile, of Ti6Al4V after various oxidation

processes. With the help of a glow discharge plasma, the sample surfaces are sputtered while the sputtered atoms get excited in the plasma emitting characteristic electromagnetic waves in the optical spectrum that can be detected [111]. This allows a depth-resolved quantitative elemental analysis [111]. The global calibration for the elemental analysis and the sputtering rates, correlating the sputtered time to the actual sputtered depth, were purchased from Spectruma Analytics GmbH. A readjustment of the depth scale in the Ti6Al4V substrate is necessary.

Figure 13 shows an unmodified oxygen concentration-depth profile received from a Ti6Al4V specimen with an oxide layer. Since the sputtering parameters are optimized towards depth profiling of 100 µm or more, the measured signal corresponding to the first ~0.5 µm should not be considered. The signal in this region is an artifact due to the plasma ignition. Furthermore, the lack of a discrete representation of the oxide-metal interface in the measured signal requires a manual definition of that transition point. Based on the work of Unnam et al. [112], 20 at.% is defined as the effective initial oxygen concentration at the oxide-metal interface marking the origin of the depth scale applicable to the substrate. The calibration of the substrate depth scale is further refined compared to the purchased global calibration using cross-section SEM images of sputtered specimens since the sputter rate is not constant over the whole specimen.

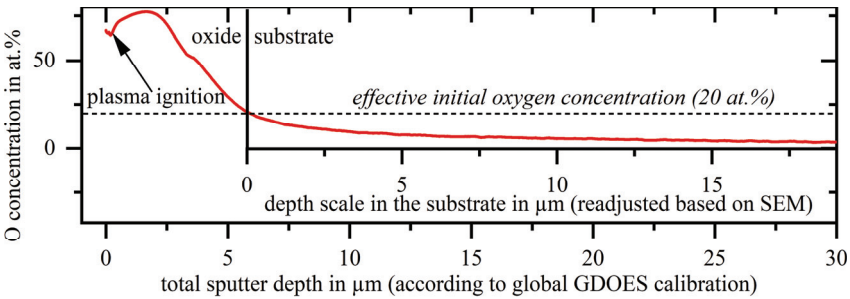

Figure 13: As-obtained oxygen concentration-depth profile demonstrating the need for a depth scale adjustment based on an effective initial oxygen concentration and cross-section SEM images of sputtered specimens.

For TiZrNbHfTa, implementing a GDOES measurement routine is not suitable due to the lack of appropriate calibration and referencing standards and the limited amount of TiZrNbHfTa specimens available to develop them. Instead, nuclear reaction analysis (NRA) is used to measure the oxygen concentration-depth profile of one rolled TiZrNbHfTa specimen after oxidation in air at 600 °C for 8 h.

NRA is a sophisticated method especially suitable for quantitative light element depth profiling with an intrinsic depth resolution of a few nanometers. The specimens are bombarded with a beam of projectile ions at high energies, typically ranging from 100 keV to 20 MeV. These impacting ions fuse with the nuclei to be investigated. During a resulting nuclear reaction, new nuclei form, and secondary particles such as protons or neutrons with defined energies are emitted and can be detected. [113]

An NRA spot measurement perpendicular to the surface of an oxidized, unmounted specimen is performed to obtain an oxygen concentration-depth profile until a depth of approx. 1.5 µm based on the intrinsic NRA depth resolution. For the task to obtain an oxygen concentration-depth profile of approx. 100 µm depth, an NRA mapping at a cross-section is realized. The mapping is performed on a cross-section with a map size of 200 µm x 150 µm and a pixel size of 2 µm x 2 µm. The pixel size is approx. half the beam size (4.5 µm x 3.5 µm) of the used 920 keV deuteron beam. These beam conditions are suitable to trigger the $O^{16}(d,p)O^{17}$ nuclear reaction, which has been proposed to study oxygen diffusion in solid metals [114]. All NRA experiments are kindly performed by Pascal Berger, Université Paris-Saclay, CEA, CNRS, NIMBE, including a detailed evaluation and the generation of the oxygen-concentration depth profiles.

In addition to EDS or NRA, atom probe tomography (APT) offers the possibility to get an elemental composition analysis of a target volume with atomic resolution, typically of a needle tip with a radius of less than 100 nm. A high electric field generated at the needle tip leads to a so-called field ionization of the metal atoms at the tip and subsequent evaporation of the ions. The ions are then accelerated in the field and can be identified with a detector. [115]

In this work, APT is used to characterize small precipitates occurring in TiZrNbHfTa after the two-step process. The measurements, including their evaluation, are kindly performed by Yujun Zhao in the group of Tong Li, Ruhr University Bochum. Needles are prepared from a region approx. 5 µm away from the surface, as shown in Figure 14 a). An FEI Helios G4 CX focused ion beam SEM is used for the needle preparation. For comparison, needles are prepared from the matrix and the precipitates (Figure 14 b)). The APT measurements on these needles are then performed with a Cameca LEAP 500 XR APT device and evaluated with an AP Suite 6 evaluation software. During the transfer from the SEM device to the APT device, surface contamination with oxygen may occur. This is accounted for by not considering the detected ions coming from the outmost regions of the needle tips. The elemental distribution figures obtained via APT of the needles represent only 5 % to 10 % of the number of obtained ions available for data analysis.

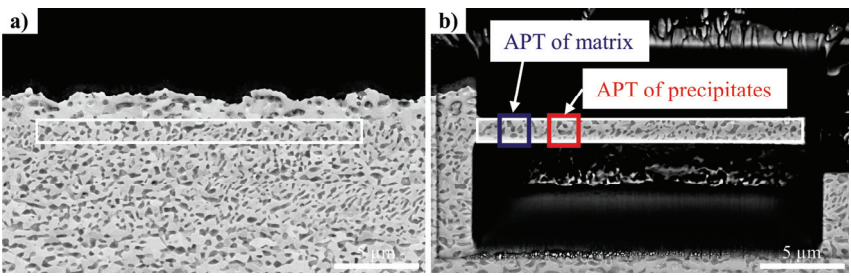

Figure 14: a) BSE-SEM images of a rolled TiZrNbHfTa specimen after the two-step process showing the region of needle extraction for APT and b) the detailed regions of origin of the needles representing the matrix and the precipitates. The images are taken and provided by Yujun Zhao in the group of Tong Li, Ruhr University Bochum.

X-ray photoelectron spectroscopy (XPS) is a helpful method to not only qualitatively and quantitatively analyze surfaces but also to determine the chemical state of the present elements, i.e., if they are in a metallic or oxidized state. During XPS, an X-ray irradiates the specimen surface, which causes the emission of electrons due to the photoelectric effect. The kinetic energy of the emitted electrons is then detected and can be correlated to a characteristic binding energy associated with the electron orbitals of the elements present. The information depth of this method is typically below 10 nm, while depth profiling can be performed using ion sputtering to remove surface layers. [116]

In this work, qualitative XPS measurements are performed on the surface of TiZrNbHfTa specimens stored in air at room temperature and after single-step oxidation in air at 600 °C. Measurements are either performed directly on the surface or after 200 min of sputtering with argon ions at 3 kV. Even with Ar sputtering, information depths of several micrometers cannot be reached. Therefore, the potential oxygen-enriched zone resulting from single-step oxidation of TiZrNbHfTa is analyzed based on a cross-section micrograph. In this case, a platinum mask is deposited on the micrograph to demarcate the region of interest from the surrounding and cover a potential surface oxide layer.

Figure 15 shows such a platinum mask before and after 200 min of sputtering. Sputtering for 200 min is appropriate to maintain the protective function of the platinum mask while cleaning the surface from potential oxygen contamination due to handling times in air. Additional XPS measurements are performed on a TiZrNbHfTa specimen after two-step oxidation, where the potential surface oxide layer is mechanically removed before the measurement in addition to 200 min of sputtering. This allows the investigation of a potential oxygen-enriched zone at a given depth. The XPS measurements are executed on a Physical Electronics PHI 5000 VersaProbe III XPS device at the Device Engineering KeyLab at the Bavarian Polymer Institute by Felix Baier, Experimental Physics XI, University of Bayreuth.

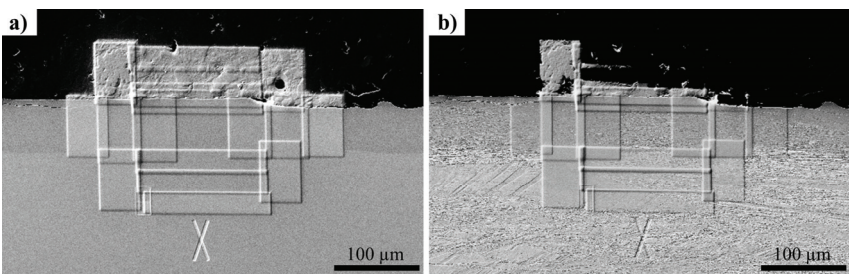

Figure 15: a) platinum mask deposited on a TiZrNbHfTa cross-section micrograph to demarcate a region of interest for XPS analysis before and b) after 200 min of sputtering with argon ions.

During X-ray diffraction analysis (XRD), an incident X-ray beam interacts with crystalline material and gets diffracted following the Braggs law. With known incident X-ray wavelength and measured diffraction angles 2Θ corresponding to diffraction reflexes, the interplanar

spacing d_{hkl} in a crystal lattice can be calculated. Based on the interplanar spacing, the lattice constants characteristic for the crystal system can be derived. [117]

In this work, XRD measurements are performed on a Bruker D8 discover using $CuK_{\alpha 1}$ monochromatic X-rays with a wavelength of 154.06 pm. A diffraction angle range from 20° to 80° is covered to study the surface of Ti6Al4V in the initial state and after performing the oxidation processes. This range is extended to 140° for the TiZrNbHfTa specimens. The step size is 0.01°, while the count time per step is adjusted between 0.5 s and 12 s depending on the specimen-specific signal gain. Based on the obtained diffractograms, phases are identified by performing a search/match operation with the software DIFFRAC.EVA, during which the measured diffractograms are compared with datasets registered in the PDF4+ ICDD database. In addition, the lattice constants of phases occurring in TiZrNbHfTa specimens are determined by the Rietveld refinement software TOPAS 4.2.

4.3.4 Reaction kinetics analysis

According to equations (4) and (5) on page 9, determining the reaction kinetics requires either measuring an area-specific mass change or layer thickness growth over time. In the case of Ti6Al4V, the mass change over time during single-step oxidation is monitored by manually measuring the weight of the specimens (20 x10 x 2 mm³) before and after oxidation at different oxidation durations. TGA is deployed in the case of TiZrNbHfTa specimens (5 x 5 x 1 mm³), as detailed in section 4.2.1.

The kinetics of oxide layer thickness growth is determined from cross-section micrographs of specimens after different oxidation durations. Four to eight SEM images per cross-section are considered and analyzed using the software OLYMPUS Stream Motion 2.3. As shown in Figure 16 a), each image is evaluated at more than 100 positions. The total oxide length evaluated per specimen is approx. 100 µm in the case of Ti6Al4V and approx. 400 µm in case of TiZrNbHfTa. If multilayered oxides occur, as in Figure 16 b), the total oxide layer thickness is considered for the reaction kinetics determination.

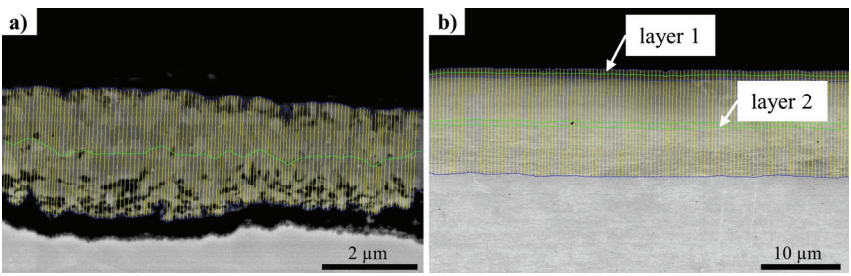

Figure 16: a) Ti6Al4V and b) TiZrNbHfTa oxide layers analyzed regarding their oxide layer thickness.

The experimental results are checked for significant deviations from the parabolic rate law before the rate constants are derived by fitting the experimental data.

4.3.5 Analysis of mechanical and tribological properties

A central aspect of determining the success of oxidation-induced surface hardening is the analysis of the surface hardness due to the different oxidation processes. The surface hardness is measured in HV0.5 using an Innovatest Falcon 500 Vickers hardness tester. Eighteen measurements are performed per specimen using a load of 0.5 kp. The mean values are provided with a 95 % confidence interval. In addition, twelve Vickers hardness measurements per specimen are realized with a Fischerscope HM 2000 microhardness tester at a load of 0.01 kp.

This device is also deployed to generate microhardness-depth profiles of the subsurface regions. For this purpose, a matrix of 20 x 20 measurement points is defined on cross-section micrographs. As shown in Figure 17, this matrix is rotated by an angle δ with regard to the specimen surface. This results in the depth resolution perpendicular to the surface being much better than the distance of 10 µm between the measurement points. Depth-controlled (0.2 µm) Martens hardness measurements are automatically performed at the defined locations.

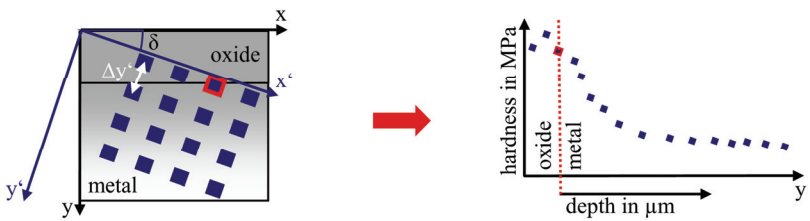

Figure 17: Schematic visualization of the hardness-depth profile determination using a matrix of measurement points rotated with regard to the specimen surface. Reference imprints are used to deduce the actual depth scale.

The adhesion of the layers obtained during oxidation of Ti6Al4V and TiZrNbHfTa is assessed using Rockwell indentation testing according to EN ISO 26443 [118]. During Rockwell indentation testing, an HRA Rockwell diamond cone impinges the surface for 10 s at 60 kp. The remaining imprint is then visually analyzed and its appearance classified concerning layer delamination. Figure 18 provides the four classes of layer adhesion defined in EN ISO 26443 [118]. Since the classification is not always unambiguous, six imprints per specimen are analyzed to provide an averaged impression.

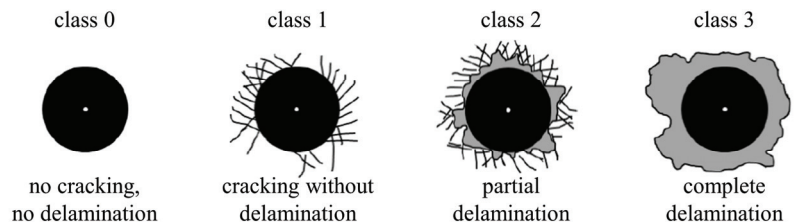

Figure 18: Layer adhesion classes for Rockwell indentation testing according to EN ISO 26443 [118].

Profilometry is used to compare the influence of the oxidation processes on surface roughness. A Mahr MarSurf PS 10 profilometer is used to determine the roughness parameters R_a and R_z from a topologic profile according to DIN EN ISO 4288 [119]. R_a is the arithmetic mean of all absolute profile height deviations with regard to a mean line [120]. R_z is the sum of the highest height and the lowest depth of a profile averaged based on five measurement intervals [120]. Six measurements are performed per specimen, yielding a mean value and the corresponding 95 % confidence interval.

For tribological testing, a knee joint wear tester was previously developed at the institute [9, 121, 122]. Figure 19 a) shows relevant potential degrees of freedom that exist between the upper femur and the lower tibia component in a human knee joint. In Figure 19 b), the variation of the occurring axial load, the flexion/extension, and the translation occurring during a step cycle according to ISO 14243-3 [123] are depicted.

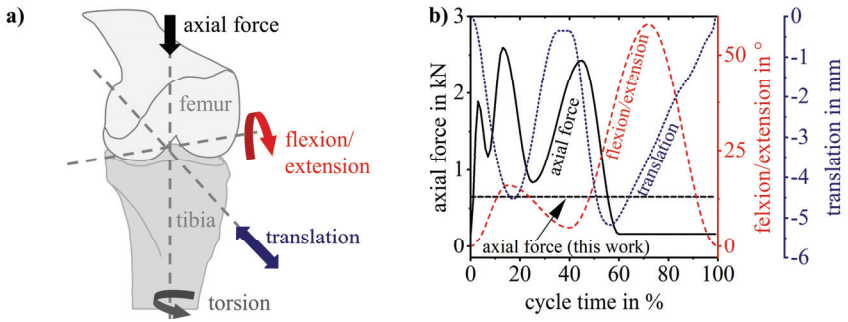

Figure 19: a) illustration of a knee joint consisting of a femur and a tibia component with its essential degrees of freedom and b) the variation of axial force, flexion angle, and translation during a standard human step cycle according to ISO 14243-3 [123] and realized in this work.

The knee-joint tribological tester shown in Figure 20 a) tries to mimic these conditions while a torsion between the femur and tibia component is neglected. A static load of 650 N replaces the cyclic axial load to facilitate the installation effort, as proposed in previous experiments [9]. The translatory movement is realized via an eccentric sheave mounted on a drive shaft. Analogously, the flexion/extension movement is realized via an eccentric sheave on the drive shaft, combined with a rack and pinion gear to convert the translatory movement into an oscillatory rotation.

The knee joint wear tester can be equipped with three test rigs to test three specimens parallelly. In this work, flat metallic specimens with a cylindric ultra-high-molecular-weight polyethylene (UHMW-PE) counterpart are used, as shown in Figure 20 b). Each test rig is connected to a cooling water system with deionized water, keeping the specimens at ambient temperature throughout the test run. One test run comprises a minimum of 500000 cycles according to ISO 14243-3 [123]. At a cycle frequency of 1 Hz, this leads to a test duration of approx. 1 week. After the test, the Ti6Al4V or TiZrNbHfTa specimens are qualitatively investigated using digital light optical microscopy.

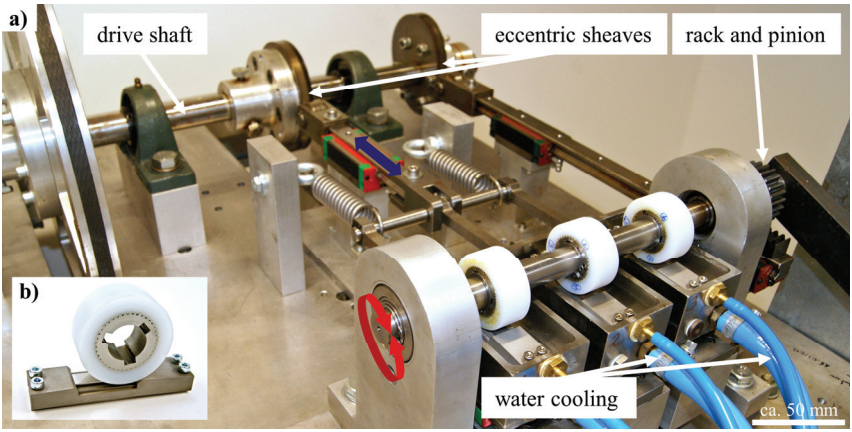

Figure 20: a) knee-joint tribological tester equipped with test rigs containing UHMW-PE cylinders running against flat metal specimens, which in b) are shown in more detail.

Calo wear testing is an alternative approach to evaluate tribological properties. Figure 21 a) shows the test setup according to ISO 26424 [124]. A drive shaft causes a ball to roll on a specimen. Assuming a slip-free shaft-ball contact, the sliding distance of the ball on the specimen can be calculated based on the shaft and ball dimensions, the rotation speed of the drive shaft, and the experiment time. Figure 21 b) depicts a typical wear crater resulting from calo wear testing in the case that the surface oxide layer is not protruded.

In this work, an Eifeler Calotest device is used with a steel ball of 20 mm diameter and 32.2 g weight. The normal force is 0.2 N and the sliding distance is 5.91 m, resulting from a test duration of 60 s at a drive shaft rotation speed of 170 min^{-1}. During each test run, 1 µm diamond suspension is applied once. Six wear craters are analyzed per specimen, yielding a mean value and the corresponding 95 % confidence interval. The chosen parameters ensure that, if present, an oxide layer is not protruded during testing. The oxide layer itself is considered homogeneous.

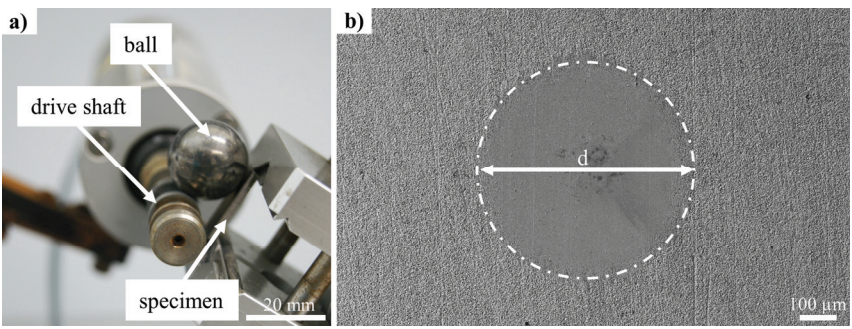

Figure 21: a) setup for Calo-wear testing and b) a typical wear crater analyzed via SE-SEM imaging.

Based on the diameter d of the wear crater, a wear coefficient K_c can be calculated [124]:

$$K_c = \frac{\pi d^4}{64 \cdot r \cdot s \cdot F_N} \tag{14}$$

K_c: *wear coefficient*
d: *diameter of the wear crater*
r: *radius of the ball*
s: *sliding distance*
F_N *normal force*

A Nanovea T50 ball-on-disk tribometer is used to determine the wear rate K_v of the specimens. As illustrated in Figure 22, a Si_3N_4 ball of 6 mm diameter is pressed against a rotating disk with a normal load of 5 N. Upon disk rotation, a wear trace with 5 mm radius is created in the case of Ti6Al4V. Due to the limited amount of TiZrNbHfTa available for testing, a 2 mm radius is chosen for this material. The sliding distance is 300 m for Ti6Al4V and 120 m for TiZrNbHfTa, such that the number of ball passes per given point on each wear trace is identical despite the different radii deployed for Ti6Al4V and TiZrNbHfTa. Based on the wear traces and their depth profiles compared to the initial surface, the volume loss can be calculated. A volume loss-based wear rate K_v can then be expressed according to equation (15) [4].

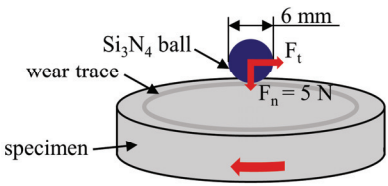

Figure 22: Illustration of the ball-on-disk setup used to determine the friction coefficient and wear rate of Ti6Al4V and TiZrNbHfTa specimens before and after different oxidation processes.

$$K_v = \frac{V}{s \cdot F_N} \tag{15}$$

K_v: *wear rate*
V: *volume wear loss*
s: *sliding distance*
F_N *normal force*

In addition, the setup continuously measures the frictional force F_t acting on the ball. This allows calculating the coefficient of friction μ according to equation (1) on page 2. The friction coefficients provided in this work are average values representing the whole experiment duration, including the running-in and steady-state-friction phases. All ball-on-disk measurements, including the wear trace analysis, calculation of the wear rates, and determination of the friction coefficients, are performed and provided by Beyza Öztürk, DECHEMA-Forschungsinstitut.

5 Experimental results

5.1 Oxidation of Ti6Al4V

Figure 23 shows the oxide layer thickness evolution during screening experiments performed on Ti6Al4V. While during the single-step process oxide layer spallation already occurs after 2 h at 780 °C (Figure 23 a)), much higher temperatures and durations can be deployed for the oxidation at reduced oxygen partial pressure (Figure 23 b)). The maximum tested temperature of 850 °C and a duration of 8 h still lead to the formation of an adherent oxide layer. This is why 680 °C is chosen to conduct further single-step oxidation experiments, as described in Table 7 (page 21). 850 °C is selected for the oxidation at reduced oxygen partial pressure, which keeps the oxidation duration needed to achieve a several micrometer thick oxide layer at a minimum and reduces the Ar gas consumption.

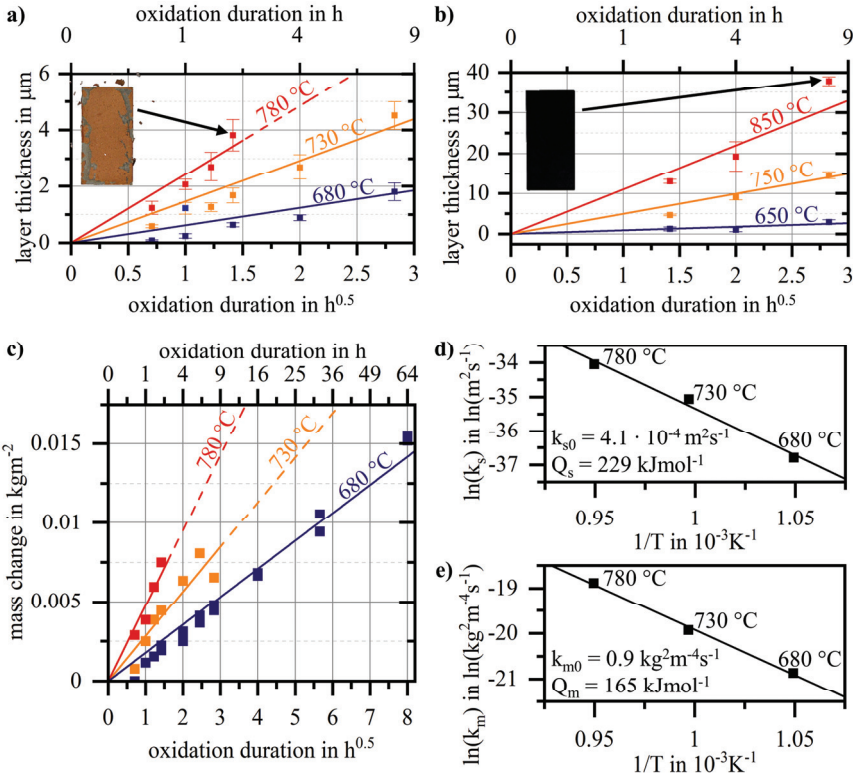

Figure 23: Layer thickness evolution over time during a) single-step oxidation of Ti6Al4V and b) oxidation at reduced oxygen partial pressure. c) provides the surface normalized mass change over time during single-step oxidation. In d), the Arrhenius plot related to the layer thickness evolution is shown, while e) is the Arrhenius plot based on the mass change.

Figure 23 c) shows the mass change curves over time corresponding to the layer thickness growth during single-step oxidation. Based on the evolution of layer thickness and mass change over time at 680 °C, 730 °C, and 780 °C, the respective reaction constants k_s and k_m can be derived from parabolic fits and are provided in Table 8. These reaction constants are used to create Arrhenius plots, as depicted in Figure 23 d) and e), from which the activation energies Q_s and Q_m are obtained according to equation (5) on page 9. The activation energy of layer growth Q_s for Ti6Al4V is 229 kJmol^{-1} with a factor k_{s0} of 4.1·10^{-4} m^{2}s^{-1}, and the activation energy of mass change Q_m is 165 kJmol^{-1} with a factor k_{m0} of 0.9 kg^{2}m^{-4}s^{-1}. In addition to the discrepancy between Q_s and Q_m, the calculated density change of the oxide layer (Table 8) is in no proportion to the density of TiO_2 rutile (4.23 g/cm³) or Ti6Al4V (4.4 g/cm³). This indicates that the oxide layer contains pores. Alternatively, a significant amount of oxygen is dissolved in Ti6Al4V instead of forming TiO_2. Both aspects are closer investigated in this section. Therefore, converting k_s into k_m or vice versa using equation (6) (page 10) is inappropriate.

Table 8: Rate constants k_s and k_m derived from parabolic fits of the layer thickness evolution and area-specific mass change over time during single-step oxidation of Ti6Al4V in the temperature range 680 °C - 780 °C and resulting $\Delta\rho(T)$ according to equation (6) on page 10.

temperature in °C	k_s in $10^{-16}\cdot m^2s^{-1}$	k_m in $10^{-9}\cdot kg^2m^{-4}s^{-1}$	$\Delta\rho(T)$ in g/cm³
680	1.1	0.9	2.86
730	5.9	2.2	1.93
780	16.3	6.3	1.97

The visual surface appearance of the Ti6Al4V specimens after their respective oxidation treatment is shown in Figure 24. A dark brownish surface occurs after the single-step process due to oxidation in air. A bright, mat, metallic surface obtained with the two-step process indicates a successful reduction of oxides previously formed during oxidation in air. The three-step process leads to a similar appearance to the single-step process. Oxidation at reduced oxygen partial pressure results in a black surface.

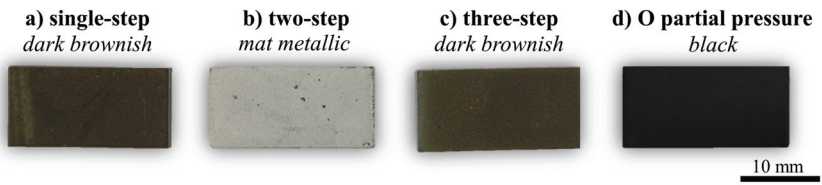

Figure 24: Images of Ti6Al4V specimens after a) single-step, b) two-step, c) three-step oxidation, and d) after oxidation at reduced oxygen partial pressure.

Figure 25 shows surface SEM images of the specimens of Figure 24 at two different magnifications. On a micrometer scale (Figure 25 a)-d)), the formation of elevated oxide grain clusters (arrow 1, Figure 25 a)), sticking out of the former even surface, can be observed during the single-step process. Despite a much smoother surface appearance, such former clusters can

still be identified after the two-step process (Figure 25 b)) while elevated clusters of oxide grains reappear after the three-step process (arrow 2, Figure 25 c)). Needle-shaped oxide grains developing during oxidation at reduced oxygen partial pressure do not form such elevated oxide grain clusters (Figure 25 d)).

Magnified excerpts reveal that fine, elongated, rod-shaped oxide grains (arrow 3, Figure 25 e)) and larger polyhedron-type oxide grains (arrow 4, Figure 25 e)) grow at the surface during single-step oxidation. In between, oxide grains of undefined shape occur. The fine, rod-shaped oxide grains are no longer present after the two-step process. Instead, only agglomerated polyhedron-type grains possessing a terraced structure (arrow 5, Figure 25 f)) are present. The surface resulting from the three-step process (Figure 25 g)) is very similar to the one after the single-step process. Oxidation at reduced oxygen partial pressure instead causes the formation of up to approx. 1 µm thick needle-shaped oxide grains at the surface (Figure 25 h)).

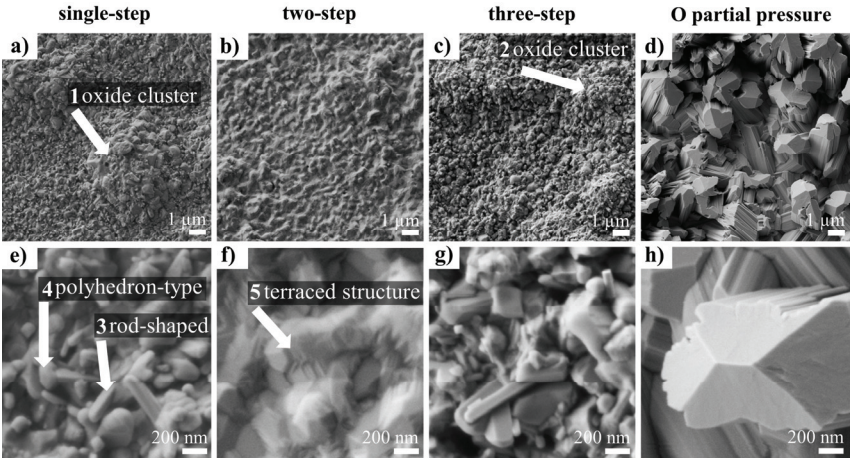

Figure 25: SE-SEM images of the surface topographies resulting from the a) single-step, b) two-step, and c) three-step process, as well as d) oxidation at reduced oxygen partial pressure, each with magnified excerpts e)-h). The spots marked with arrows are referenced in the text.

Figure 26 shows cross-section micrographs, including Ti, Al, and O EDS elemental mappings. The rod-shaped or polyhedron-type oxide grains observed after single-step oxidation are rich in Ti (arrow 1, Figure 26 a)) while the grains of undefined shape in-between are rich in Al (arrow 2, Figure 26 a)). The terraced, polyhedron-type grains resulting from the two-step process appear Al-rich and form only in the first ~250 nm perpendicular to the surface (arrow 3, Figure 26 b)). Like the single-step process, Ti-rich rod-shaped and polyhedron-type oxide grains occur at the surface after three-step oxidation with Al-rich grains of undefined shape in-between (arrow 4, Figure 26 c)). Oxidation at reduced oxygen partial pressure leads to the formation of a multilayered oxide layer. The needle-shaped oxide grains at the very top are rich in Ti (arrow 5, Figure 26 d)) followed by an intermediate Al-rich layer (arrow 6, Figure 26 d)) and another Ti-rich layer underneath.

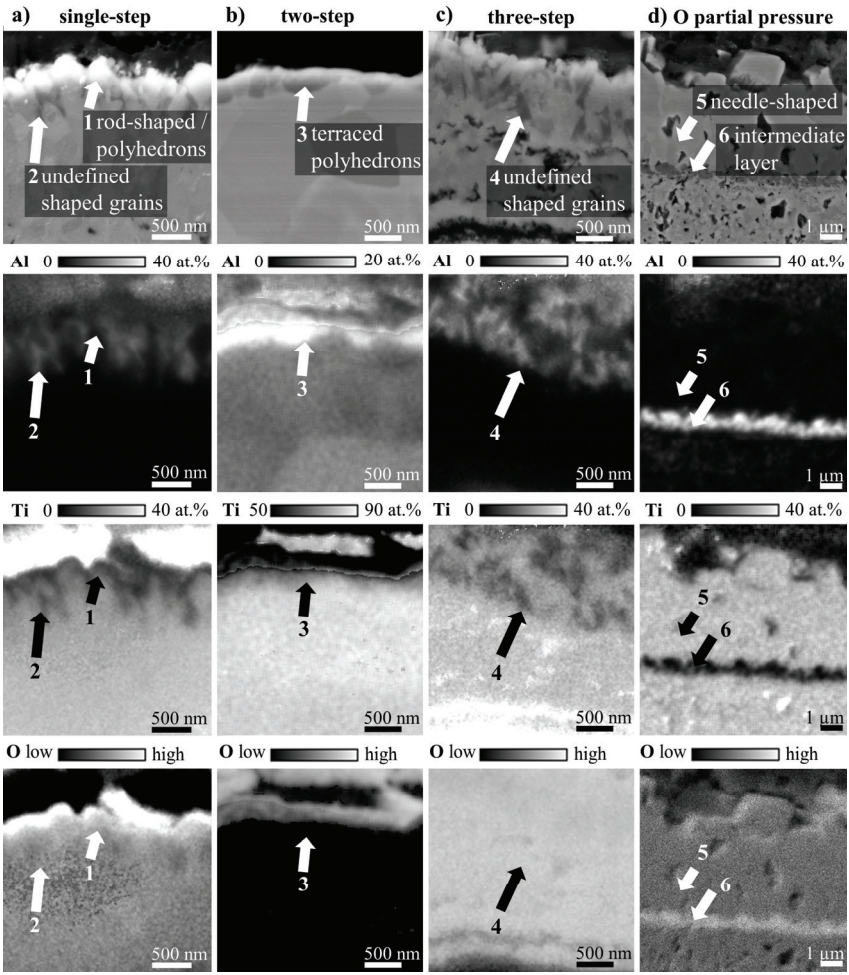

Figure 26: SE-SEM images and EDS elemental mappings of cross-section micrographs after a) single-step, b) two-step, and c) three-step oxidation, as well as d) after oxidation at reduced oxygen partial pressure (at a different magnification). The spots marked with arrows are referenced in the text.

Figure 27 provides the XRD diffractograms of the surface of unmounted Ti6Al4V specimens, each treated with one of the four studied oxidation processes. The oxide layer resulting from the single-step process dominantly consists of TiO_2 rutile (ICDD 00-021-1276) and minor amounts of α–Al_2O_3 (ICDD 01-070-5679). This indicates that the Ti-rich polyhedron-type and rod-shaped oxide grains identified during EDS analysis (Figure 26 a)) are TiO_2 oxides. The Al-rich grains of undefined shape are Al_2O_3. Due to an oxide layer thickness of only 2.5 ± 0.5 µm, peaks indicating the presence of α–Ti (ICDD 00-044-1294) can be attributed to the subsurface

region or substrate. After the two-step process, no oxide phases are identified. Instead, α–Ti and Ti_3Al (ICDD 00-052-0859) are found with Ti_3Al corresponding to the Al-rich grains observed during the EDS analysis (Figure 26 b)). The diffractogram of the specimen after three-step oxidation is similar to the one after single-step oxidation. In the case of oxidation at reduced oxygen partial pressure, α–Al_2O_3, related to the Al-rich intermediate layer (Figure 26 d)), and TiO_2 rutile are present. α–Ti is not identified since the X-rays do not penetrate the oxide layer of 13 ± 0.5 µm. None of the four diffractograms, even those revealing titanium, show the presence of β-Ti, indicating that the subsurface region is β-phase depleted.

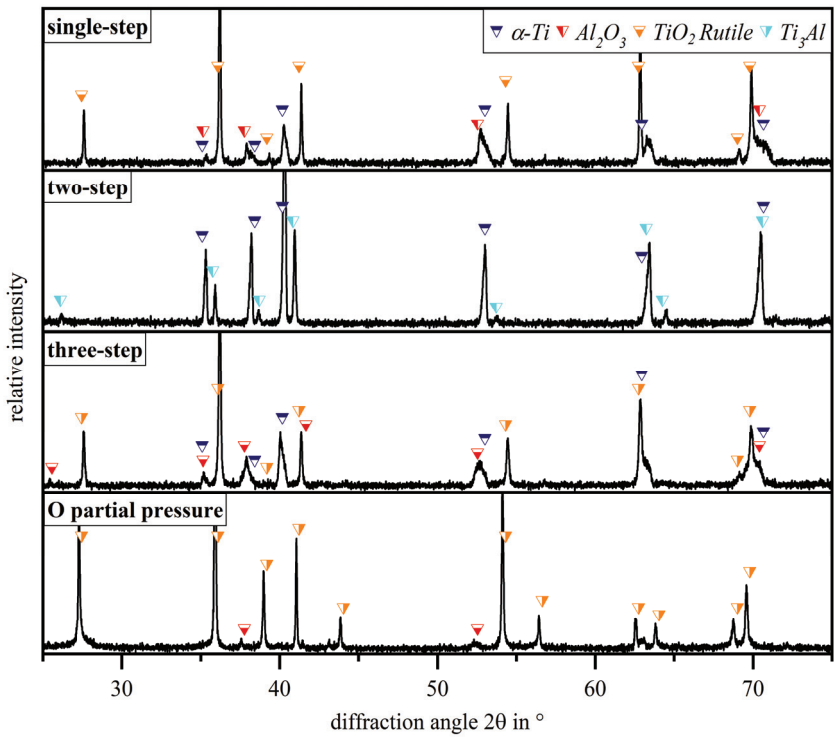

Figure 27: Surface XRD analysis of Ti6Al4V after single-step, two-step, and three-step oxidation, as well as after oxidation at reduced oxygen partial pressure with peaks identified based on the ICDD database.

As shown in Figure 28, the different oxidation processes impact the oxide layer morphology, if an oxide layer is present, and the subsurface microstructure. The oxide layer formed during the single-step process exhibits compact agglomerations of oxide grains in some regions while open pores accumulate preferably at the oxide-metal interface (arrow 1, Figure 28 a)). Instead of an oxide layer, darker appearing grains, previously identified as Ti_3Al, occur at the surface after two-step oxidation (arrow 2, Figure 28 b). A few micrometers beneath the surface, such darker

appearing Ti_3Al grains locally occur in the form of a lamella (arrow 3, Figure 28 b)). Furthermore, pores are visible at a depth of approx. 1 µm from the surface (arrow 4, Figure 28 b)). The three-step process, similar to the single-step process, leads to the formation of agglomerations of oxide grains. At the same time, open pores accumulate, preferably at the oxide-metal interface, leading to a partial detachment of the oxide layer (arrow 5, Figure 28 c)). In contrast to that, the multilayered oxide layer obtained during oxidation at reduced oxygen partial pressure shows only a few larger pores in the region of needle-shaped oxide grains (arrow 6, Figure 28 d)) while fine, closed, homogeneously distributed pores occur in the oxide layer in touch with the metal (arrow 7, Figure 28 d)). The overview images (Figure 28 e)-h)) reveal that the relative amount of the brighter appearing β-Ti phase (arrow 8, Figure 28 e)) is reduced in the subsurface region compared to the Ti6Al4V substrate. The two-step process even leads to a surface near region completely depleted in β-Ti (arrow 9, Figure 28 f)).

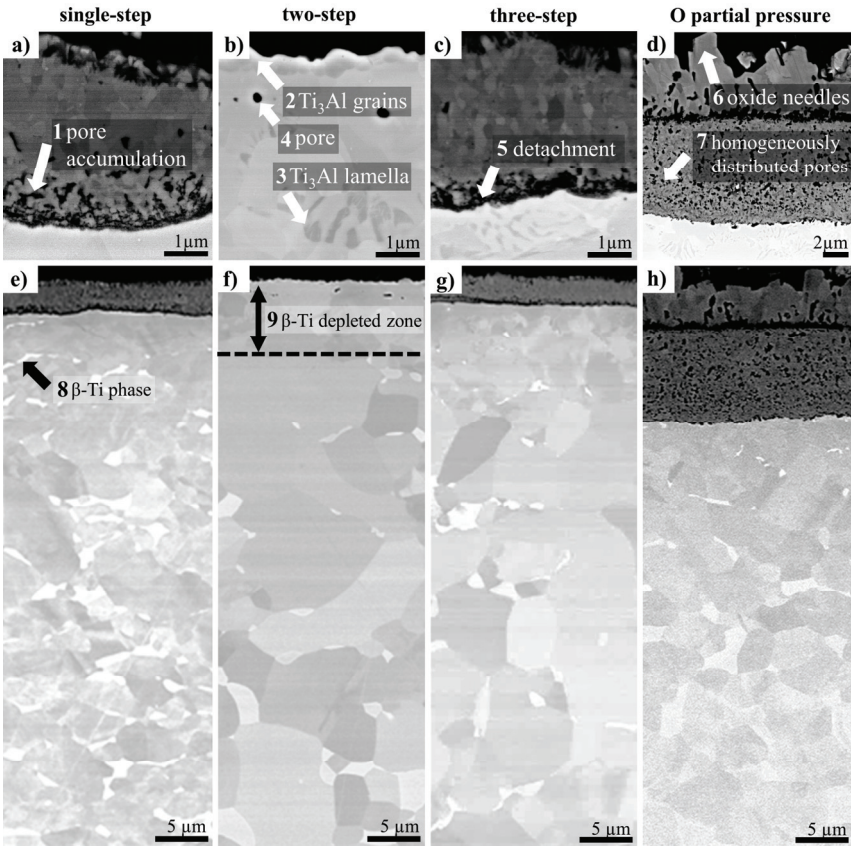

Figure 28: BSE-SEM micrographs of Ti6Al4V specimens after a) single-step, b) two-step, and c) three-step oxidation, as well as d) after oxidation at reduced oxygen partial pressure including overview images (e)-h)). The spots marked with arrows are referenced in the text.

Figure 29 provides SE-SEM images of Ti6Al4V after single-step oxidation and oxidation at reduced oxygen partial pressure, corresponding to the BSE-SEM images shown in Figure 28. Since SE-SEM images reveal a topography contrast, they confirm that the regions appearing black at the oxide-substrate interface in the BSE-SEM images after single-step and three-step oxidation (Figure 28 a) and c)) indeed are pores or indicate an oxide layer detachment. This is not the case for Ti6Al4V oxidized at reduced oxygen partial pressure, where fine, closed pores occur homogeneously distributed in the oxide layer (Figure 29 b)).

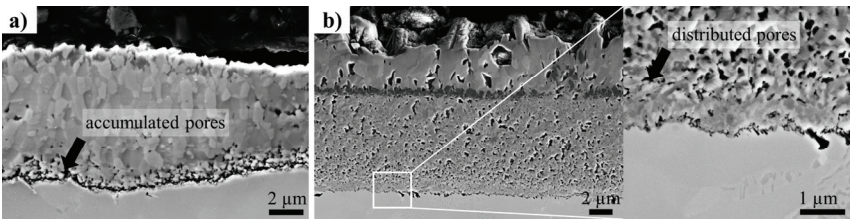

Figure 29: SE-SEM micrographs of Ti6Al4V specimens after a) single-step oxidation and b) oxidation at reduced oxygen partial pressure.

The subsurface regions, starting from either the oxide-metal or air-metal interface, are more closely investigated using GDOES and microhardness measurements. Figure 30 shows the obtained oxygen concentration-depth profiles compared to the microhardness-depth profiles. Starting from an effective initial concentration of 20 at.% at the oxide-metal interface, the oxygen concentration gradually decreases in the case of the single-step process, reaching 0 at.% at a depth of 20 µm. A much higher oxygen penetration depth of 85 µm is reached with the two-step process. The oxygen concentration at the air-metal interface is below 10 at.% and the profile is near-linear. Higher oxygen concentration values occurring in the first 0.5 µm are a measurement artifact caused by the GDOES plasma ignition (see page 23). The additional final oxidation step during the three-step process mainly affects the first 20 µm. The concentration-depth profile initially shows a gradual decrease starting from the effective initial concentration of 20 at.%. After 20 µm, it follows the near-linear trend observed for the two-step process. Oxidation at reduced oxygen partial pressure leads to oxygen diffusion depths comparable to the two-step and three-step processes, yet the oxygen enrichment in the first 20 µm is significantly higher.

All microhardness-depth profiles show a similar trend to the oxygen concentration-depth profiles. The maximum hardness of ~9 GPa is reached close to the oxide-metal interface in the case of the single-step and three-step process as well as after oxidation at reduced oxygen partial pressure. Due to the comparably lower oxygen concentration at the air-metal interface after two-step oxidation, the maximum hardness is also lower and only ~6 GPa.

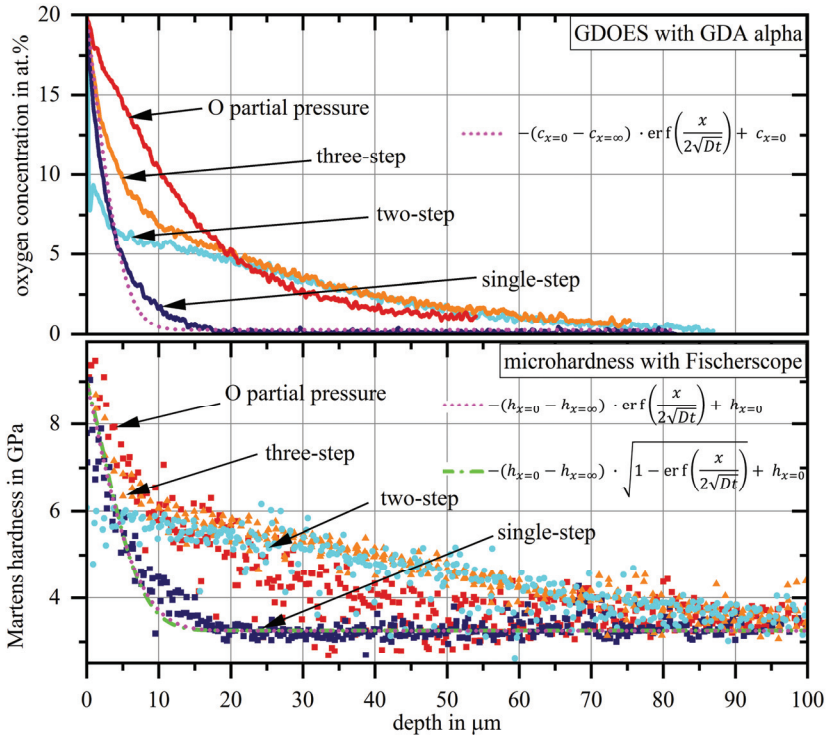

Figure 30: Subsurface oxygen concentration- and microhardness-depth profiles of Ti6Al4V after single-step, two-step, and three-step oxidation, as well as oxidation at reduced oxygen partial pressure. The curves are plotted starting at either the oxide-metal or the air-metal interface. In addition, fits of the profiles resulting from single-step oxidation are provided based on equation (9) on page 11 and equations (10) and (11) on page 12.

Table 9 provides the apparent oxygen diffusion coefficients in Ti6Al4V derived from the oxygen concentration- and hardness-depth profile after single-step oxidation (Figure 30). The diffusion coefficient is obtained by fitting equation (9) on page 11 to the oxygen concentration-depth profile. In the case of the hardness-depth profile, both possible model equations discussed in the literature (equation (10) and equation (11) on page 12) are considered, resulting in a comparably good fit. All three derived diffusion coefficients have a similar order of magnitude. They are further discussed and set in contrast to literature values in the discussion section on page 67.

Table 9: Oxygen diffusion coefficients derived from the hardness- and oxygen concentration-depth profiles after single-step oxidation of Ti6Al4V (Figure 30).

	***D* from GDOES profile**	***D* from hardness profile**	***D* from hardness profile**
fit model	equation (9)	equation (10)	equation (11)
$c_{x=0}$ / $h_{x=0}$	20 at.% (preset)	9 GPa (preset)	9 GPa (preset)
$c_{x=\infty}$ / $h_{x=\infty}$	0.3 at.%	3.3 GPa	3.3 GPa
R^2	0.9662	0.7174	0.7127
D	$1.3 \cdot 10^{-16}$ m^2s^{-1}	$1.1 \cdot 10^{-16}$ m^2s^{-1}	$2.9 \cdot 10^{-16}$ m^2s^{-1}

In Figure 31, the Martens hardness values obtained from the hardness-depth profiles after single-step, two-step, and three-step oxidation are correlated with the corresponding oxygen concentrations from the respective oxygen concentration-depth profiles (Figure 30). In direct comparison, the assumption of a parabolic correlation relationship (Figure 31 b)) yields a better goodness of fit compared to a linear relationship (Figure 31 a)) and can best represent the experimentally determined correlation between oxygen concentration and hardness.

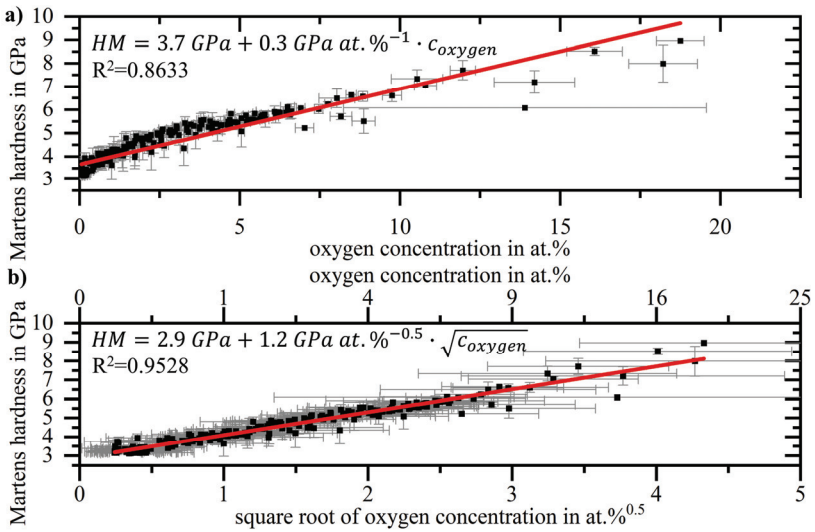

Figure 31: Correlation of Martens hardness (HM) and oxygen concentration in Ti6Al4V based on the single-step, two-step, and three-step oxygen concentration- and hardness-depth profiles (Figure 30) assuming an a) linear and b) parabolic relationship. The data points are the mean values with their standard deviation obtained from a discretization needed during the correlation procedure.

5.2 Oxidation of TiZrNbHfTa

5.2.1 Characterization of initial as-cast, rolled, and rolled & annealed TiZrNbHfTa

Table 10 provides the elemental compositions of as-cast, rolled, and rolled & annealed TiZrNbHfTa after manufacturing (section 4.1). In all cases, the composition is equimolar in good approximation. No significantly different process-dependent oxygen or nitrogen contamination is detected.

Table 10: Elemental concentrations of bulk as-cast, rolled, and rolled & annealed TiZrNbHfTa determined via XRF (Ti, Zr, Nb, Hf, Ta) and carrier hot gas extraction analysis (O, N).

material	Ti in at.%	Zr in at.%	Nb in at.%	Hf in at.%	Ta in at.%	O in at.%	N in at.%
as-cast	18.4	21.7	20.8	20.1	18.6	0.25	0.11
rolled	18.0	21.2	21.1	19.9	19.4	0.31	0.15
rolled & annealed	18.0	20.4	21.0	20.2	19.9	0.34	0.13

Figure 32 shows the XRD diffractograms obtained for as-cast, rolled, and rolled & annealed TiZrNbHfTa. As far as assessable with an XRD analysis [42], all manufacturing routes lead to single-phase bcc material. The observed peak positions are in good agreement with the reflexes reported for single-phase bcc1 TiZrNbHfTa in the ICDD database (ICDD 04-018-541) [125].

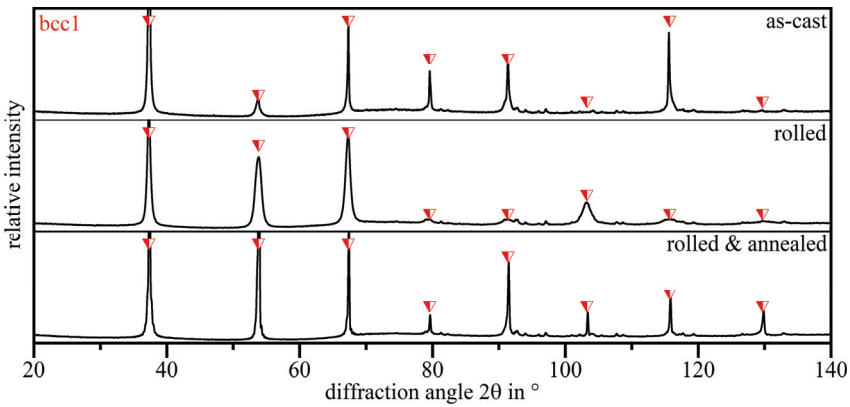

Figure 32: XRD-analysis of as-cast, rolled, and rolled & annealed TiZrNbHfTa in the initial state with the indicators marking the database peak positions of single-phase bcc1 TiZrNbHfTa (ICDD 04-018-541) [125].

Figure 33 shows the initial microstructure of as-cast, rolled, and rolled & annealed TiZrNbHfTa. On average, the grain size in the as-cast material is 90 ± 33 µm with subgrains visible in the BSE-SEM images (arrow 1, Figure 33 a)). In contrast, the rolled material exhibits an ultrafine-grained microstructure with a grain size of 200 ± 120 nm. These ultrafine grains are narrow, elongated, and preferentially orientated parallel to the surface (arrow 2, Figure 33 b)). This is due to heavy plastic deformation during cold rolling. During the annealing

of the rolled material at 1200 °C, recrystallization takes place. The microstructure of rolled & annealed material is characterized by pronounced grains similar to the as-cast material. In this case, the grain size is 47 ± 22 µm, and no subgrains are visible (Figure 33 c)).

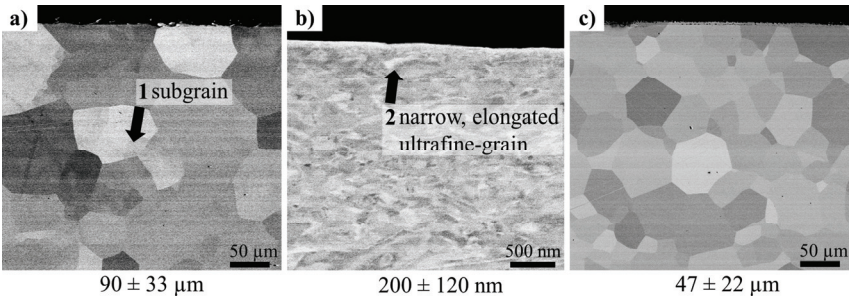

Figure 33: BSE-SEM images of cross-section micrographs revealing the initial microstructure of a) as-cast, b) rolled, and c) rolled & annealed TiZrNbHfTa. The spots marked with arrows are referenced in the text.

5.2.2 Single-step oxidation of TiZrNbHfTa

Microstructure-dependent oxidation behavior

The microstructure hugely impacts the oxidation behavior of TiZrNbHfTa, as shown in Figure 34. While the thermogravimetric analysis at 600 °C reveals a continuous mass gain over 24 h in the case of rolled material, except for a minor number of spalled particles (arrow 1, Figure 34), the as-cast and rolled & annealed material exhibit a mass loss up from 4 h. This mass loss is attributed to catastrophic oxidation causing severe spallation and hence to particles departing the measurement crucible.

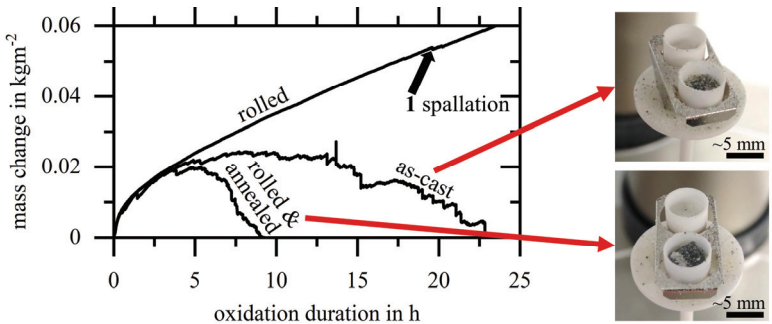

Figure 34: Thermogravimetric analysis revealing the mass change per surface area during oxidation (600 °C, in synthetic air) of as-cast, rolled, and rolled & annealed TiZrNbHfTa. Arrow 1 is referenced in the text.

Figure 35 shows the microstructure of as-cast, rolled, and rolled & annealed TiZrNbHfTa after oxidation at 600 °C. Remarkable changes are visible compared to the initial microstructure

(Figure 34). In all three material states, a darker-appearing region of ~50 µm depth is apparent at the surface of the specimens in the BSE-SEM images, indicating the presence of a light element such as oxygen. In the as-cast material (Figure 35 a)), the grain and subgrain boundaries appear darker than the initial state. A similar darker appearance of the grain boundaries is also visible in the case of rolled & annealed material (Figure 35 c)). The corresponding qualitative EPMA oxygen mappings (Figure 35 d)-f)) indicate that the oxygen concentration is highest directly at the surface of all three materials. An oxygen-enriched zone of up to 58 µm can be identified. This is in agreement with the darker-appearing surface region identified in the BSE-SEM images. The EPMA mappings do not indicate an oxygen enrichment in the substrate underneath the oxygen-enriched zones.

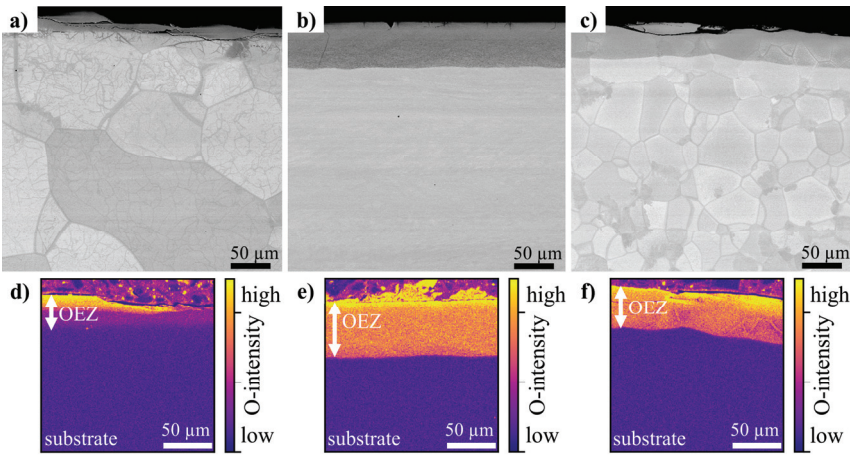

Figure 35: BSE-SEM images of cross-section micrographs of a) as-cast, b) rolled, and c) rolled & annealed TiZrNbHfTa after oxidation (600 °C, 24 h, in air) with d)-f) corresponding qualitative EPMA oxygen mappings revealing an oxygen-enriched zone (OEZ) beneath the surface. The EPMA oxygen mappings are provided by Beyza Öztürk, DECHEMA-Forschungsinstitut.

Detailed BSE-SEM images of the non-oxygen-enriched substrate are shown in Figure 36. At the grain and subgrain boundaries of as-cast TiZrNbHfTa, the formation of at least one new phase is visible. Occasionally, the formation of one or potentially several new phases also occurs within the grains (Figure 36 a)). In the case of rolled material, a two-phase microstructure on the nanometer scale is present in the substrate (Figure 36 b)). Similar to as-cast material, one or several new phases forming at the grain boundaries or occasionally within the grains can also be observed for rolled & annealed TiZrNbHfTa. Here, the multi-phased regions at the grain boundaries exhibit a lamellar microstructure and sometimes extend from the grain boundaries into the grains (Figure 36 c)). Figure 36 d) shows the X-ray diffractograms corresponding to the non-oxygen-enriched substrate. It is apparent that for the as-cast and the rolled & annealed material, a new bcc2 phase and a new hcp1 phase are present beside the initial bcc1 phase. In the case of rolled TiZrNbHfTa, the initial bcc1 phase no longer occurs,

indicating a complete decomposition into a new bcc2 and a new hcp1 phase. Due to its potential capability to dissolve high amounts of oxygen, the hcp1 phase is expected to appear darker in the BSE-SEM images. The lattice parameters of the identified bcc1, bcc2, and hcp1 phase are listed in Table 11.

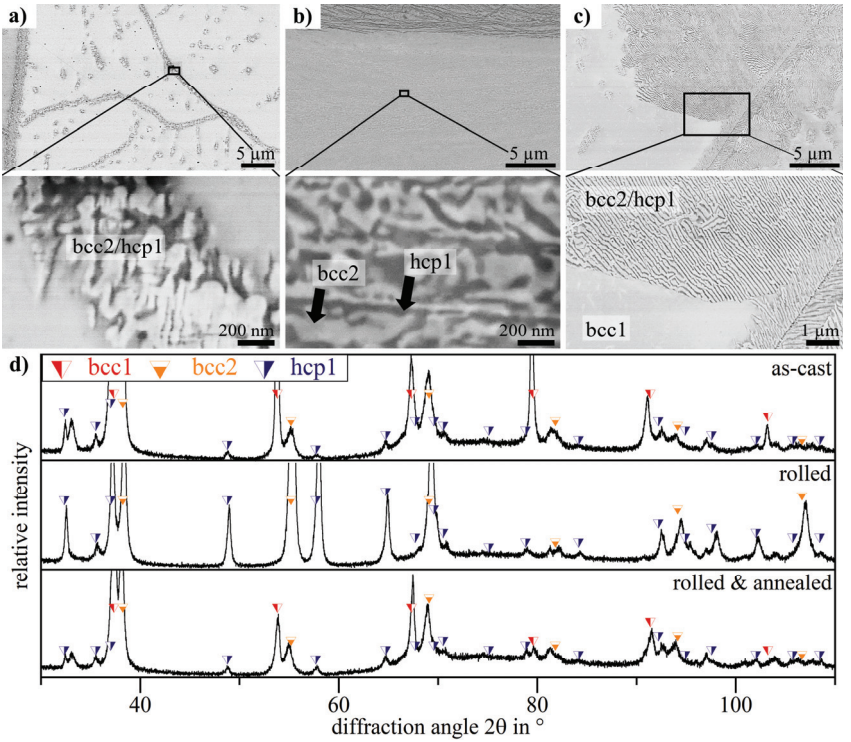

Figure 36: Substrate regions of a) as-cast, b) rolled, and c) rolled & annealed TiZrNbHfTa after oxidation (600 °C, 24 h, in air) analyzed via BSE-SEM and d) corresponding XRD analysis.

Table 11: Dominant phases with their respective space groups and lattice parameters according to a Rietveld refinement model performed with the XRD data shown in Figure 36 d).

phase	space group	lattice parameter in pm
bcc1	Im-$\bar{3}$m	340.7
bcc2	Im-$\bar{3}$m	333.8
hcp1	P63/mmc	c= 505.9, a=320.2 c/a=1.580

Figure 37 shows the oxygen-enriched zone of as-cast TiZrNbHfTa after oxidation in air at 600 °C for 24 h, visible in SEM images and an EPMA mapping. A potential surface oxide layer

is visible (arrow 1, Figure 37), containing several cracks oriented parallel to the specimen surface. Parts of this layer are already spalled off during oxidation or metallographic preparation. At the surface near grain and subgrain boundaries, an enhanced oxygen presence is observed, indicating accelerated, localized oxygen ingress along grain boundaries (arrow 2, Figure 37).

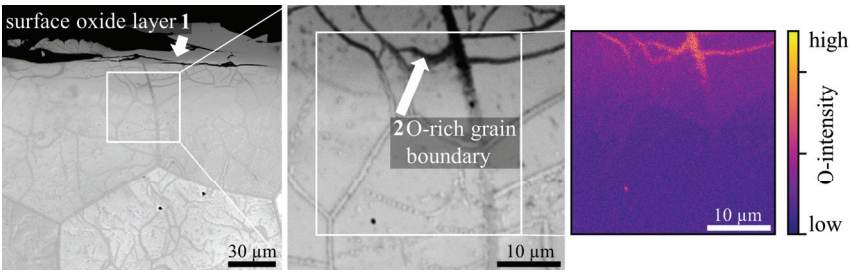

Figure 37: BSE-SEM micrographs of the surface region of as-cast TiZrNbHfTa after oxidation (600 °C, 24 h, in air) with a corresponding qualitative EPMA oxygen mapping. The spots marked with arrows are referenced in the text.

Figure 38 shows BSE-SEM images of the oxygen-enriched zone of rolled TiZrNbHfTa after oxidation in air at 600 °C for 24 h. Only a few minor cracks are visible at the surface (arrow 1, Figure 38). A compact, micrometer-sized, darker-appearing potential surface oxide layer is present (arrow 2, Figure 38). The oxygen-enriched zone extending towards the substrate shows a two-phase microstructure. This structure is comparable to the one identified in the substrate of rolled TiZrNbHfTa (Figure 36 b)) with the difference that the material contrast between the two phases is significantly enhanced. This indicates the preferential allocation of a light element, such as oxygen, in only one of the two observed phases (arrow 3, Figure 38).

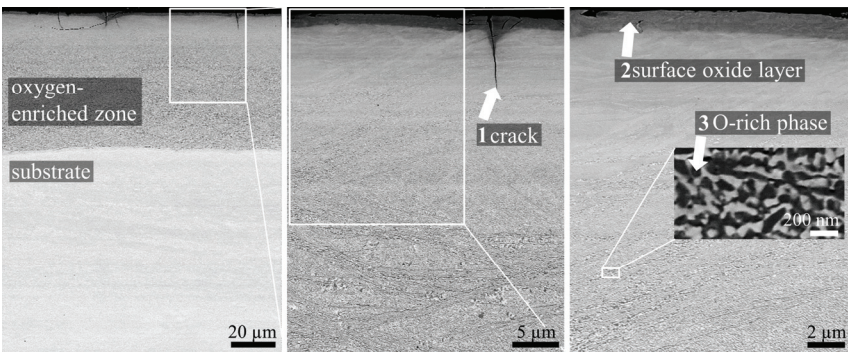

Figure 38: BSE-SEM micrographs of the surface region of rolled TiZrNbHfTa after oxidation (600 °C, 24 h, in air). The spots marked with arrows are referenced in the text.

Figure 39 shows a rolled TiZrNbHfTa specimen after 24 h and 48 h of oxidation at 600 °C in an atmosphere with a reduced oxygen partial pressure of ~10^{-19} Pa. The presence of a surface

oxide layer, the microstructure, and the layer thickness obtained are comparable to the result after oxidation in air (Figure 38). Also, the occurrence of minor cracks in the subsurface region is comparable, while the cracks increase after prolonged oxidation (Figure 39 b)).

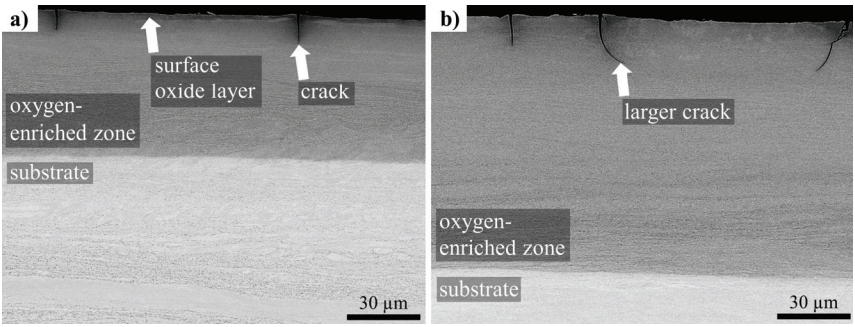

Figure 39: BSE-SEM micrographs of the surface region of a) rolled TiZrNbHfTa after 24 h and b) 48 h of oxidation at 600 °C in an atmosphere with a reduced oxygen partial pressure of ~10^{-19} Pa. The spots marked with arrows are referenced in the text.

Figure 40 depicts BSE-SEM images of the oxygen-enriched zone of rolled & annealed TiZrNbHfTa after oxidation in air at 600 °C for 24 h. A darker-appearing compact surface oxide layer is mainly detached (arrow 1, Figure 40). This can already happen during the oxidation process, as observed during thermogravimetric analysis (Figure 34), or during metallographic preparation. In the oxygen-enriched zone underneath, intergranular cracks occur (arrow 2, Figure 40). Similar to the substrate, also the oxygen-enriched zone exhibits at least two visible phases. These phases either occur close to the grain boundaries in the form of lamella (arrow 3, Figure 40) or precipitates inside the grains (arrow 4, Figure 40).

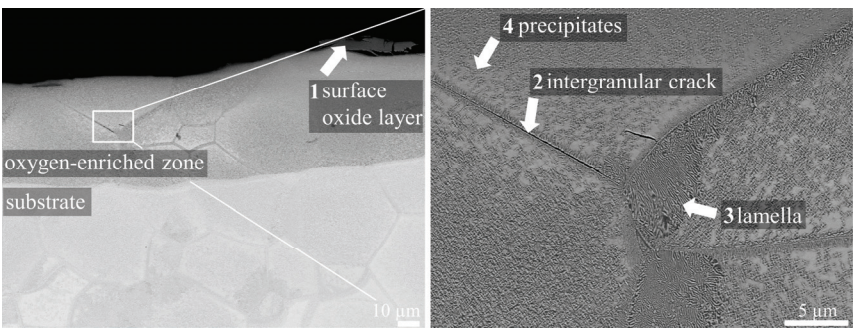

Figure 40: BSE-SEM micrographs of the surface region of rolled & annealed TiZrNbHfTa after oxidation (600 °C, 24 h, in air). The spots marked with arrows are referenced in the text.

Surface and subsurface characterization of rolled TiZrNbHfTa after oxidation

The thermogravimetric analysis and the microstructural characterization before and after oxidation of as-cast, rolled, and rolled & annealed TiZrNbHfTa indicate that oxidation to obtain a hard, adherent surface layer is only promising in the case of rolled material. A need to distinguish between single-step oxidation and oxidation at reduced oxygen partial pressure is not indicated, according to Figure 39. Therefore, the behavior of rolled TiZrNbHfTa during single-step oxidation is studied in more detail, addressing, amongst others, the obtained elemental composition at the surface and in the subsurface region, the oxygen concentration- and hardness-depth profiles, and the reaction kinetics.

Figure 41 shows an elemental EDS mapping of a rolled TiZrNbHfTa specimen after oxidation in air at 600 °C for 24 h coated with a gold layer before the oxidation process. The EDS mapping reveals that this gold layer is still present at the surface even after oxidation of the specimen (arrow 1 in Au-map, Figure 41). This indicates that outward diffusion of metallic elements towards the metal-air interface is not significant during the oxidation process. Instead, oxygen diffuses through the gold layer towards and into the metal. The potential compact, micrometer-sized surface oxide layer underneath the gold layer (arrow 2 in O-map, Figure 41) is also identifiable in the BSE-SEM cross-section micrographs (arrow 2, Figure 38, page 44). It exhibits a higher oxygen concentration than the below oxygen-enriched zone.

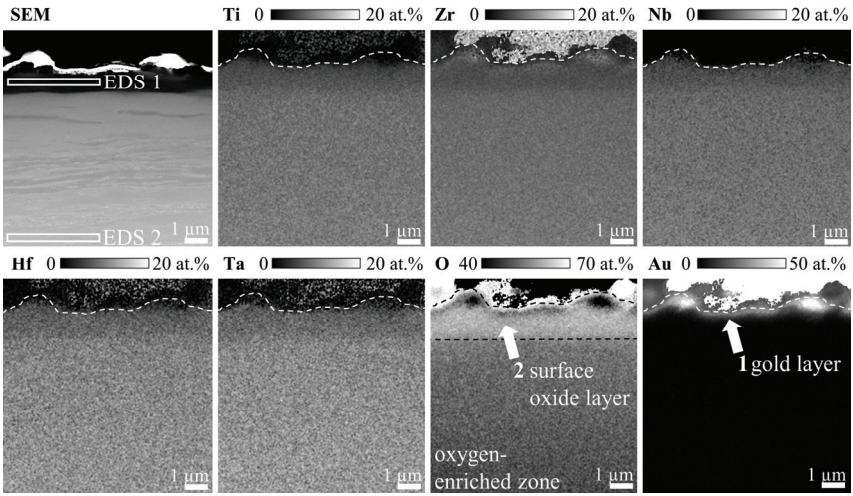

Figure 41: Elemental EDS mappings of the oxygen-enriched surface region of rolled TiZrNbHfTa after oxidation (600 °C, 24 h, in air). A gold layer is deposited on the specimen before oxidation to identify a preferred oxide layer growth direction. The spots marked with arrows are referenced in the text.

According to the elemental quantification presented in Table 12, the oxygen concentration in the compact surface layer is 67 at.%, while it is 48 at.% in the oxygen-enriched zone

underneath. Both oxygen concentrations are higher than the known oxygen solubility limits of the metallic alloying elements in TiZrNbHfTa (section 2.4.2, page 11), indicating the formation of oxides. However, on average, the metallic alloying elements maintain their equimolar ratio in the compact surface oxide layer and the oxygen-enriched zone underneath.

Table 12: Elemental concentrations of the compact surface oxide layer (region EDS1 in SEM image in Figure 41) and the beneath oxygen-enriched zone (region EDS2 in SEM image in Figure 41) after oxidation (600 °C, 24 h, in air) of rolled TiZrNbHfTa.

element	concentration (region EDS 1) in at.%	concentration (region EDS 2) in at.%
Ti	7	10
Zr	6	10
Nb	6	10
Hf	7	11
Ta	7	11
O	67	48

Figure 42 a) reveals the NRA oxygen concentration-depth profile of rolled TiZrNbHfTa after 8 h of oxidation at 600 °C in air, determined by Pascal Berger, Université Paris-Saclay, CEA, CNRS, NIMBE. The oxygen concentration is expressed in terms of oxygen stoichiometry x in $Ti_1Zr_1Nb_1Hf_1Ta_1O_x$, with the metallic elements maintaining their equimolar ratio. Based on the cross-section NRA mapping, the compact surface oxide layer has an oxygen stoichiometry of ~7.5. Under the assumption of an equimolar metal composition, which is valid according to the previously performed EDS analysis (Table 12), this is equivalent to an oxygen concentration of 60 at.%. Each metal is present with a concentration of 8 at.%. The NRA measurement directly on the surface oxide layer yields an oxygen stoichiometry of ~11, equivalent to an oxygen concentration of 69 at.%.

In the oxygen-enriched zone underneath the surface oxide layer, the oxygen stoichiometry gradually decreases according to the NRA cross-section mapping until a depth of 30 µm, where it levels out at ~3.5. Given an equimolar composition regarding the metallic elements, this oxygen stoichiometry corresponds to an oxygen concentration of 41 at.%. At a depth of 30 µm, the oxygen stoichiometry decreases drastically, reaching zero at a depth of 40 µm. In addition to the oxygen concentration-depth profile, Figure 42 a) also provides the microhardness-depth profile. The trend reflected in the microhardness-depth profile is similar to the oxygen stoichiometry-depth profile with the exemption that the hardness decrease over depth in the oxygen-enriched zone tends to follow a linear trend. Compared to the initial rolled TiZrNbHfTa, also depicted in Figure 42 a), a higher substrate hardness is obtained. The drop of oxygen stoichiometry and hardness at a depth of 30 µm correlates well with the visible contrast change in the SEM image of the corresponding cross-section micrograph (Figure 42 b)).

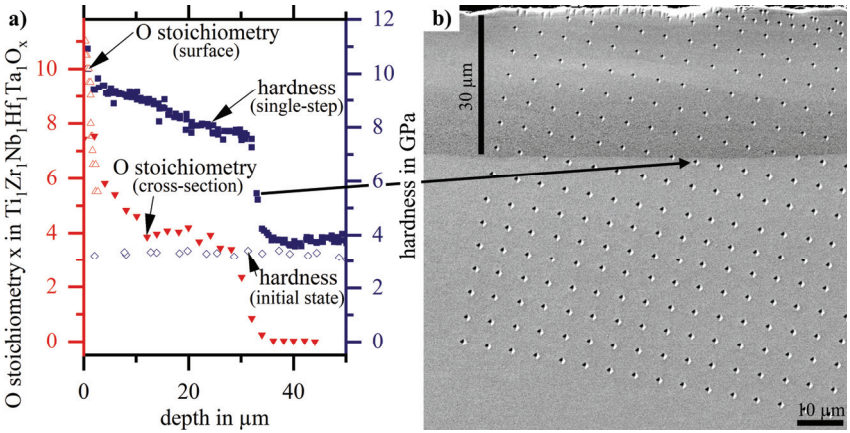

Figure 42: a) oxygen stoichiometry-depth profile determined via NRA on the specimen surface and measured via mapping a cross-section micrograph of rolled TiZrNbHfTa after single-step oxidation (600 °C, 8 h, in air). The corresponding microhardness-depth profile and the microhardness-depth profile of rolled TiZrNbHfTa in initial state are provided in addition. b) shows a SE-SEM image of the imprints caused by the microhardness measurements, clearly revealing the presence of an oxygen-enriched zone. NRA oxygen stoichiometry data are provided by Pascal Berger, Université Paris-Saclay, CEA, CNRS, NIMBE.

Similar to the EDS results (Table 12), the oxygen stoichiometry-depth profile of rolled TiZrNbHfTa after oxidation implies the presence of oxides in the compact surface layer and the oxygen-enriched zone underneath. Nevertheless, the X-ray diffractogram in Figure 43, obtained via surface XRD analysis with an angle-dependent information depth << 10 µm, does not provide sufficiently clear reflexes to allow an unambiguous identification of any crystal structures and hence their associated oxides. Despite a measurement time of 2 s per step, the peak-to-background ratio is poor and the lower angle peaks are characterized by a peak width of several degrees, including severe peak overlapping. This implies that long-range ordered oxide crystal structures are not dominant neither in the compact surface oxide layer nor in the underlying oxygen-enriched zone.

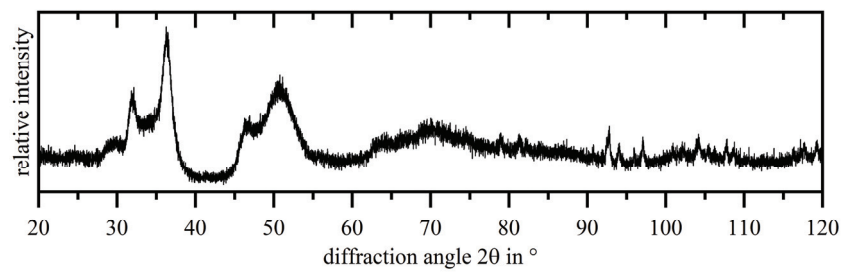

Figure 43: X-ray diffractogram obtained from surface XRD-analysis of rolled TiZrNbHfTa after oxidation (600 °C, 24 h, in air).

Figure 45 shows SE-SEM images revealing the surface topography resulting from single-step oxidation of rolled TiZrNbHfTa in air at 600 °C for 8 h. Scratches dominate the topography. These scratches are due to the grinding down to P1200 grinding paper performed during specimen preparation before the actual oxidation step (section 4.1). Hence, the surface topography appears to be unaffected by single-step oxidation. In contrast to, e.g., Ti6Al4V, no distinguishable surface oxide grains form. In agreement with Figure 34 on page 41, spallation is not observed after oxidation at 600 °C for 8 h in air.

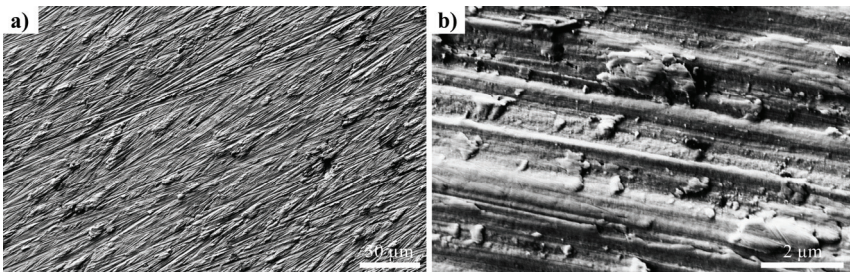

Figure 44: a) SE-SEM of the surface topography resulting from single-step oxidation of rolled TiZrNbHfTa (600 °C, 8 h, in air) and b) a higher magnified SE-SEM image.

Due to the absence of distinguishable oxide grains with long-range crystalline order, the XRD analysis cannot provide any information on which oxides actually form directly at the surface. An XPS analysis is an alternative approach that does not rely on the crystal structure but can identify potential oxides based on the measured characteristic binding energies. Figure 45 provides the characteristic binding energies of Ti, Zr, Nb, Hf, and Ta obtained during XPS analysis. Figure 45 a) shows that oxide formation on TiZrNbHfTa already occurs within minutes of air contact at room temperature. The characteristic binding energies imply the presence of TiO_2, ZrO_2, Nb_2O_5, HfO_2, and Ta_2O_5. Nevertheless, all elements can also be found in metallic state, except for Ti, where a high signal noise occurs. For Zr and Hf, more atoms are present in oxidized than metallic states, which is vice versa for Nb and Ta. In consequence, the native oxide layer is rich in ZrO_2 and HfO_2. This matches the expectation based on the Ellingham-Richardson diagram (Figure 5, page 8), according to which ZrO_2 is the most stable oxide, followed by HfO_2. After more than a week of air contact at room temperature (Figure 45 b)), the oxidized state is dominant for all elements. The XPS measurements confirm that TiZrNbHfTa is capable of forming a native oxide layer at room temperature. Oxidation at 600 °C for 1 h (Figure 45 c)) causes all surface atoms to be present in oxidized state. To reveal if internal oxides occur in the oxygen-enriched zone, an XPS analysis of a masked cross-section, which covers the already analyzed surface oxide layer with platinum to avoid a signal contribution of the surface oxides (Figure 15 on page 25), is performed with rolled TiZrNbHfTa after oxidation in air at 600 °C for 24 °h (Figure 45 d)). In the oxygen-enriched zone, Ti, Nb, and Ta are only present in metallic state. Instead, Zr and Hf dominantly occur in oxidized state with only some atoms still being present in metallic state, i.e., internal ZrO_2 and HfO_2 oxides form.

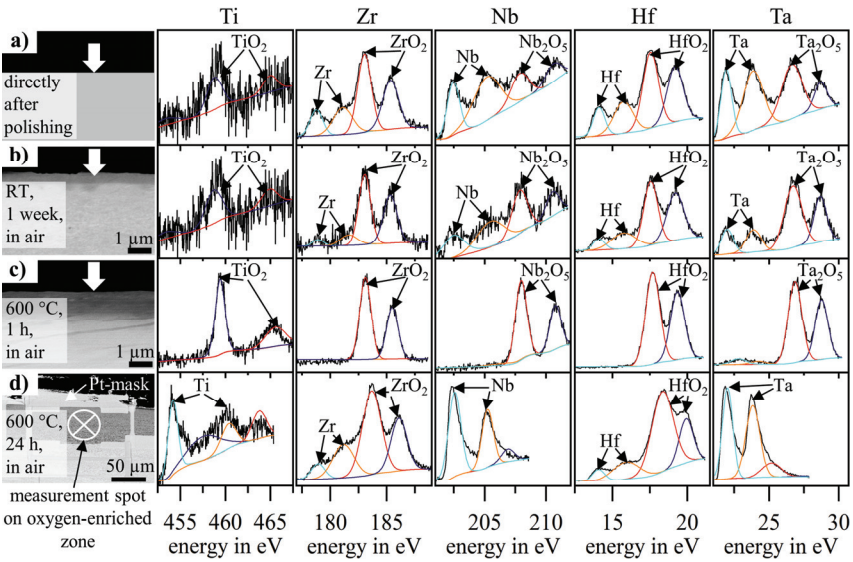

Figure 45: Characteristic binding energies (relative intensities) obtained using XPS analysis on the surface of a) rolled TiZrNbHfTa directly after polishing, b) more than one week with air contact at room temperature (RT) after polishing, c) after oxidation (600 °C, 1 h, in air), and d) on a masked cross-section of rolled TiZrNbHfTa after oxidation (600 °C, 24 h, in air). The XPS data are provided by Felix Baier, University of Bayreuth.

Figure 46 shows the surface area-specific mass change and the thickness evolution of the oxygen-enriched zone over time during oxidation between 550 °C and 650 °C. The thickness determination of the oxygen-enriched zone includes the surface oxide layer, typically not exceeding 2 µm. In good approximation, the mass change and the growth of the oxygen-enriched zone follow a parabolic rate law in the studied time-temperature regime. Only after prolonged oxidation at 650 °C spallation, and hence, a deviation from the parabolic behavior occurs. Table 13 provides the temperature-dependent reaction constants k_m and k_s derived from parabolic fits of the experimental data according to equation (4) on page 9. Based on these reaction constants, the Arrhenius plots depicted in Figure 46 b) and d) are obtained. Following equation (5) on page 9, the activation energy of mass change Q_m of 178 kJmol^{-1} with a factor k_{m0} of 796.6 kg^{2}m^{-4}s^{-1} is obtained. The activation energy Q_s describing the growth of the oxygen-enriched zone is 139 kJmol^{-1} with a factor k_{s0} of 6.7·10^{-6} m. Under the assumption of volume constancy of the specimens, the rate constants k_m are converted into rate constants k_s by determining a temperature-dependant average density change $\Delta\rho(T)$,which is then used for the conversion according to equation (6) on page 10. Figure 46 e) visualizes the density change $\Delta\rho(T)$ due to oxygen ingress into the specimen. In Fig f), a combined Arrhenius plot including the rate constants k_s obtained from the conversion is shown, yielding an activation energy Q_{sc} of 143 kJmol^{-1} and a factor k_{sc0} of 1.2·10^{-5} m.

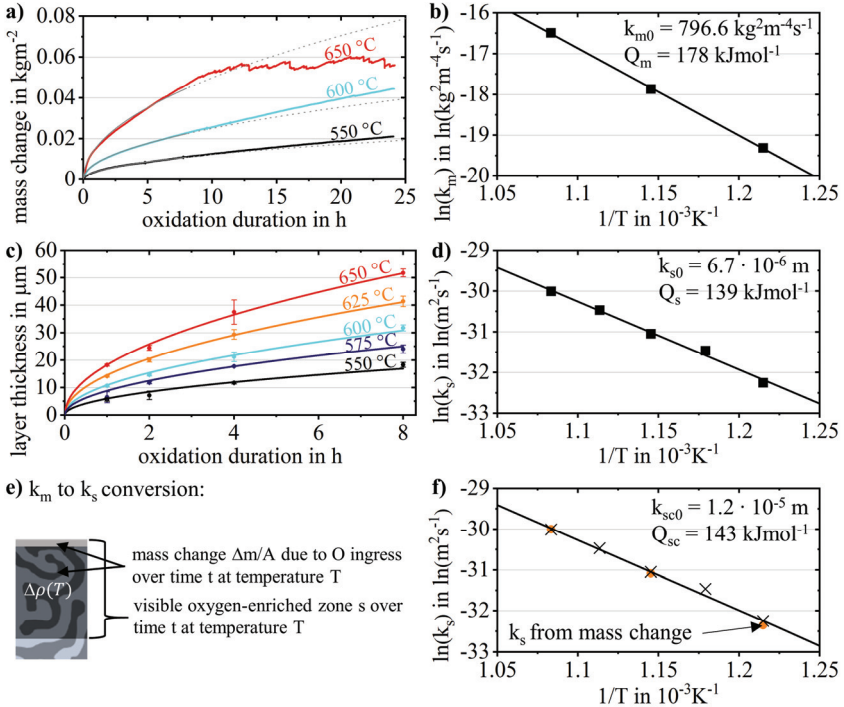

Figure 46: a) thermogravimetric analysis of rolled TiZrNbHfTa revealing the surface area-specific mass change over time during oxidation at 550 °C, 600 °C, and 650 °C in synthetic air with b) the corresponding Arrhenius plot. c) shows the evolution of an oxygen-enriched zone over time during oxidation in the temperature range of 550 °C - 650 °C with d) the corresponding Arrhenius plot. e) visualizes the density change $\Delta\rho(T)$ used for the conversion of k_m values into rate constants k_{sc}, yielding the combined Arrheniusplot shown in f). Reprinted from Dickes et al. [126] with permission from Elsevier, Elsevier © 2023.

Table 13: Mass-related rate constants k_m and thickness-related rate constant k_s derived from parabolic fits of the area-specific mass change and the thickness evolution of an oxygen-enriched zone over time during oxidation in the temperature range of 550 °C - 650 °C. The converted rate constants k_{sc}, derived from k_m values, are also provided.

temperature in °C	k_m in $10^{-8}\cdot kg^2m^{-4}s^{-1}$	k_s in $10^{-14}\cdot m^2s^{-1}$	k_{sc} **from** k_m in $10^{-14}\cdot m^2s^{-1}$
550	0.5	1.0	0.9
575	-	2.1	-
600	2.0	3.2	3.2
625	-	5.9	-
650	7.6	9.3	9.4

5.2.3 Two-step oxidation of TiZrNbHfTa

SEM microstructure characterization

In the first step, the microstructure of TiZrNbHfTa after two-step oxidation is analyzed. Figure 47 shows cross-section BSE-SEM images of rolled TiZrNbHfTa after two-step oxidation. Four distinct regions can be identified. At the surface, the micrometer-sized surface oxide layer observed after the single-step process is still visible (arrow 1, Figure 47). Underneath, grains of 1 - 2 µm size are visible, with darker-appearing precipitates in between (arrow 2, Figure 47). This region extends to a depth of 25 µm, after which larger grains with lamella form (arrow 3, Figure 47). The darker-appearing lamella are mainly present close to or at the grain boundaries of the larger grains. Deeper towards the substrate, grains typically larger than 50 µm size with a microstructure similar to the one observed for the rolled & annealed state (Figure 35 c), page 42) occur (arrow 4, Figure 47).

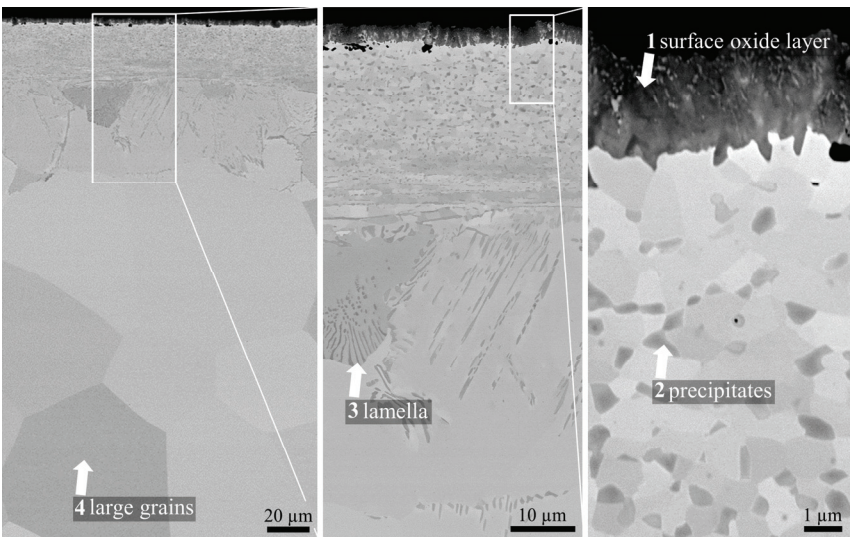

Figure 47: BSE-SEM images of the surface region of rolled TiZrNbHfTa after two-step oxidation (550 °C, 24 h, in air + 1200 °C, 1 h, vacuum + quenching). The spots marked with arrows are referenced in the text.

Figure 48 provides SE-SEM images depicting the surface topography resulting from two-step oxidation. Other than after the single-step process (Figure 44, page 49), scratches from the grinding procedure during specimen preparation are not visible. Instead, oxide grains with an average grain size of 0.8 µm can be identified. Along a network of narrow lines, elevated clusters of grains form (arrow 1, Figure 48 a)).

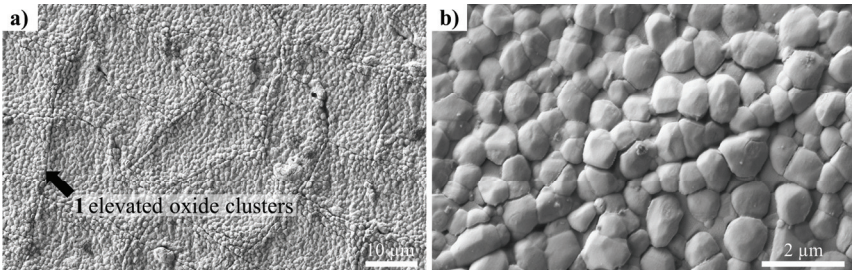

Figure 48: a) SE-SEM overview image of the surface topography resulting from two-step oxidation of rolled TiZrNbHfTa (550 °C, 24 h, in air + 1200 °C, 1 h, vacuum + quenching) with b) a higher magnified SEM image. The spot marked with an arrow is referenced in the text.

Chemical and crystallographic analysis of the subsurface region

The microstructural characterization reveals the occurrence of precipitates in a matrix phase. These precipitates and the matrix phase are studied in detail using EDS, APT, XPS, and XRD. Figure 49 shows an elemental EDS mapping, in the first place, confirming a micrometer-sized surface oxide layer (arrow 1 in O-map, Figure 49). Internal oxidation is present up to a depth of 2 µm underneath the surface oxide layer because the oxygen concentration locally exceeds 30 at.% (arrow 2 in O-map, Figure 49). The oxygen concentration in precipitates more than 2 µm away from the surface oxide layer (arrow 3 in O-map, Figure 49) does not indicate the presence of oxides. These precipitates are enriched in Zr, Hf, and O compared to the surrounding matrix grains, while they are depleted in Nb and Ta and, to a smaller extent, in Ti.

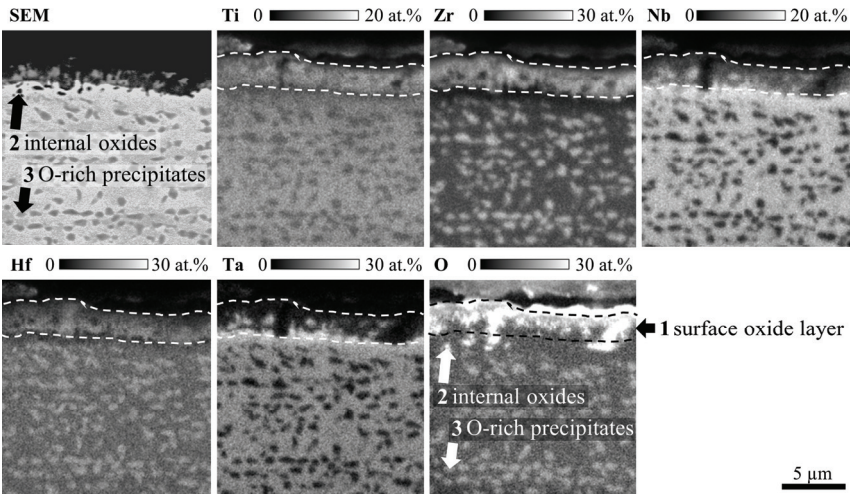

Figure 49: Elemental EDS mappings of the surface and subsurface region of rolled TiZrNbHfTa after the two-step process. Spots marked with an arrow are referenced in the text.

Figure 50 provides a line scan extracted from the elemental mapping (Figure 49), reflecting the compositional deviations between matrix grains and precipitates. It is worth noting that while significant oxygen concentration differences occur between matrix and precipitates, an overall decrease of oxygen concentration within the depicted 15 µm is barely noticeable.

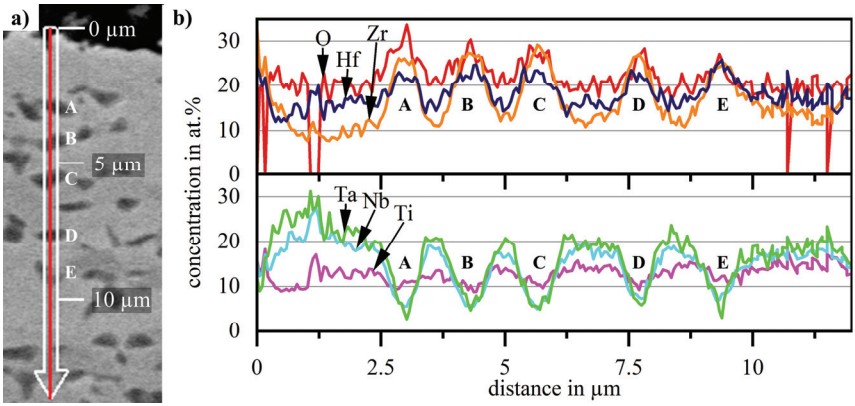

Figure 50: a) SEM image showing the location and width of an EDS line scan of the subsurface region after two-step oxidation of rolled TiZrNbHfTa, based on Figure 49, and b) the concentration-depth profiles of Ti, Zr, Nb, Hf, Ta, and O starting at the oxide-metal interface.

Figure 51 shows that even the lamella forming nearby or at the grain boundaries deeper towards the substrate, at a depth of ~30 µm, have a composition similar to the surface near precipitates.

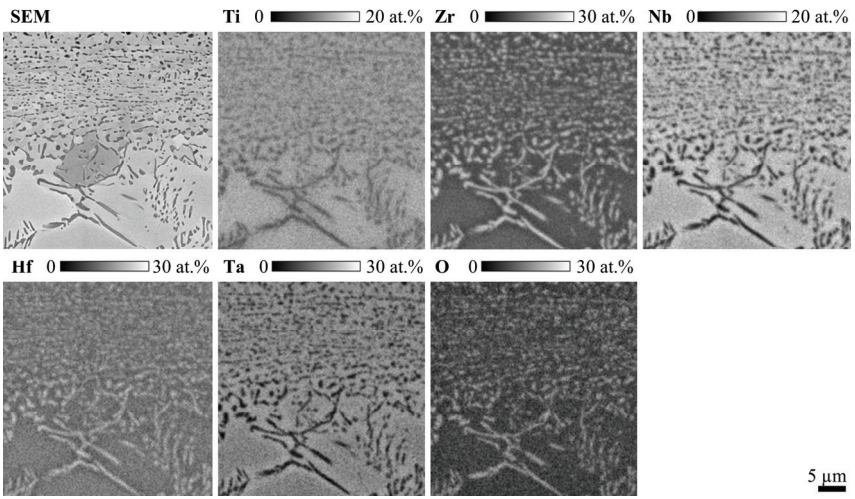

Figure 51: Elemental EDS mappings of the subsurface region of rolled TiZrNbHfTa after two-step oxidation, including the region with lamella forming nearby or at grain boundaries of larger grains in a depth of ~30 µm.

Table 14 lists the elemental composition of the matrix and the precipitates approx. 5 µm from the oxide-metal interface. The respective compositions are determined by averaging nine EDS point measurements.

Table 14: Elemental composition of the matrix and precipitates in rolled TiZrNbHfTa after two-step oxidation averaged from nine EDS point measurements in approx. 5 µm distance from the oxide-metal interface provided with the standard deviation.

elements	matrix composition in at.%	precipitate composition in at.%
Ti	15 ± 1	11 ± 1
Zr	11 ± 1	29 ± 4
Nb	19 ± 2	5 ± 2
Hf	15 ± 1	22 ± 1
Ta	19 ± 2	6 ± 2
O	21 ± 3	28 ± 3

Figure 52 shows representative excerpts of the analyzed APT needle tips prepared from the matrix region and the precipitates in approx. 5 µm distance from the oxide-metal interface. A cubic volume is used for the evaluation of the matrix composition (Figure 52 a)), while the depicted needle volume (Figure 52 b)) is used in the case of a precipitate. The multidirectional concentration profiles derived from the analyzed material volume indicate that the matrix and the precipitates are homogeneous also on a nanometer scale and that the atoms are statistically distributed.

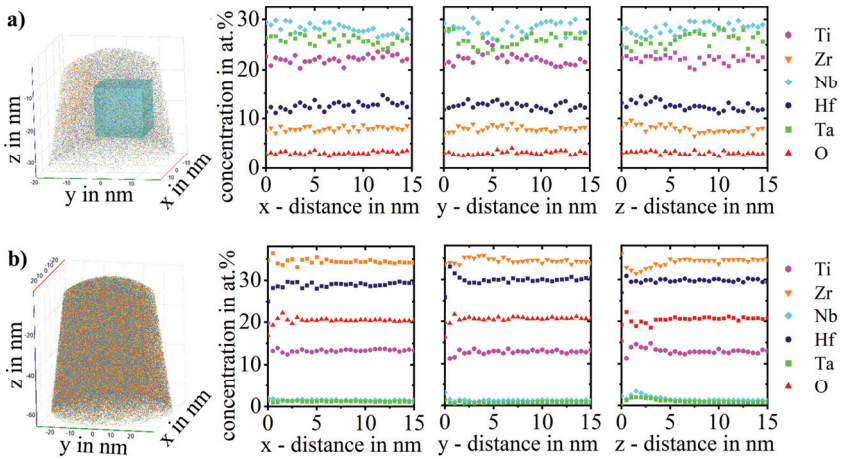

Figure 52: APT multidirectional elemental composition profiles on a nanometer scale in a) the matrix (cubic volume) and b) a precipitate (depicted needle tip volume) of rolled TiZrNbHfTa after the two-step process in approx. 5 µm distance from the oxide-metal interface. APT data are provided by Yujun Zhao, Ruhr University Bochum.

The averaged elemental compositions of the analyzed matrix and precipitate volume are given in Table 15. While the trend of the precipitates being rich in Hf, Zr, and O and simultaneously

being depleted in Nb and Ta is identical to the EDS measurements, the absolute values of the APT analysis differ. This is especially true for the oxygen concentration, which appears to be overestimated in the case of the EDS analysis at the expense of the titanium concentration. Such an overestimation of the oxygen concentration is due to a peak overlap of the O K_{α} and the Ti $L_{\beta 3}$ characteristic energies in the EDS spectrum. In Addition, during EDS, a surface oxide layer forming during specimen handling in air is also reflected in the determined signal, increasing the measured oxygen concentration. All in all, the APT results are more reliable.

Table 15: Elemental compositions of matrix and precipitates in rolled TiZrNbHfTa after two-step oxidation derived from APT measurements in approx. 5 µm distance from the oxide-metal interface. APT data are provided by Yujun Zhao, Ruhr University Bochum.

elements	**matrix composition** in at.%	**precipitate composition** in at.%
Ti	22.5	13.5
Zr	8.0	34.8
Nb	28.5	1.4
Hf	12.4	29.2
Ta	25.7	0.8
O	2.9	20.3

Figure 53 depicts an elemental composition profile derived from the APT data by investigating a cylindrical volume perpendicularly penetrating the matrix-precipitate interface. As previously shown, the elemental concentrations within the matrix and the precipitates are constant. Close to the interface, the matrix is disproportionately rich in Nb and Ta and poor in Hf and Zr. While the matrix close to the interface is already depleted in Ti, the Ti concentration increases directly at the interface before reaching the lower, constant Ti concentration of the precipitate.

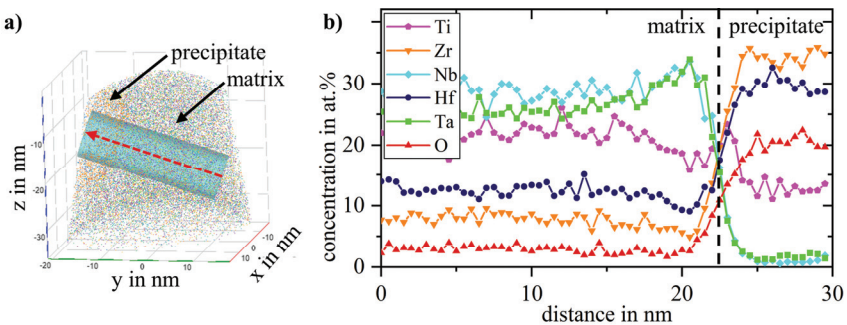

Figure 53: a) APT of a needle tip covering parts of the matrix and a precipitate of rolled TiZrNbHfTa after two-step oxidation and b) elemental concentration profiles derived from a cylindrical volume perpendicularly penetrating the matrix-precipitate interface as indicated in a). APT data are provided by Yujun Zhao, Ruhr University Bochum.

Figure 54 shows the results of the XPS analysis of the precipitates and the matrix after removing the surface oxide layer. All five metallic elements in TiZrNbHfTa are dominantly present in metallic state. Only in the case of Zr and Hf, minor peaks corresponding to the characteristic

binding energies of ZrO_2 and HfO_2 are present. Despite the sputtering with argon ions performed before the measurement, remaining oxygen atoms in the vacuum atmosphere cause the occurrence of ZrO_2 and HfO_2 due to the high oxygen affinity of Zr and Hf. An actual presence of oxides in the precipitates is unlikely when setting the energy spectra in contrast to the results obtained on TiZrNbHfTa immediately after polishing, where the short handling time in air already causes Zr and Hf to be dominantly in oxidized state (Figure 45 a), page 50).

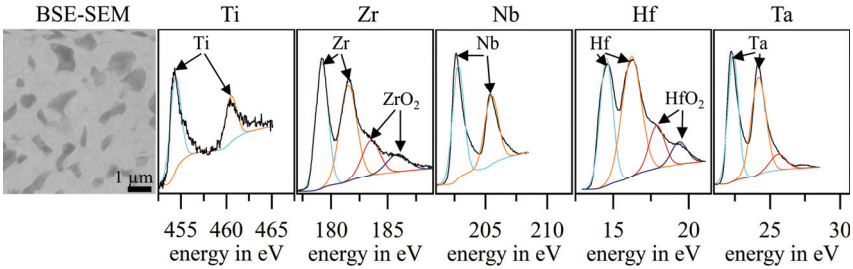

Figure 54: Characteristic binding energies (relative intensities) obtained via surface XPS analysis of rolled TiZrNbHfTa after the two-step process. The surface oxide layer is removed before the measurement such that the matrix and precipitates are analyzed, as shown in the SEM image.

Figure 55 shows the X-ray diffractogram of a rolled TiZrNbHfTa specimen after two-step oxidation. Similar to the XPS analysis, the first ~5 µm of the specimen are removed before the measurement to primarily analyze the matrix and precipitates, not the surface oxide layer. Three major phases are identified in the diffractogram comprising two bcc phases and one hcp phase.

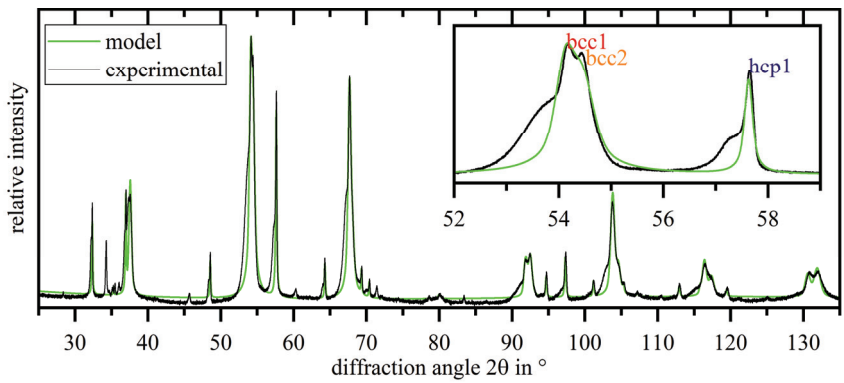

Figure 55: X-ray diffractogram of the surface of rolled TiZrNbHfTa after two-step oxidation and removal of the surface oxide layer such that the matrix, precipitates, and substrate are analyzed.

The lattice parameters of these phases, obtained by Rietveld analysis, are given in Table 16. While the bcc phase is in agreement with the lattice parameters previously observed for bcc1 TiZrNbHfTa (section 5.2.1, page 40; section 5.2.2, page 41), the lattice parameters for the bcc2

phase and the hcp1 phase are larger than the ones observed after single-step oxidation of TiZrNbHfTa (Table 11, page 43). Additionally, the magnified excerpt of the diffractogram in Figure 55 shows pronounced peak tails at the lower angle side of both, hcp and bcc peaks. The Rietveld refinement model does not cover these peak tails.

Table 16: Dominant phases with their respective space groups and lattice parameters according to a refinement model using the XRD data shown in Figure 55.

phase	space group	lattice parameter in pm
bcc1	$Im\bar{3}m$	339.3
bcc2	$Im\bar{3}m$	337.6
hcp1	P63/mmc	c= 510.4, a=320.2, c/a=1.594

Hardness-depth profile

The experimentally confirmed presence of dissolved oxygen in the subsurface region also affects its hardness. Figure 56 shows the microhardness-depth profile covering the two-phase region comprising matrix and precipitates and the single-phase substrate obtained after two-step oxidation of rolled TiZrNbHfTa. The hardness decreases from approx. 5 GPa near the surface to 4.2 GPa in the single-phase region. Because of the parabolic correlation between oxygen concentration and hardness previously observed in the case of Ti6Al4V (Figure 31, page 39), model equation (11) on page 12 is used to describe the overall decreasing trend. However, the hardness values in the two-phase region scatter in the order of magnitude of 1 GPa. This is due to the hcp1 precipitates having a higher hardness than the bcc2 matrix, as confirmed by comparative hardness measurements indicated in Figure 56 b).

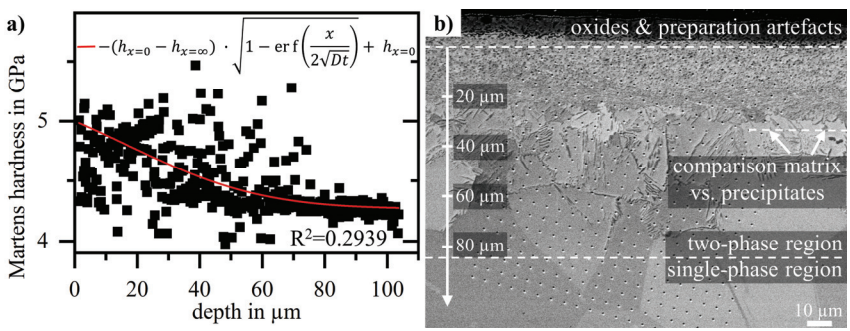

Figure 56: a) microhardness-depth profile covering the two-phase and single-phase region resulting from two-step oxidation of rolled TiZrNbHfTa with a fit according to equation (11) on page 12 and b) the corresponding micrograph. b) additionally indicates the depth used for a comparison between matrix and precipitate hardness, as provided in Table 17.

While the depth profiling yields Martens hardness values of ~4.1 GPa to ~5.2 GPa at a depth of 30 µm, Table 17 lists the Martens hardness values of a separate measurement series explicitly determining the hardness of the precipitates and matrix, as indicated in Figure 56 b). A higher

hardness of the precipitates compared to the matrix is observed. The much higher standard deviation in the case of the precipitates is because the precipitate size is typically smaller than the imprint size of the microhardness measurements. This causes a varying contribution of the matrix hardness to the measured value. All in all, the constant substrate hardness value is not reached until a depth of 80 µm. Compared to the single-step process (Figure 42, page 48), the subsurface region associated with a hardness decrease is more than doubled.

Table 17: Mean and standard deviation derived from nine Martens hardness measurements of the matrix and the precipitates shortly after the transition region from fine, round precipitates to lamellar precipitates, as indicated in Figure 56 b).

	matrix in MPa	**precipitate** in MPa
mean	4571	5114
standard deviation	72	235

5.3 Tribological properties of Ti6Al4V and TiZrNbHfTa after oxidation

The surface properties of the initial state of Ti6Al4V and TiZrNbHfTa are compared to the surface properties resulting from the oxidation processes performed with each material, as described in Table 7 on page 21.

Surface morphology

Oxidation significantly influences the surface morphology, as shown in the SEM images of cross-section micrographs in Figure 57.

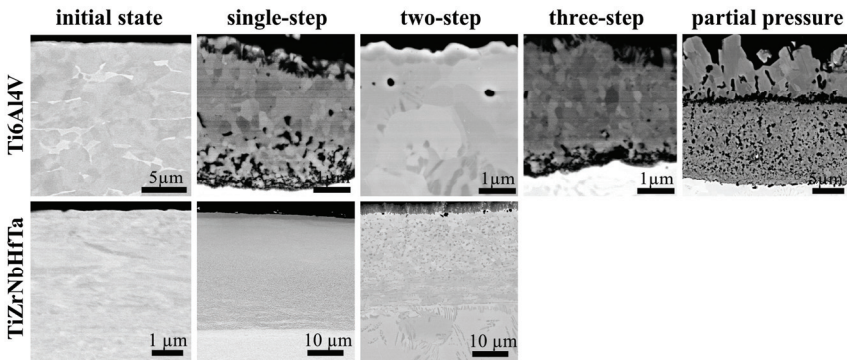

Figure 57: Comparison of the surface morphologies according to BSE-SEM images of cross-section micrographs of Ti6Al4V and TiZrNbHfTa after different oxidation processes.

Single-step and three-step oxidation of Ti6Al4V lead to a porous surface oxide layer with pores allocated at the oxide-metal interface, as previously described (section 5.1, page 31). A mainly pore-free surface without an oxide layer is obtained via the two-step process, while oxidation of Ti6Al4V at reduced oxygen partial pressure causes the formation of needle-shaped oxide

grains on top of an oxide layer with fine, homogeneously distributed pores. These needle-shaped oxide grains are removed by grinding before further tribological experiments. In the case of TiZrNbHfTa, single-step and two-step oxidation both lead to the presence of a micrometer-sized surface oxide layer without any pores, as detailed in section 5.2 (page 40).

Rockwell indentation testing

Figure 58 shows the respective surfaces with the imprints caused by Rockwell indentation testing. In the initial state, the indentation does not cause any crack formation nor spallation. Instead, all oxidation processes affect the specimens in a way that cracking of different extent and/or spallation occurs around the imprint. The adhesion classes according to ISO 26443 derived from the appearance of the imprints, as described in section 4.3.5 (page 27), are given in Table 18.

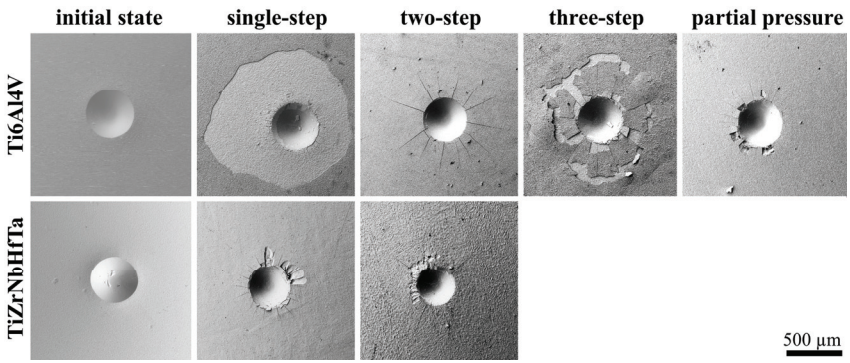

Figure 58: Comparison of the surface layer adhesion, determined via Rockwell indentation testing, of Ti6Al4V and TiZrNbHfTa after different oxidation processes.

Ti6Al4V, after two-step oxidation, has the best adhesion class, yet no surface oxide layer is present in this case. Considering only surfaces with a surface oxide layer, Ti6Al4V oxidized at reduced oxygen partial pressure, and TiZrNbHfTa after single-step and two-step oxidation are best with an adhesion class ranging between class 1 and class 2.

Table 18: Adhesion classes derived from Rockwell indentation tests according to ISO 26443 based on the imprints shown in Figure 58.

process	Ti6Al4V	TiZrNbHfTa
single-step	3	1-2
two-step	1	1-2
three-step	2-3	-
partial pressure	1-2	-

Surface hardness

Figure 59 a) shows the result of Vickers surface hardness measurements (HV0.5) which correspond to indentation depths of up to 3 µm. Ti6Al4V and rolled TiZrNbHfTa in the initial

state have a comparable hardness of ~350 HV0.5. All oxidation processes lead to an increase in surface hardness. The highest hardness in the case of Ti6Al4V is obtained with oxidation at reduced oxygen partial pressure. Single-step oxidation of rolled TiZrNbHfTa leads to the globally highest hardness of 1522 ± 64 HV0.5, while the two-step process in the case of TiZrNbHfTa again reduces the hardness. Figure 59 b) shows Vickers surface hardness measurements (HV0.01), corresponding to indentation depths below 1 µm. The smaller indentation depths and hence smaller imprints are the reason for a larger scattering compared to the HV0.5 measurements since the imprints can be identified less precisely and are more prone to be affected by local obstacles such as pores. Furthermore, the smaller indentation depths can also explain the systematic shift towards higher hardness values. Especially the high hardness values obtained for TiZrNbHfTa after the two-step process compared to the HV0.5 measurement are remarkable. In addition to an indentation size effect, they can be explained by the micrometer-sized compact surface oxide layer still present, which is not protruded due to the smaller load applied during the HV0.01 measurements.

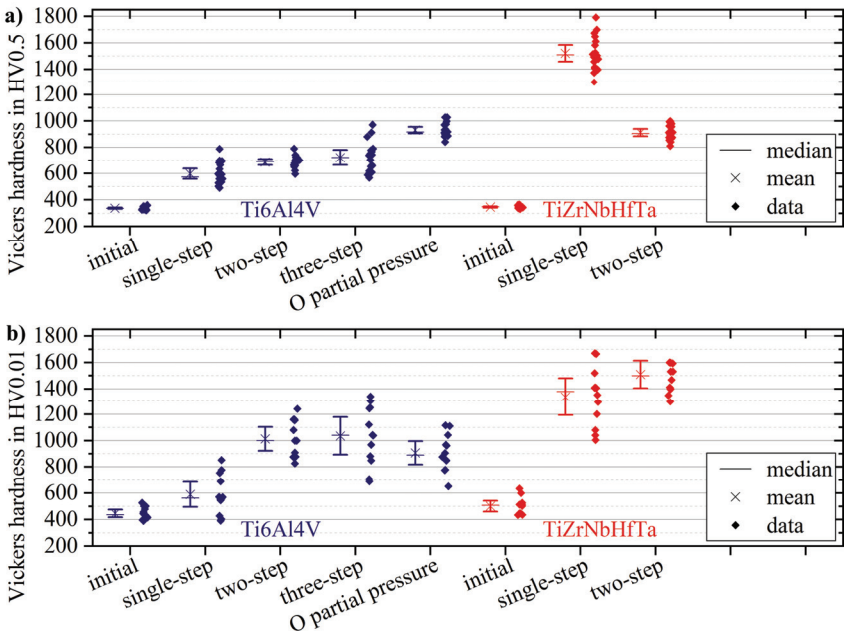

Figure 59: Comparison of a) the Vickers surface hardnesses HV0.5 and b) HV0.01 of Ti6Al4V and TiZrNbHfTa after different oxidation processes. 95% confidence intervals are indicated.

Surface roughness

The result of R_a and R_z surface roughness measurements of Ti6Al4V and TiZrNbHfTa after different oxidation processes are shown in Figure 60. Both roughness parameters reflect a similar trend. The formation of an oxide layer always goes along with a surface roughness

increase. In the case of Ti6Al4V, the reduction of the oxide layer during the two-step process reduces the roughness compared to the previous oxide layer. This is not the case for TiZrNbHfTa, where a compact surface oxide layer with a further increased roughness is still present after the two-step process. The comparable low roughness observed for Ti6Al4V after oxidation at reduced oxygen partial pressure can be explained by the grinding step after oxidation in order to remove the needle-shaped oxide grains.

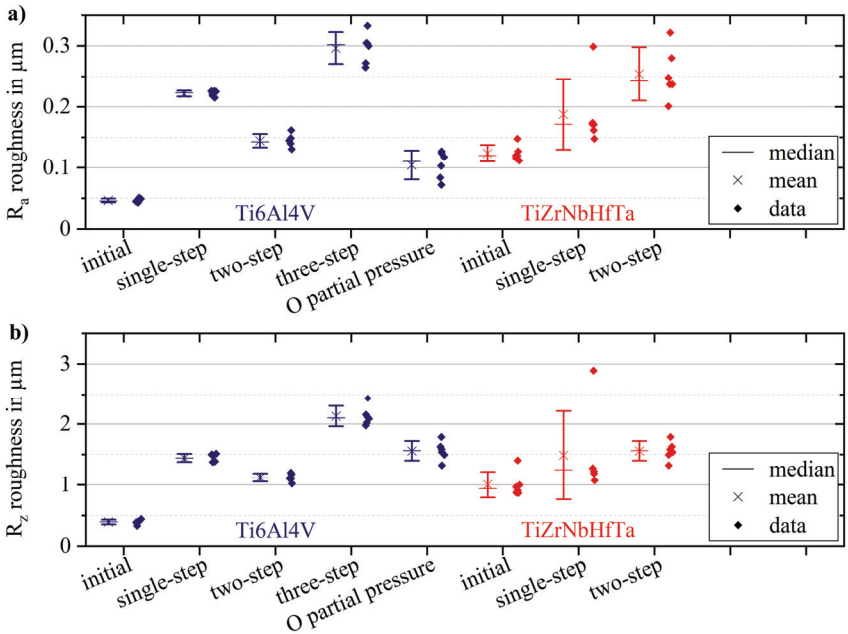

Figure 60: Comparison of a) the surface roughnesses R_a and b) R_z of Ti6Al4V and TiZrNbHfTa after different oxidation processes. 95% confidence intervals are indicated.

Knee joint wear testing

Figure 61 shows the wear traces resulting from knee joint wear testing of Ti6Al4V and TiZrNbHfTa after different oxidation processes. In all cases, wear traces are visible. Defects in the oxide layer formed during single-step and three-step oxidation of Ti6Al4V are apparent (arrows 1 & 2, Figure 61). A defect-free surface is observed for the specimen after two-step oxidation and the specimen oxidized at reduced oxygen partial pressure. The surface of TiZrNbHfTa treated with the single-step process is mainly defect-free except for a larger spalled-off region at the specimen edge (arrow 3, Figure 61), which can be explained by an intrinsic defect of the material. The surface obtained after the two-step process instead is entirely defect-free.

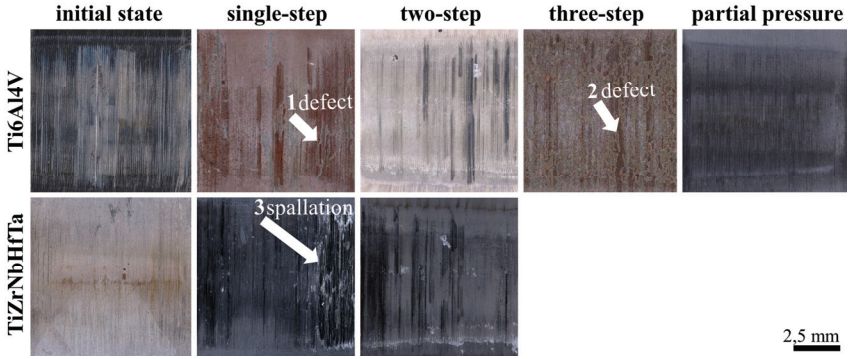

Figure 61: Comparison of the wear traces resulting from knee joint wear testing of Ti6Al4V and TiZrNbHfTa after different oxidation processes. The spots marked with arrows are referenced in the text.

Calo wear testing

A quantitative comparison of the wear behavior in terms of a wear coefficient derived from calo wear tests is given in Figure 62. Untreated Ti6Al4V has the highest wear coefficient. All oxidation processes lead to a reduction of the wear coefficient. The largest reduction in the case of Ti6Al4V is obtained via the two-step process, while oxidation at reduced oxygen partial pressure leads to the best result among the processes resulting in an oxide layer. Oxidation of TiZrNbHfTa does not reduce the wear coefficient compared to the initial state. The wear coefficient of all investigated TiZrNbHfTa specimens is lower than the ones determined for Ti6Al4V.

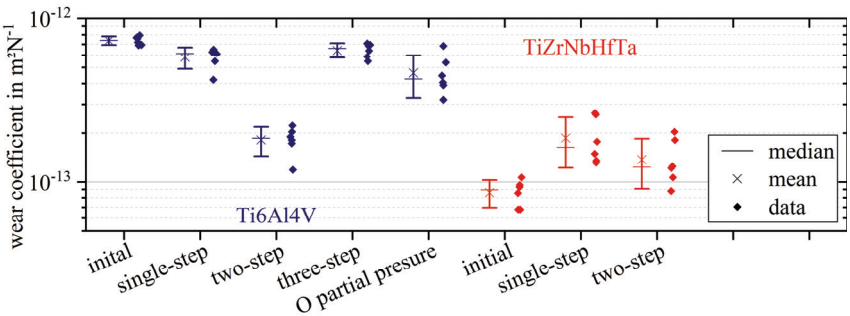

Figure 62: Comparison of the wear coefficients derived from calo wear tests of Ti6Al4V and TiZrNbHfTa after different oxidation processes. 95% confidence intervals are indicated.

Ball on disk tribometer

Figure 63 shows the wear traces resulting from ball-on-disk tribometer wear testing of Ti6Al4V and TiZrNbHfTa after different oxidation processes. The wear traces are distinguishable regarding their width and their homogeneity. Ti6Al4V, in its initial state, exhibits the largest trace width. All oxidation processes reduce the observed wear trace width. In the case of Ti6Al4V, oxidation at reduced oxygen partial pressure leads to the lowest obtained trace width. This wear trace has an inhomogeneous appearance (arrow 1, Figure 63). For TiZrNbHfTa, the largest wear trace is observed after two-step oxidation. Single-step oxidation of TiZrNbHfTa leads to the overall smallest wear trace width.

The wear rate determined from the wear traces reflects a similar trend to the wear trace widths, as shown in Figure 64 a). Ti6Al4V in the initial state has the highest wear rate. Two-step oxidation of Ti6Al4V can slightly reduce the wear rate. The presence of an oxide layer further reduces the wear rate. The single-step and the three-step process lead to identical results. Oxidation at reduced oxygen partial pressure causes the lowest wear rate. The overall lowest wear rate is obtained in the case of TiZrNbHfTa after single-step oxidation, where the wear trace is too narrow to be distinguished from the surrounding with the deployed profilometry method. Two-step oxidation of TiZrNbHfTa does not reduce the wear rate compared to the initial state.

Figure 64 b) provides the coefficients of friction determined during ball-on-disc wear testing. In the case of Ti6Al4V, the presence of an oxide layer after the single-step and three-step process and after oxidation at reduced oxygen partial pressure drastically increase the coefficient of friction compared to the initial state and the two-step process. The coefficient of friction of TiZrNbHfTa remains unaffected by the oxidation processes.

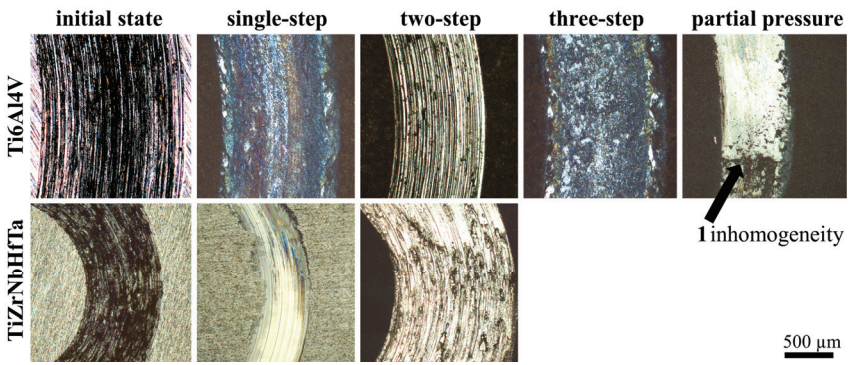

Figure 63: Comparison of the wear traces resulting from ball-on-disk wear testing of Ti6Al4V and TiZrNbHfTa after different oxidation processes. The wear trace images are provided by Beyza Öztürk, DECHEMA-Forschungsinstitut. The spot marked with an arrow is referenced in the text.

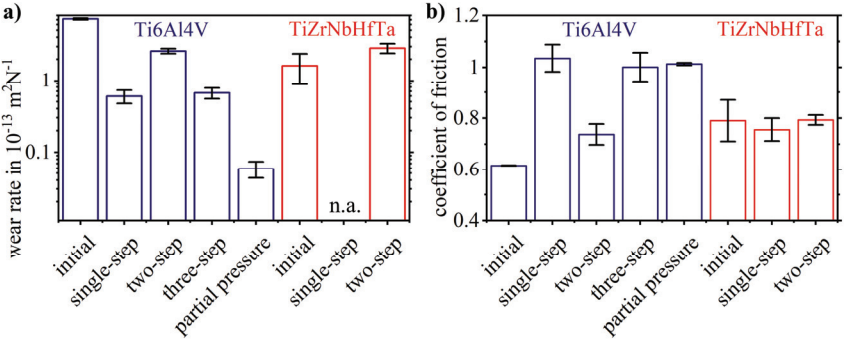

Figure 64: Comparison of a) the wear rates and b) the coefficients of friction of Ti6Al4V and TiZrNbHfTa after different oxidation processes determined via a ball-on-disk tribometer. Standard deviations are indicated. The data are provided by Beyza Öztürk, DECHEMA-Forschungsinstitut.

The results of the comparative study on the effect of different oxidation processes on the surface properties of Ti6Al4V and TiZrNbHfTa are interpreted in the discussion section (section 6.4, page 88).

6 Discussion

6.1 Tailoring surface and subsurface properties of Ti6Al4V via oxidation

6.1.1 Oxidation and diffusion kinetics of Ti6Al4V

The oxidation of Ti6Al4V is well-studied in the literature (section 2.4.3, page 13). This allows setting the oxidation and oxygen diffusion properties of the studied Ti6Al4V specimens in comparison to literature data. In the literature, a reaction kinetics determination based on mass change dominates over an oxide layer thickness analysis. Therefore, Figure 65 compares the reaction constants k_m determined during single-step oxidation screening experiments (Table 8, page 32) to a model developed by Vaché et al. [74]. This model, similar to the present work, considers the mass gain due to oxide layer and oxygen diffusion zone formation. The experimental data are consistent with the model expectation. With 165 kJmol^{-1}, the determined activation energy Q_m is lower than the 232 kJmol^{-1} given by Vaché et al. [74]. This deviation can be explained by the higher oxidation temperatures used in this work and the limited number of data points. In addition, the assumption of parabolic growth is only an approximation as the growth behavior is time and temperature-dependent [82] (section 2.4.3, page 13). This leads to a slight systematic overestimation of the parabolic fit regarding the oxide layer thickness and mass gain at low oxidation durations (Figure 23, page 31).

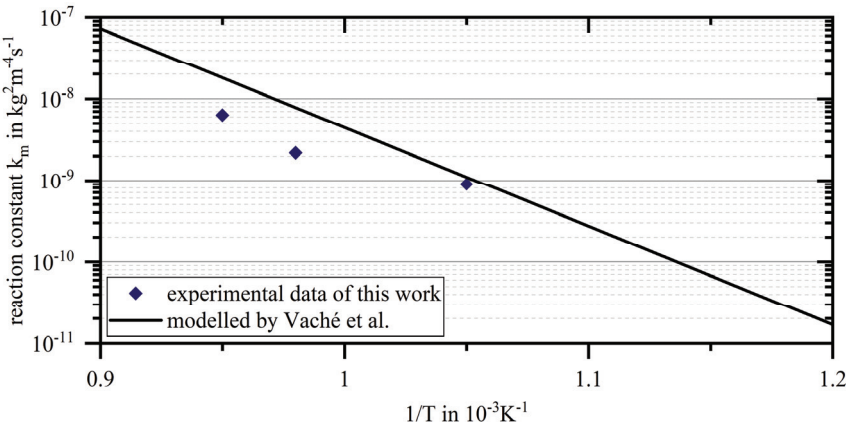

Figure 65: Experimentally determined reaction constants k_m compared to the mass gain model comprising oxide layer and oxygen diffusion zone formation by Vaché et al. [74].

Figure 66 compares the oxygen diffusion coefficients derived from the oxygen concentration-depth and hardness-depth profiles with data available in the literature [74, 81, 86, 127–132]. All three determined oxygen diffusion coefficients (Table 9, page 39) reflect the trend shown in the literature data. The diffusion coefficient determined from the microhardness-depth profile under the assumption of a parabolic oxygen concentration-hardness correlation (equation (11), page 12) best matches the linear regression of all available literature data. However, the

deviation between the determined diffusion coefficients in this work is within a typical range also observed in the literature data. It must be noted that the method applied to determine the oxygen diffusion coefficient affects the outcome due to method-specific systematic errors.

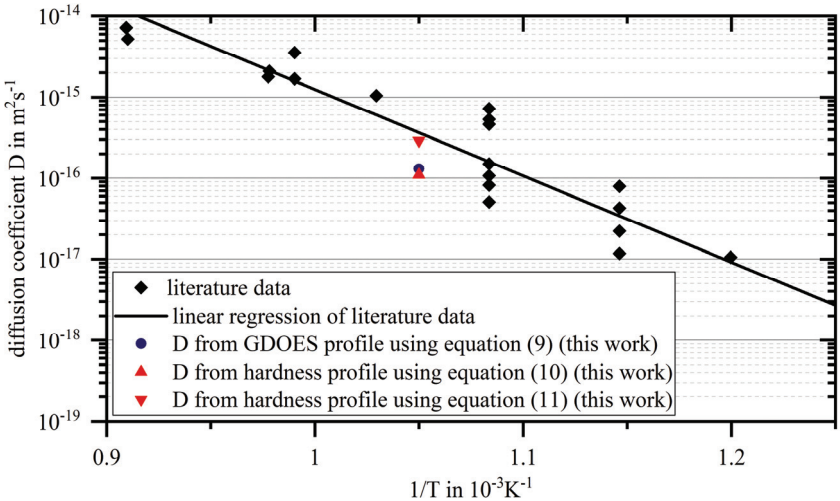

Figure 66: Experimentally determined oxygen diffusion coefficients (Table 9, page 39) compared to data available in Vaché et al. [74] based on other works [81, 86, 127–132].

All in all, the literature data reported on the oxidation and oxygen diffusion behavior of Ti6Al4V are applicable to the specimens studied in this work. Therefore, the following discussion focuses on the specific impacts of the four different oxidation processes on the surface constitution and microstructure (section 6.1.2) and oxygen diffusion zone formation (section 6.1.3).

6.1.2 Process-dependent surface constitution and microstructure

In the present work, information obtained from EDS mappings (Figure 26, page 34), highly magnified SE-SEM images (Figure 25, page 33), and XRD data (Figure 27, page 35) are combined to determine the phases present at the surface grains after the four oxidation processes with a resolution < 1 µm. This is advantageous over the mainly EDS mapping-based analysis performed on oxidized Ti6Al4V specimens available in the literature [93, 100]. Single-step and three-step oxidation of Ti6Al4V lead to the formation of a TiO_2 rutile oxide layer. At the surface, the rutile oxide grains occur either as elongated rods or polyhedrons. α–Al_2O_3 oxide grains are identified in the top 500 nm of the oxide layer but do not entirely cover the oxide layer. This observation agrees with the theory proposed by Du et al. [82], according to which TiO_2 preferably forms at the oxide-substrate interface, as shown in Figure 67. According to the present work, this theory also remains applicable to the additional final oxidation step during the three-step process.

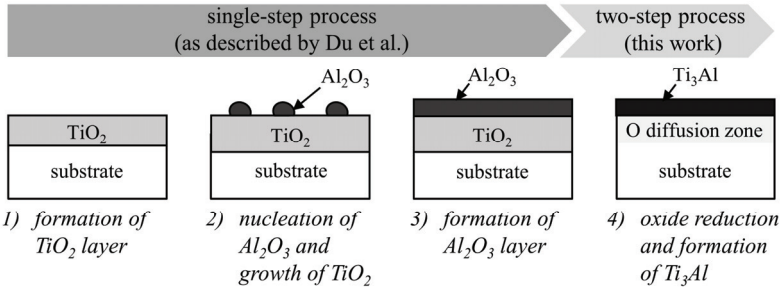

Figure 67: Illustration of the oxide layer formation process during single-step oxidation, as described by Du et al. [82], and the Ti_3Al phase formation at the surface during the two-step process.

The observed formation of nodular oxide grain clusters (Figure 25, page 33) during air oxidation of Ti6Al4V is a common phenomenon [26, 82, 89, 92, 133]. Their occurrence cannot be explained with the approach of Du et al. [82], as done by Zhang et al. [89], who observed an increased Al outward diffusion towards the surface due to bending strains. No indication of such an enhanced Al_2O_3 presence in these clusters is given in this work. Casadebaight et al. [134] report an oxide grain cluster formation due to preferential oxidation of β-phase regions between α-laths. Also, this idea is unlikely applicable to the specimens used in this work since oxide grain clusters are also observed on specimens after the three-step process where the subsurface region is depleted in β-phase. A reliable explanation for the formation of oxide grain clusters would require additional studies explicitly focusing on these clusters, which is beyond the scope of this work.

As expected, the oxide layer is successfully reduced during the two-step process. The grains directly at the surface (Figure 26 b), page 34) are identified as Ti_3Al. While a similar terraced surface morphology was observed for pure Ti [135], no detailed studies of the surface grains after two-step oxidation of Ti6Al4V are available according to the author's knowledge. Nevertheless, the formation of Ti_3Al is plausible. Since Al_2O_3 oxide grains form at the surface during single-step oxidation [82, 89], as previously described, the surface after the oxide layer reduction step is locally enriched in Al. According to the TiAl phase diagram (Figure 2, page 5), this increased Al concentration leads to the formation of the Ti_3Al phase, as illustrated in Figure 67. Ti_3Al can also dissolve high amounts of interstitial oxygen [136]. An oxygen concentration difference between the Ti_3Al surface grains and Ti grains underneath can not be distinguished based on the EDS mapping (Figure 26 b), page 34) or the GDOES measurements (Figure 30, page 38). Therefore, the presence of interstitially dissolved oxygen in the Ti_3Al surface grains after two-step oxidation is possible.

The surface constitution and morphology resulting from oxidation at reduced oxygen partial pressure is as described by Du et al. [102]. A multilayered oxide layer forms, consisting of needle-shaped TiO_2 oxide grains, an intermediate Al_2O_3 layer, and a fine, porous TiO_2 layer.

6.1.3 Tailoring oxygen concentration- and hardness-depth profiles

The direct comparison of four different oxidation processes demonstrates the variety of options available to tailor the oxide layer thickness and morphology, the oxygen concentration-depth profiles, and the corresponding hardness-depth profile (Figure 30, page 38). While single-step oxidation only leads to oxygen diffusion zones of several micrometers, this step defines the amount of oxygen available for the formation of a much larger diffusion zone of up to ~100 µm during oxide layer reduction in the two-step process. The realized parameter set ensures that the oxide layer is completely dissolved and that oxygen diffusion towards the substrate continues even after this point. This explains the lower oxygen concentration at the air-metal interface compared to the effective initial oxygen concentration at the oxide-metal interface in the case of single-step oxidation. Consequently, after the two-step process, the oxygen concentration-depth profile develops a near-linear course compared to a gradual profile shape obtained after single-step oxidation. The additional final oxidation step during the three-step process again only affects the oxygen concentration-depth profile in the first micrometers. In this region, the obtained oxygen concentration-depth profile is a superposition of the near-linear profile created during the two-step process and the gradual profile observed for the single-step process. Figure 68 shows that by adjusting the parameters of each process step in the three-step process, the oxide layer thickness, the overall oxygen-diffusion depth, and the degree of a gradual and near-linear component of the oxygen concentration-depth profile (blue, continuous line, Figure 68) can be tailored. In contrast, oxidation at reduced oxygen partial pressure does not offer this flexibility but has the big advantage of just one oxidation step.

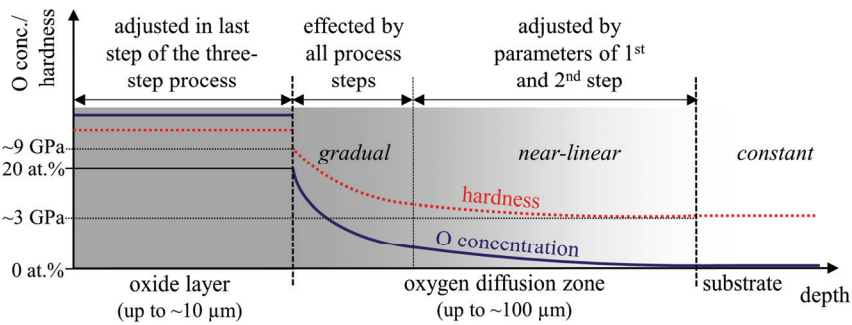

Figure 68: Schematic representation of the influence of the different process steps realized during three-step oxidation on the oxygen concentration-depth profile (blue, continuous line) and hardness-depth profile (red, dotted line).

Due to the correlation between oxygen concentration and hardness, the previous findings not only apply to the oxygen concentration-depth profiles but also to the hardness-depth profiles (red, dotted line, Figure 68). Comparing GDOES data and microhardness measurements confirms that the relationship between oxygen concentration and hardness of Ti6Al4V follows a parabolic law (Figure 31, page 39). This is in line with Vaché et al. [74] and stresses that equation (11) on page 12 is to be used rather than equation (10) on page 12 to derive an oxygen diffusion coefficient based on hardness-depth profiles.

Besides an impact on the hardness in the subsurface region, the formation of an oxygen diffusion zone also influences the microstructure. A decrease in the amount of β-phase in the oxygen diffusion zone occurs, which is also observed by Zhang et al. [25]. It can be explained by the α-stabilizing nature of oxygen [5]. As observed during the two-step process, such a β-phase depleted zone increases with increasing oxygen diffusion depths. Additionally, the accumulation of Al in the surface near region during the two-step process leads to the formation of a lamellar microstructure with α-Ti lamella and α_2-Ti_3Al lamella, as observed by Bagot et al. [137]. Following the β-phase depleted zone, an α- and β-phase transition region is observed, as also described by Zhang et al. [25], until a stable α- and β-phase ratio is obtained. The BSE-SEM images (Figure 28, page 36) show that these microstructural changes are also true for Ti6Al4V oxidized at reduced oxygen partial pressure, which has not been studied before.

6.2 Surface hardening of TiZrNbHfTa through single-step oxidation

6.2.1 Microstructure influence on the prevailing oxidation mechanism

The key difference between the three investigated TiZrNbHfTa material states as-cast, rolled, and rolled & annealed is their initial microstructures, while their elemental composition and crystal structure are comparable. These microstructure differences result from the various manufacturing routes used, i.e., casting on a cooled copper plate, cold rolling, and cold rolling with subsequent annealing. They have a significant impact on the oxidation behavior.

Coarse-grained TiZrNbHfTa

The as-cast and the rolled & annealed specimens both exhibit catastrophic oxidation. This is in line with the observations made by Chang et al. [18] for as-cast TiZrNbHfTa oxidized between 700 °C and 1300 °C and by Sheihk et al. [106] for as-cast $Ti_{1.5}ZrNb_{0.5}Hf_{0.5}Ta_{0.5}$ oxidized between 600 °C and 1000 °C. In their work, Sheihk et al. [106] published a detailed SEM image and an electron backscattered diffraction image of the bulk microstructure revealing grains of approx. 50 µm size (49 ± 29 µm) and the occurrence of subgrain boundaries. Except for a slightly smaller grain size compared to the as-cast material used in this work, the microstructure is similar. Therefore, catastrophic oxidation of TiZrNbHfTa can be linked to the presence of coarse grains with grain sizes of several tens of micrometers. The presence or absence of subgrain boundaries has a negligible effect with regard to the goal of achieving a hard, adherent oxide layer since catastrophic oxidation is observed for as-cast (subgrain boundaries) and rolled & annealed TiZrNbHfTa (no subgrain boundaries). In order to understand the cause-effect relationship between the presence of coarse grains of several tens of micrometers in size and catastrophic oxidation, several phenomena must be considered. According to Schütze [138], four types of stresses can be associated with the failure of an oxide layer:

- intrinsic growth stresses, e.g., due to the chemical nature of the oxidation process
- geometrically induced growth stresses, e.g., at curvatures
- thermal stresses, e.g., due to different thermal expansion coefficients of oxides and metals
- external stresses, e.g., external forces

From a macroscopic perspective, it is not apparent why coarse-grained TiZrNbHfTa exhibits catastrophic oxidation and ultrafine-grained material does not. Under the assumption that the same oxide types form because of identical elemental composition, intrinsic growth stresses, geometrically induced growth stresses, thermal stresses, and external stresses should be comparable. However, differences regarding intrinsic growth stresses can arise from a microscopic viewpoint. Besides a Pilling-Bedworth ratio unequal to one, several aspects contribute to intrinsic growth stresses [138], such as phase and compositional changes [139] or oxygen diffusion into the metal in combination with oxygen dissolution [140].

The latter aspects are of high relevance to understanding the oxidation behavior of coarse-grained TiZrNbHfTa because a localized phase decomposition at the grain boundaries (Figure 36, page 43) and an accelerated oxygen inward diffusion along these grain boundaries (Figure 37, page 44) are experimentally observed for as-cast and rolled & annealed material. Both observations go along with compositional changes at the grain boundaries.

To understand the phenomenon of a localized phase decomposition at the grain boundaries, it is essential to acknowledge that all three deployed manufacturing routes preserve the single-phase bcc1 state at room temperature, which is a meta-stable state according to the TiZrNbHfTa phase diagram (Figure 4, page 6). A phase decomposition of this meta-stable bcc1 phase into a bcc2 and a hcp1 phase during oxidation at 600 °C, or heat treatment in general, is expected according to the phase diagram and previous works [45, 59–61]. The reason for the phase decomposition preferably taking place at the grain boundaries is that these provide fast diffusion pathways and are possible nucleation sites for the bcc2 and hcp1 phases [45]. Figure 69 provides a schematic illustration of such a phase decomposition at the grain boundaries.

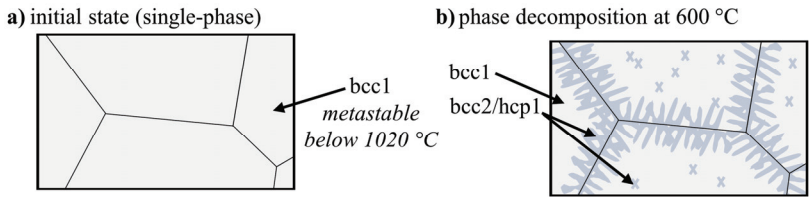

Figure 69: Schematic illustration of a) the coarse-grained single-phase bcc material and b) the phase decomposition at 600 °C taking place preferably at the grain boundaries.

As shown for a face-centered cubic $Co_{26}Cu_{10}Fe_{27}Mn_{10}Ni_{27}$ alloy, a phase formation at grain boundaries may comprise different stages of segregation and depletion of certain elements [141], which are fostered by the possibility of a fast diffusion at the grain boundaries. For TiZrNbHfTa, Schuh et al. [45] assign an observed intercrystalline fracture during tensile testing of nanocrystalline material after 1 h of annealing at 500 °C to the precipitation of a brittle phase at the grain boundaries. More specifically, the weak interface strength between the precipitating hcp-phase and the bcc-phase is claimed to cause the intercrystalline fracture [45]. While such an intercrystalline fracture due to a phase decomposition at grain boundaries is to be considered, the SEM images of substrate regions of as-cast and rolled & annealed TiZrNbHfTa (Figure 36, page 43) do not imply a deterioration of these materials solely due to

a phase decomposition at the grain and subgrain boundaries. Instead, crack formation and spallation are only observed in the oxygen-enriched zone (Figure 35, page 42).

Therefore, accelerated oxygen diffusion along grain boundaries must be considered. The EPMA mapping (Figure 37, page 44) confirms that the grain boundaries act as pathways for inward oxygen diffusion. In contrast to rolled TiZrNbHfTa, the as-cast and the rolled & annealed material possess pronounced grain boundaries oriented perpendicular to the surface, which can promote a rapid in-depth diffusion of oxygen. At the grain boundaries, two effects are possible due to the presence of oxygen. Since oxygen is an α-phase stabilizing element [5], the formation of hcp precipitates is enhanced. These precipitates can then dissolve high amounts of oxygen. Additionally, oxygen at the grain boundaries can lead to intergranular oxidation of the Hf and Zr-rich hcp phases. Regardless of the scenario, either the oxygen dissolution, leading to an increased cell volume of the hcp phase due to an increase of the lattice constants [73], or the oxide formation with the oxides having a Pilling-Bedworth ratio larger than one, will lead to internal stresses [65, 139, 140] and consequently to intergranular cracking [142]. Such an intergranular crack is visible in Figure 40 on page 45. According to Evans [140], the relaxation of stresses caused by oxygen dissolution can also be linked to the fracture of a surface oxide layer. Figure 70 a) illustrates the accelerated oxygen inward diffusion along grain boundaries during the oxidation of coarse-grained TiZrNbHfTa. In addition, the formation of a surface oxide layer and an oxygen-enriched zone, as observed in the EPMA images (Figure 35, page 42), is shown. In Figure 70 b), the formation of intergranular cracks due to internal stresses arising from the localized phase decomposition in combination with the localized ingress of oxygen are visualized, leading to the spallation of the oxide layer.

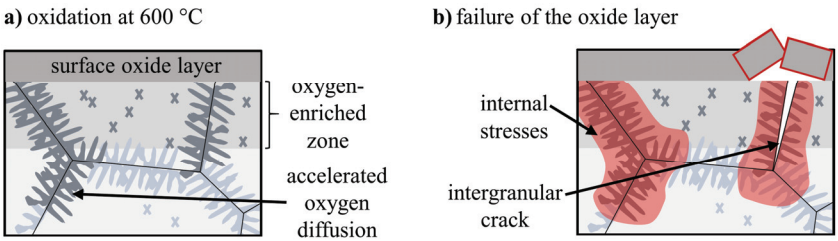

Figure 70: Schematic illustration of a) the accelerated oxygen ingress along the grain boundaries during oxidation of coarse-grained TiZrNbHfTa at 600 °C and b) the resulting localized internal stresses leading to intergranular cracking and failure of the oxide layer.

Alternative explanations for the catastrophic oxidation behavior of coarse-grained TiZrNbHfTa have been set up in the literature. Sheik et al. [106] attribute the pesting behavior of $Ti_{1.5}ZrNb_{0.5}Hf_{0.5}Ta_{0.5}$ mainly to the lack of formation of a protecting scale caused by a mismatch in volume expansion between the formed oxides and the substrate in addition to intergranular oxidation. This can explain the spallation and cracks in the surface oxide layer observed for as-cast and rolled & annealed TiZrNbHfTa (Figure 37, page 44; Figure 40, page 45). Another mechanism set up by Gorr et al. [143] assumes oxygen dissolution and crack formation in the metal as a starting point for catastrophic oxidation. Gorr et al. [143] attribute the local crack

formation to stresses resulting from an anisotropic lattice distortion due to oxygen interstitials. According to Kofstad [65], these oxygen interstitials occupy octahedral sites in the bcc crystal. Both explanations only address the oxidation behavior on a macroscopic level and do not consider the microstructure. This is necessary to distinguish between the behavior of coarse-grained and ultrafine-grained TiZrNbHfTa.

Figure 71 summarizes that despite the presence of macroscopic intrinsic growth stresses, geometrically induced growth stresses, thermal stresses, and external stresses, a localized phase decomposition drives the catastrophic oxidation of coarse-grained TiZrNbHfTa at the grain boundaries in combination with rapid oxygen inward diffusion along the grain boundaries.

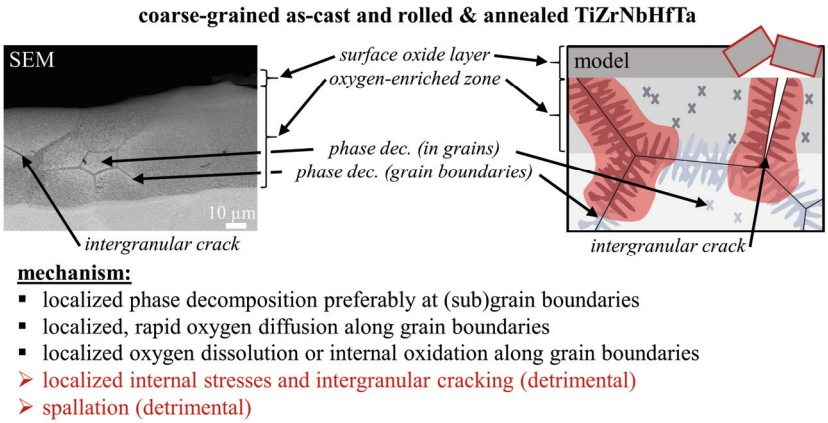

Figure 71: Mechanism explaining the catastrophic oxidation behavior of coarse-grained TiZrNbHfTa.

Ultrafine-grained TiZrNbHfTa

An oxidation mechanism (Figure 72) is developed based on the experimental findings (section 5.2.2, page 41). This mechanism accounts for the ultrafine-grained microstructure of rolled TiZrNbHfTa and can explain its substantially different oxidation behavior compared to coarse-grained as-cast and rolled & annealed material.

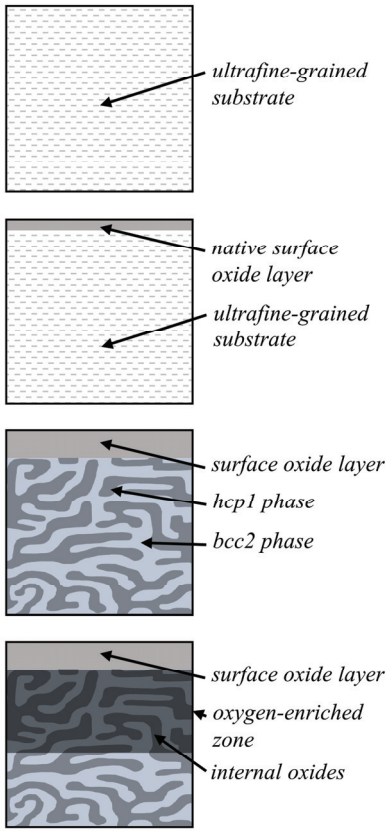

Figure 72: Mechanism describing the single-step oxidation process of rolled, ultrafine-grained TiZrNbHfTa at 600 °C.

The proposed mechanism acknowledges that a native oxide layer forms and grows on TiZrNbHfTa already in air at ambient temperatures (Figure 72 II), as confirmed by the XPS analysis (Figure 45 a), page 50). This is expected to occur independent of the microstructure and therefore is not the reason for the different oxidation behavior of ultrafine-grained material compared to coarse-grained material. However, the capability of TiZrNbHfTa to form such native oxide films is vital with regard to biomedical applications since it allows a so-called self-

healing of the oxide layer upon damage through scratches due to wear. The oxides identified in the native oxide layer are the monometallic oxides TiO_2, ZrO_2, Nb_2O_5, HfO_2, and Ta_2O_5. This is in line with previous XPS studies on TiZrNbHfTa and $Ti_{1.5}ZrNb_{0.5}Hf_{0.5}Ta_{0.5}$ oxidized in air at ambient temperature [64, 103–105]. In two publications [104, 105], minor additional monometallic oxides and suboxides, not identified in this work, are reported. The ratio of detected elements in oxidized state to elements in metallic state increases over time for all elements, while especially Ti, Zr, and Hf rapidly oxidize (Figure 45 a) and b), page 50). According to the Ellingham-Richardson diagram (Figure 5, page 8), ZrO_2, followed by HfO_2 and TiO_2, are more stable oxides than Nb_2O_5 and Ta_2O_5 and have a higher oxygen affinity which explains their preferential occurrence. Hruska et al. [105] also observe such preferential oxidation of Zr, Hf, and Ti in TiZrNbHfTa. This is in agreement with thermodynamic calculations and experiments by Backman et al. [144, 145], who emphasize the preferential oxidation of the group IV elements Zr, Hf, and Ti in high entropy alloys. The referenced XPS studies on TiZrNbHfTa oxidized in air at ambient temperature cover as-cast material [103, 104] and sputtered films [64, 105] with microstructures different from the rolled material studied in this work. This implies that the formation of a native oxide film on TiZrNbHfTa high entropy alloy is an intrinsic material behavior not affected by the microstructure.

During early-stage oxidation at 600 °C, the native oxide layer film grows to form a surface oxide layer (Figure 72 III). Oxygen inward diffusion dominates this process since the gold layer sputtered on a specimen before oxidation remains at the surface even after the oxidation process (Figure 41, page 46). This means that no outward growth of the oxide layer occurs. All elements in the surface oxide layer are present in oxidized state according to the XPS analysis (Figure 45 c), page 50). Therefore, it consists of the monometallic oxides TiO_2, ZrO_2, Nb_2O_5, HfO_2, and Ta_2O_5 only. Oxide powders resulting from oxidation in air at 800 °C studied in the literature show a similar result [11]. The absence of elements in metallic state in the surface oxide layer can be attributed to two factors: Firstly, according to equation (3) on page 8, the oxide dissociation pressure decreases with increasing temperature, meaning that the stability of the oxides increases. This makes even less stable oxides such as Nb_2O_5 and Ta_2O_5 more likely to form. Secondly, as implied by equation (5) on page 9 and equation (8) on page 10, the reaction and diffusion kinetics accelerate with increasing temperature.

Underneath the surface oxide layer, early-stage oxidation causes a phase decomposition of the initial single-phase bcc1 TiZrNbHfTa into a new bcc2 and an hcp1 phase (Figure 72 III), as confirmed by the XRD analysis of rolled material after thermal treatment at 600 °C (Figure 36 d), page 43). This is in accordance with the TiZrNbHfTa phase diagram (Figure 4, page 6) and previous theoretical and experimental works [45, 59–61] underlining that a Nb- and Ta-rich bcc2 and a Hf- and Zr-rich hcp1 phase form instead of the initial meta-stable bcc1 phase. The striking difference between rolled material and as-cast and rolled & annealed TiZrNbHfTa is that the phase decomposition is completed within a few hours. This is due to the ultrafine-grained microstructure providing a vast number of grain boundaries that act as diffusion pathways and as preferred sites for the formation of new phases [45]. In consequence, a homogeneous two-phase microstructure (Figure 36 b), page 43), still on a nanometer scale, develops during early-stage oxidation of rolled TiZrNbHfTa.

Continued oxidation at 600 °C causes oxygen to diffuse through the surface oxide layer towards the substrate (Figure 72 IV). An oxygen-enriched zone forms. BSE-SEM images (Figure 35 b), page 42), as well as the EPMA oxygen mapping (Figure 35 e), page 42), indicate that the oxygen ingress takes place evenly over the whole surface area. No preferred oxygen diffusion pathways are identifiable on a micrometer scale. This is in contrast to as-cast and rolled & annealed material where grain boundaries foster localized oxygen ingress. According to the XPS analysis performed in the oxygen-enriched zone, only Hf and Zr are dominantly present in oxidized state. This is plausible given the previously discussed preferential oxidation behavior of Hf and Zr in high entropy alloys [144, 145]. Preferential oxidation of Hf and Zr fits the observation that the former hcp1 phase, containing high amounts of Hf and Zr, appears significantly darker in the BSE-SEM image (Figure 38, page 44) because it is oxygen-rich. A detailed discussion about the oxygen concentration in the oxygen-enriched zone is provided in the next section 6.2.2.

Figure 73 summarizes why single-step oxidation of ultrafine-grained TiZrNbHfTa results in an adherent oxide layer without catastrophic oxidation.

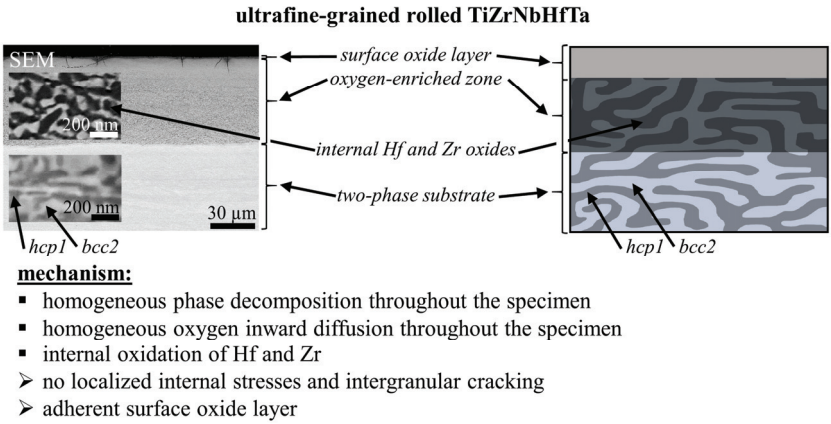

Figure 73: Summary of the mechanism explaining the absence of catastrophic oxidation behavior during single-step oxidation of ultrafine-grained rolled TiZrNbHfTa.

6.2.2 Oxygen-enrichment of rolled TiZrNbHfTa and its implication on hardness

Composition of the surface oxide layer and the subsurface region

Various analysis methods to resolve the elemental composition and oxygen concentration at the surface and in the subsurface region after single-step oxidation and their results have been presented (section 4.3.3, page 22, and section 5.2.2, page 41). While the XPS analysis of the surface indicates the formation of monometallic oxides in agreement with the literature, the surface XRD analysis (Figure 43, page 48) does not unambiguously indicate the presence of such oxides. Figure 74 gives a magnified cutout of the X-ray diffractogram obtained for rolled TiZrNbHfTa oxidized for 24 h at 600 °C. The reflex positions of tetragonal TiO_2 (ICDD 00-

021-1276), monoclinic ZrO_2 (ICDD 04-015-6852), and monoclinic HfO_2 (ICDD 00-034-0104) at ambient conditions are plotted additionally. Despite these oxides being the most likely ones, the match between the experimentally obtained diffractogram and the theoretical reflex positions is poor. According to the database, a peak is matched only for the major HfO_2 reflex. Minor HfO_2 reflexes are only poorly reflected in the diffractogram. Complex oxides such as $HfTiO_4$ or $ZrTiO_4$ [106] or numerous other theoretically possible oxides observed in comparable compositionally complex alloys [145, 146] are neither indicated by the diffractogram. They are typically expected to occur only after prolonged oxidation durations [143] or at higher oxidation temperatures [146]. The fact that only a few, very broad peaks with a poor peak-to-background ratio are observed implies that the analyzed material volume lacks a long-range crystalline order and instead is vitreous. A vitreous oxide layer with local oxide clusters in an overall disorder oxide matrix forming during oxidation at 400 °C has been reported for the high entropy alloy $Fe_{0.28}Co_{0.21}Ni_{0.20}Cu_{0.08}Pt_{0.23}$ [147]. The occurrence of a vitreous oxide layer, therefore, is plausible.

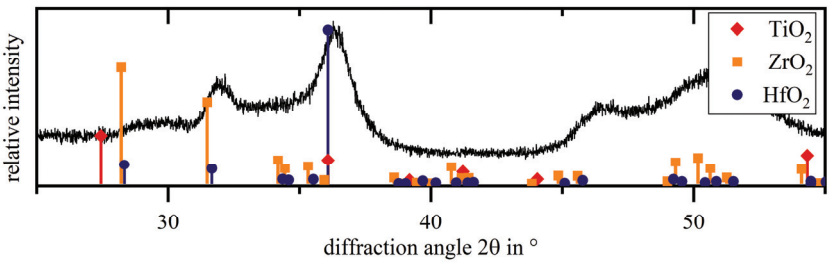

Figure 74: Excerpt of the surface X-ray diffractogram of rolled TiZrNbHfTa after oxidation for 24 h at 600 °C as shown in Figure 43 on page 48 with markers indicating potential reflexes of TiO_2 (ICDD 00-021-1276), ZrO_2 (ICDD 04-015-6852), and HfO_2 (ICDD 00-034-0104).

Amongst the three analysis methods, XPS, EDS, and NRA, yielding information about the oxygen concentration at the surface and in the subsurface region, NRA is outstanding because it provides the complete oxygen concentration-depth profile. In Table 19, the NRA oxygen concentrations (Figure 42, page 48) are listed next to the oxygen concentrations implied by the presence of certain oxides according to the XPS analysis (Figure 45, page 50) and the oxygen concentrations measured via EDS (Figure 41, page 46). The core assumption allowing this comparison is that if the material is homogeneous, the oxygen concentration determined via NRA can be expressed as oxygen stoichiometry x in $Ti_1Zr_1Nb_1Hf_1Ta_1O_x$. This is not the case due to the formation of a Hf- and Zr-rich hcp1 and a Nb- and Ta-rich bcc2 phase on a nanometer scale. Given the NRA beam size of 4.5 µm x 3.5 µm and a pixel size of 2 µm x 2 µm, an XPS spot size of up to 100 µm, and an evaluated EDS mapping region of 4 µm x 0.5 µm (Figure 41, page 46), the assumption of a homogenous material regarding the oxygen concentration analysis is still appropriate. Averaging information from an EDS mapping region of 4 µm x 0.5 µm, leading to an analyzed volume of ~2 µm³, the EDS results shown in Table 12 on page 47 confirm an equimolar presence of the metallic elements.

Table 19: Expected oxygen concentrations of the surface oxide layer and the oxygen-enriched zone (in oxygen stoichiometry x and in at.%) according to the oxides indicated by the XPS analysis compared to the NRA and EDS measurements.

	oxides indicated by XPS	**c(O) implied** in stoich. x	**c(O) implied** in at.%	**c(O) NRA** in stoich. x	**c(O) NRA** in at.%	**c(O) EDS** in at.%
surface oxide layer (cross-section)	TiO_2 ZrO_2 Nb_2O_5 HfO_2 Ta_2O_5	11	69	7.5	60	67
oxygen-enriched zone at 30 µm (cross-section)	ZrO_2 HfO_2	4	44	3.5	41	-
surface oxide layer (surface)	TiO_2 ZrO_2 Nb_2O_5 HfO_2 Ta_2O_5	11	69	11	69	67

As depicted in Table 19, the expected oxygen stoichiometry in a surface oxide layer solely consisting of monometallic oxides would be 11, which is equivalent to an oxygen concentration of 69 at.%. According to the cross-sectional NRA mapping, the measured oxygen stoichiometry is only 7.5 at the surface. This can be explained by the presence of elements in metallic state in regions of the surface oxide layer not reached by the surface XPS analysis or by a lack of resolution of the NRA mapping. Figure 75 shows the capability of the different analysis methods to locally resolve the elemental composition of the surface oxide layer. It is apparent that a lack of resolution during the NRA mapping is the cause for the mismatch between the expected and determined oxygen stoichiometry. In contrast, the NRA surface spot measurement yields an oxygen stoichiometry of 11, which agrees with the EDS analysis. A comparable resolution problem does not occur in the oxygen-enriched zone, where less sharp concentration changes are expected.

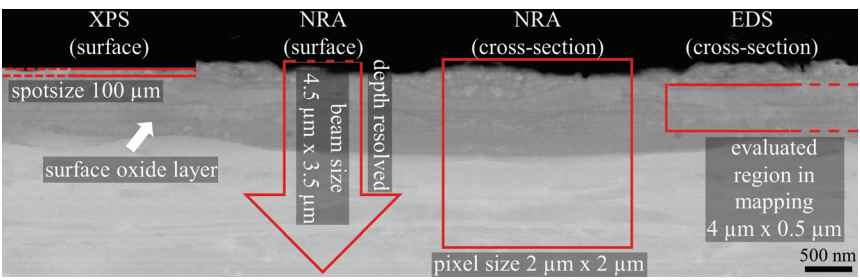

Figure 75: Schematic representation of the capability of the methods XPS (surface), NRA (surface), NRA (cross-section), and EDS (cross-section) to resolve the elemental composition of a surface oxide layer obtained during single-step oxidation of rolled TiZrNbHfTa.

At 30 µm depth from the surface, the NRA mapping again yields a slightly lower oxygen stoichiometry than expected. This is due to the presence of minor amounts of Zr and Hf still in metallic state. However, with a minimum oxygen concentration of 41 at.% before the significant decrease after a depth of 30 µm, the oxygen concentration is above the oxygen solubility limit of Ti, Zr, or Hf. This proves the presence of internal oxides, as indicated by the XPS analysis. The data set is therefore consistent and in agreement with the oxidation mechanism discussed earlier in section 6.2.1 (page 70).

Correlation of oxygen concentration and hardness in the oxygen-enriched zone

Similar to Ti6Al4V, a correlation between the oxygen concentration-depth profile with the hardness-depth profile is apparent (Figure 42, page 48). As shown in Figure 76 a), one can distinguish two regions in the oxygen-enriched zone: A region of near-linear oxygen concentration and hardness decrease and a region showing a steep, gradual drop in oxygen concentration and hardness. The region of near-linear decrease is characterized by the presence of internal oxides, while the gradual decrease is related to oxygen being interstitially dissolved in the metal. Figure 76 b) shows the correlation between oxygen concentration and hardness, assuming a linear correlation. Figure 76 c) assumes a parabolic correlation. In both cases, two clusters can be identified corresponding to the region with internal oxides and to the region with dissolved oxygen only. Fitting a linear (Figure 76 b)) and a parabolic (Figure 76 c)) correlation model to the data in the region with dissolved oxygen yields a better goodness of fit in the case of a linear model. Due to the small number of data points available for fitting, a parabolic correlation relationship, as found by Vaché et al. for Ti6Al4V [74] and confirmed in this work (Figure 31, page 39), is still not excluded.

Regardless of the correlation model, the model cannot be extended to data points corresponding to the region of internal oxides. The formation of oxides causes a disproportional hardness increase compared to dissolved oxygen. Therefore, the approximated correlation between oxygen concentration and hardness is a pseudo-correlation. A better approach would be to correlate the ratio of oxidized elements to elements in metallic state, which is only implicitly represented in the measured NRA oxygen concentration-depth profile. The precise, depth-resolved ratio of elements in oxidized to elements in metallic state cannot be retrieved from the cross-section XPS analysis (Figure 45 d), page 50) since the measurement provides averaged information over the whole oxygen-enriched zone. It can be assumed that the minor amounts of Zr and Hf atoms still in metallic state are likely located towards depths of 30 µm while, at the surface, all Zr and Hf atoms are in oxidized state. With the decreasing relative amount of elements in oxidized state also the hardness decreases, which is what the hardness-depth profile confirms. It has to be noted that besides the hardening due to the formation of an oxygen-enriched zone with internal oxides or dissolved oxygen, the substrate hardness is also increased compared to the initial rolled material. This is because the phase decomposition as such already leads to a hardness increase according to Stepanov et al. [148].

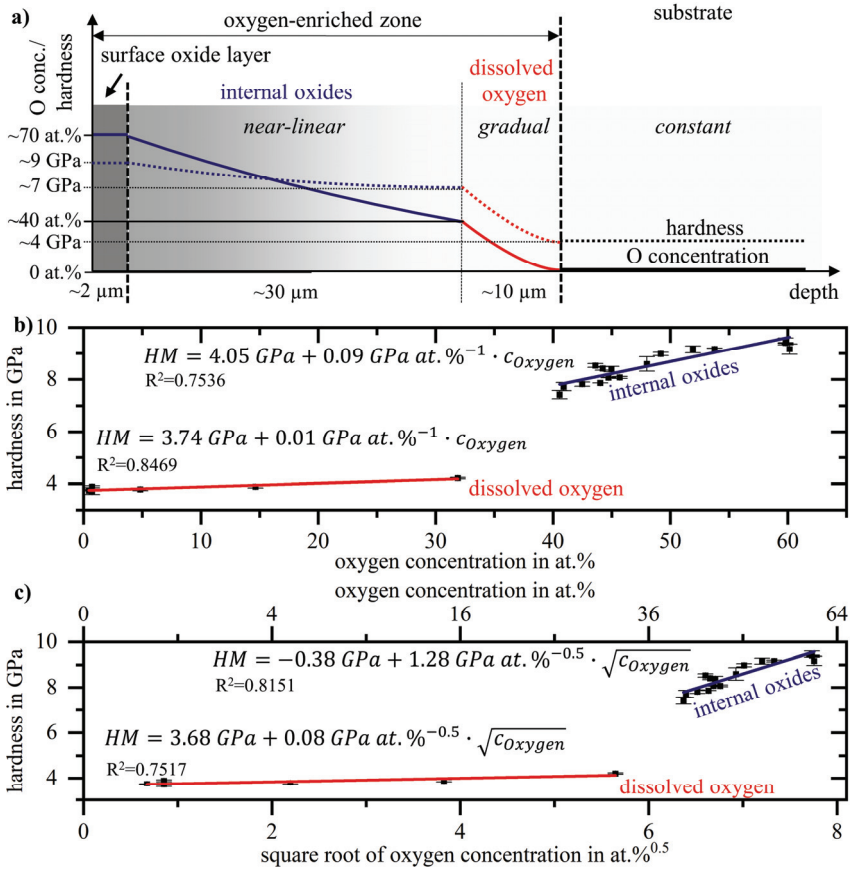

Figure 76: a) schematic oxygen concentration-depth profile (continuous line) and hardness-depth profile (dotted line) obtained after single-step oxidation of rolled TiZrNbHfTa based on NRA measurements (Figure 42, page 48) and correlation of Martens hardness (HM) and oxygen concentration assuming a b) linear and c) parabolic relationship. A different correlation relationship depending on the presence of internal oxides is indicated in b) and c).

6.3 Precipitation hardening of TiZrNbHfTa during two-step oxidation

6.3.1 (Sub-)surface constitution and microstructure due to oxygen presence

The parameters deployed for the vacuum heat treatment step during the two-step process are identical to the ones used for the annealing of rolled TiZrNbHfTa in order to obtain rolled & annealed material. Despite this fact, the resulting microstructures are significantly different. This is due to the formation of a surface oxide layer and an oxygen-enriched zone during single-step oxidation of rolled TiZrNbHfTa previous to the vacuum heat treatment

leading to the presence of oxygen in the subsurface region. The implications of this oxygen presence in the subsurface region are discussed in the following.

Persistence of a surface oxide layer

The micrometer-sized, compact surface oxide layer formed during single-step oxidation in air is still present after the two-step process according to the BSE-SEM images (Figure 47, page 52) and the EDS elemental mapping of the surface region (Figure 49, page 53). Instead of dissolving, the former vitreous surface oxide layer transforms into an oxide layer with distinguishable, recrystallized grains (Figure 48, page 53). The fact that the surface oxide layer is still present is unexpected since the chosen temperature for the vacuum heat treatment with 1200 °C is much higher than the 850 °C typically used for Ti6Al4V [80]. With the oxide layer reduction being a diffusion-controlled process, according to equation (8) on page 10, one would expect a drastically accelerated oxide layer reduction at 1200 °C. In the case of ZrNb7, an oxide layer of several micrometers could be reduced within minutes at 1000 °C [78]. Even though HfO_2, ZrO_2, and TiO_2 are thermodynamically very stable oxides, an oxide layer reduction is possible. It is typically associated with the formation of a pronounced oxygen diffusion zone in which the respective hcp α-phase occurs dominantly or exclusively (Figure 28, page 36) [25, 78] and dissolves high amounts of oxygen [13, 15].

This is in contrast to TiZrNbHfTa. The TiZrNbHfTa phase diagram (Figure 4, page 6) outlines that pure TiZrNbHfTa at 1200 °C is single phase bcc and hence does not possess the capability to dissolve large amounts of oxygen. Additionally, the oxygen-enriched zone formed during single-step oxidation contains internal oxides until a depth of ~30 µm (Figure 42, page 48), leading to an average oxygen concentration in the subsurface region of more than 41 at.% at the start point of the vacuum heat treatment. This oxygen concentration is beyond the solubility limit even of hcp Ti, Zr, and Hf [13, 15, 16]. Consequently, the oxygen-enriched zone created during the single-step process itself acts as an oxygen reservoir for inward oxygen diffusion, which must be consumed first. Until this is the case, the oxygen flux from the surface oxide layer into the metal is low according to equation (7) on page 10. This is because of a low oxygen concentration difference at the interface between the surface oxide layer and the oxygen-enriched zone. Therefore, the surface oxide layer remains present under the selected process conditions of the two-step process.

Precipitate formation in the subsurface region

Underneath the surface oxide layer, the oxygen in the subsurface region is completely dissolved after two-step oxidation. Internal oxides formed during oxidation in air are reduced, as confirmed by the XPS measurements (Figure 54, page 57). The oxygen present in the subsurface region during vacuum heat treatment at 1200 °C leads to the characteristic microstructure observed in BSE-SEM images (Figure 47, page 52) and the EDS analysis (Figure 49, page 53; Figure 51, page 54). Figure 77 illustrates this microstructure compared to the one obtained after the single-step process.

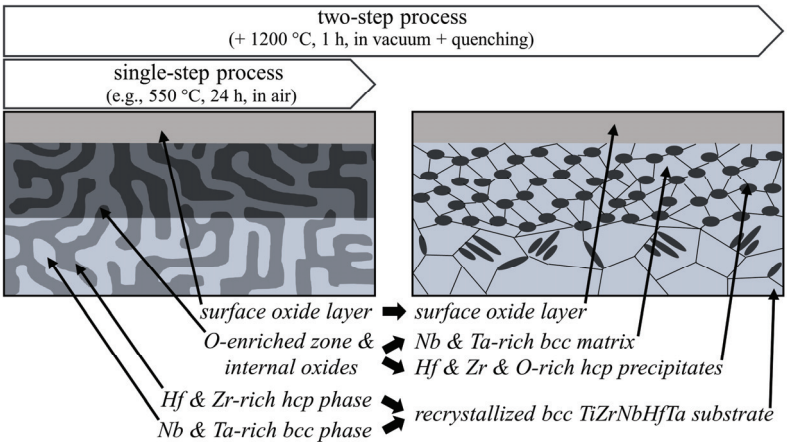

Figure 77: Illustration of the microstructure evolution during two-step oxidation of rolled TiZrNbHfTa showing that: the surface oxide layer obtained during single-step oxidation remains present, the oxygen in the oxygen-enriched zone after single-step oxidation leads to the formation of O-rich hcp precipitates in a bcc matrix, and the substrate recrystallizes single-phase bcc.

In the subsurface region, Hf- and Zr-rich precipitates containing minor amounts of Ti and 20 at.% of oxygen form in an Nb- and Ta-rich matrix, see EDS (Figure 49, page 53; Figure 51, page 54; Table 14, page 55) and APT measurements (Figure 52, page 55; Table 15, page 56). The APT concentration line profiles perpendicularly crossing the interface between a precipitate and the matrix (Figure 53, page 56) reveal that the precipitate is completely depleted in Nb and Ta. In contrast, a higher concentration of Nb and Ta compared to the matrix is observed close to the interface. This indicates that Nb and Ta actively diffuse out of the precipitates. Similar concentration profiles of a bcc2/hcp1 phase interface are reported by Chen et al. [60] in non-oxygen-enriched rolled & annealed TiZrNbHfTa after vacuum heat treatment at 700 °C. Diffusion of Nb and Ta out of the hcp precipitates into a bcc matrix phase is therefore not linked to oxygen presence and can be explained by the β-phase stabilizing nature of Nb and Ta [5]. However, the occurrence of Hf- and Zr-rich precipitates in the subsurface region is attributed to the presence of oxygen because, after a transition region with lamellar-shaped precipitates, the microstructure is single-phase (Figure 47, page 52) like the one observed for rolled & annealed TiZrNbHfTa (Figure 33 c), page 41). In accordance with the TiZrNbHfTa phase diagram (Figure 4, page 6), oxygen-free TiZrNbHfTa is in a single-phase state at 1200 °C.

As introduced in section 2.2.1 (page 3), oxygen is an α-phase stabilizer [5]. It stabilizes the formation of an hcp phase which can dissolve high amounts of oxygen. The XRD analysis (Figure 55, page 57; Table 16, page 58) confirms the presence of an hcp1 phase in the subsurface region after two-step oxidation of TiZrNbHfTa. An oxygen concentration of 20 at.% determined in this hcp1 precipitates is plausible since it is below the oxygen solubility limit of

hcp Ti, Zr, and Hf [13, 15, 16]. An oxygen concentration of up to 3 at.% in the Nb- and Ta-rich matrix (Table 15, page 56), which is bcc according to the XRD analysis (Figure 55, page 57; Table 16, page 58), is in agreement with the oxygen solubility limit of bcc Nb and Ta being 4 at.% at 1200 °C [75–77]. It can be concluded that the presence of oxygen in TiZrNbHfTa suppresses the formation of a single-phase bcc1 phase at 1200 °C. Figure 78 shows a calculated phase diagram (Thermo-Calc, TC-Ni8 database) of TiZrNbHfTa containing 10 at.% oxygen. The phase diagram matches the experimental observation that oxygen suppresses a single-phase bcc1 state. In addition, the experimental observation is consistent with the work of Wu et al. [149], who report the formation of Hf- and Zr-rich hcp precipitates in a bcc matrix in oxygen-doped quaternary TiZrNbHf. The addition of Ta appears not to alter this behavior.

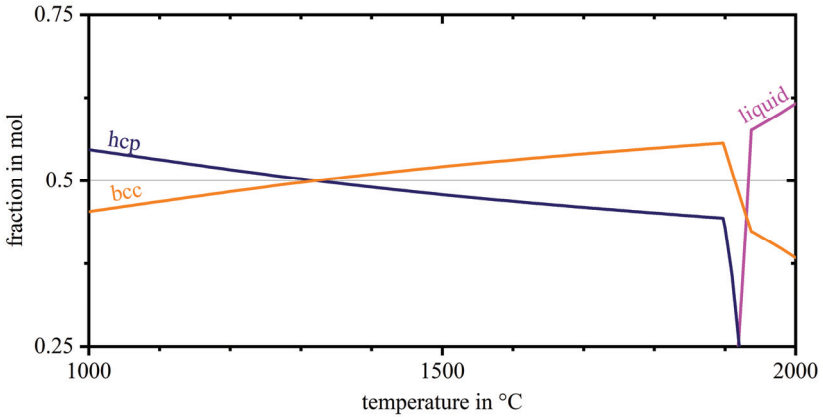

Figure 78: Phase diagram of TiZrNbHfTa containing 10 at.% oxygen as predicted by Thermo-Calc (TC-Ni8 database).

6.3.2 Effect of oxygen diffusion zone formation on hardness and lattice parameters

Oxygen concentration- and hardness-depth profiles in the oxygen diffusion zone

The nature of the hardness-depth profile in the subsurface region obtained via two-step oxidation (Figure 56, page 58) significantly differs from the previously discussed ones (section 6.1.3, page 69; section 6.2.2, page 76). This is because of the two-phase nature of the subsurface region. Other than after single-step oxidation of TiZrNbHfTa, where two phases are only distinguishable on a nanometer scale, precipitates of several micrometers occur. At equal depth, the Hf- and Zr-rich hcp1 precipitates possess a significantly different oxygen concentration and microhardness than the Nb- and Ta-rich bcc2 matrix (Table 15, page 56; Table 17, page 59). This is reflected in a discontinuous oxygen concentration-depth profile on a micrometer scale (Figure 50, page 54). Analogously, the hardness values scatter in the oxygen diffusion zone (Figure 56, page 58). A trend following a hardness decrease according to equation (11) on page 12 can be identified. However, even at up to 80 µm depth, some measurement points lead to hardness values similar to the ones at 0 µm depth. This implies that

a separate oxygen concentration- and hardness-depth profile applies for each phase, as visualized in Figure 79. Identifying the individual profiles would require additional APT measurements of the matrix and precipitates along the depth axis and nano hardness measurements to resolve the hardness of the matrix and the precipitates. Figure 79 also points out that the transition depth from the bcc2 phase to the bcc1 phase may not be congruent with the depth until which the hcp1 phase occurs since the two bcc phases are not distinguishable in the BSE-SEM images (Figure 47, page 52).

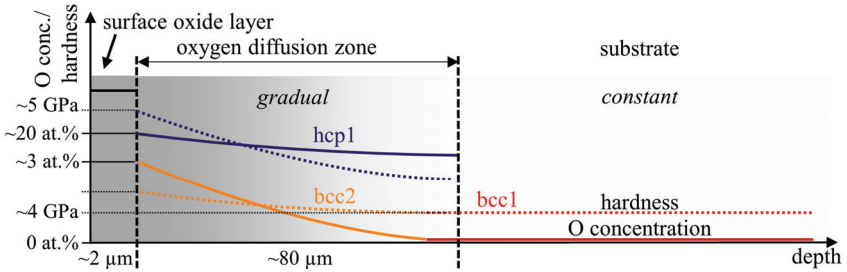

Figure 79: Schematic oxygen concentration-depth profile (continuous line) and hardness-depth profile (dotted line) obtained after two-step oxidation of rolled TiZrNbHfTa showing idealized profiles in the two-phase subsurface region.

Lattice constant increase due to interstitial oxygen

The X-ray diffractogram of the subsurface region, meaning that the surface oxide layer is removed before the measurement (Figure 55, page 57), has an angle-dependent information depth << 10 µm. Therefore, The diffractogram is a superposition of information originating from unit cells located at different depths. According to Figure 79, this means that bcc1, bcc2, and hcp1 unit cells containing different amounts of oxygen are covered. This is a possible reason for the poor refinement model achieved based on these three phases. For titanium and titanium alloys, it is known that dissolved oxygen, which in the case of the α-phase preferentially occurs at octahedral sites [150], leads to a peak shift due to an increase of the lattice constants [73, 151–153]. An increase in the lattice constants due to oxygen dissolution is also observed for bcc TiZrNbHf [154]. This explains the asymmetric peak tails at the lower-angle side observed for both, hcp and bcc peaks. Figure 80 shows the result of an extended refinement considering an additional oxygen-rich bcc(O) and hcp(O) phase beside the already identified bcc1, bcc2, and hcp1 phases to model the asymmetric peak tails.

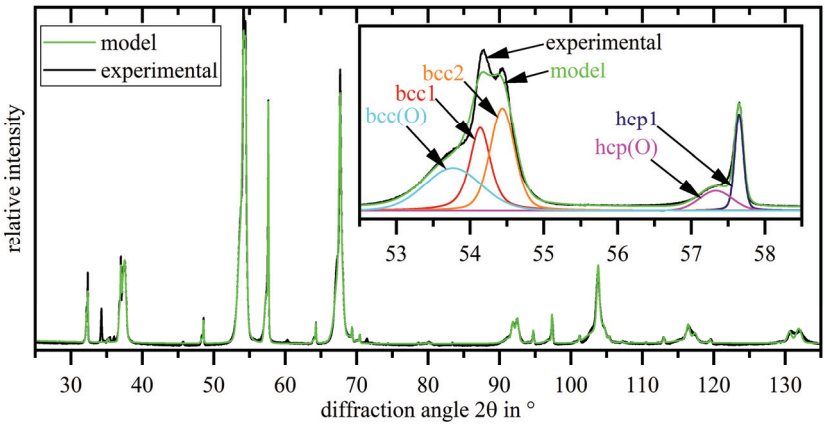

Figure 80: X-ray diffractogram of the subsurface region of rolled TiZrNbHfTa after two-step oxidation and removal of the surface oxide layer, as presented in Figure 55 on page 57. An additional oxygen-rich bcc(O) and hcp(O) phase are considered for the refinement model.

The lattice parameters corresponding to the extended refinement model are given in Table 20 and set in comparison to the ones previously determined for TiZrNbHfTa in the initial state and after single-step oxidation as well as literature values. The lattice parameters of the bcc1 phase are consistent with experimental and literature values for single-phase bcc TiZrNbHfTa. The lattice parameters of the bcc2 phase are larger than the ones determined after the single-step process and reported in the literature. This can be due to an overall different elemental composition of the bcc2 phase after two-step oxidation. The bcc(O) phase to model the asymmetric peak tail has a significantly increased lattice constant compared to the bcc2 phase due to the interstitially dissolved oxygen. Nevertheless, the lattice parameters of the bcc(O) phase are distinguishable from a bcc3 phase reported to occur at 700 °C [60] and 800 °C [45] (Table 20). The lattice parameters obtained for the hcp1 phase after two-step oxidation are increased compared to the single-step process. This is due to a different elemental composition in the hcp phase caused by the overall presence of oxygen in the case of the two-step process. The hcp(O) phase used to model the asymmetric peak tails of the hcp peaks indicates an increase in the lattice constants a and c due to the presence of oxygen. This is expected and in agreement with the observations made for α-titanium [73].

The modeled peaks of the bcc(O) and hcp(O) phases to account for the observed asymmetric peak tails themselves are a superposition of reflexes coming from unit cells with various oxygen concentrations. A manual evaluation of the hcp phase after two-step oxidation is performed to assess the plausibility of the lattice parameter changes due to oxygen dissolution indicated by the refinement model. The reflexes corresponding to the crystal plane with the hkl indices (010) and (013) are used to determine the lattice constants a and c corresponding to a unit cell with a low and a high oxygen concentration. Figure 81 shows that a reflex associated with the maximum of the main hcp peak is selected to represent a unit cell of low oxygen concentration. An assumed additional reflex associated with the local maximum of the second derivation of

the asymmetric peak tail profile slope is chosen to represent a unit cell of high oxygen concentration.

Table 20: Comparison of experimentally obtained lattice parameters of TiZrNbHfTa after different oxidation processes and literature values.

	bcc1 a in pm	**bcc2** a in pm	**bcc3** a in pm	**hcp1** a, c in pm	**bcc(O)** a in pm	**hcp(O)** a, c in pm
experimental						
initial state *rolled*	340.4	-	-	-	-	-
single-step *substrate*	340.7	333.8	-	a = 318.7 c = 505.9 c/a =1.587	-	-
two-step *oxygen-enriched zone*	339.3	337.6	-	a = 320.2 c = 510.4 c/a =1.594	341.5	a = 321.8 c = 511.6 c/a =1.590
literature						
initial state [43] *as-cast*	340.4	-		-	-	-
initial state [45] *pressure torsion*	341.1					
initial state [60] *rolled & annealed*	340.8					
annealed [45] *500 °C, 100 h*	-	335.4		a = 319.8 c = 506.7 c/a =1.584		
annealed [59] *600 °C, theory*		333.3		a = 310.5 c = 501.5 c/a =1.615		
annealed [60] *700 °C, 96 h*		332.3	344.7	a = 314.3 c = 504.2 c/a =1.604		
annealed [45] *800 °C, 1 h*		334.5	344.9	a = 322.8 c = 511.5 c/a =1.585		

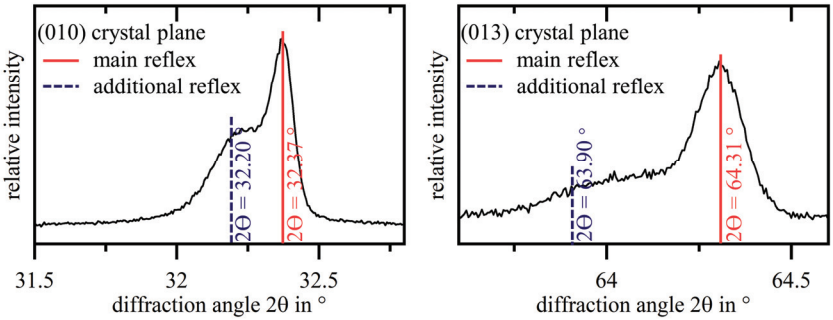

Figure 81: X-ray diffractograms of the subsurface region of TiZrNbHfTa after two-step oxidation (oxide layer removed) with peaks corresponding to the (010) and (013) crystal planes. An assumed additional reflex representing an oxygen-rich unit cell is set in contrast to the main reflex.

Table 21 shows the determined lattice misfits in relation to the results derived via the refinement model and literature values for commercially pure α-titanium. An increase of the lattice parameter a is observed, leading to a relative misfit that agrees well with the one determined via the refinement model and the literature. Regarding the lattice parameter c, both experimental approaches yield a lower relative misfit than reported in the literature on commercially pure α-titanium. However, oxygen dissolution is a reasonable explanation for the observed peak tails since the misfit reported in the literature is not exceeded.

Table 21: Relative lattice misfits of the TiZrNbHfTa hcp phases due to dissolved oxygen determined manually and via Rietveld analysis in contrast to literature values for commercially pure α-Ti.

	a in pm	***c*** in pm
experimental (manual)		
main reflex	319.1	509.7
assumed reflex	320.7	512.7
relative misfit in 10^{-3}	+5.0	+5.9
experimental (refinement)		
hcp1	320.2	510.4
hcp(O)	321.5	511.6
relative misfit in 10^{-3}	+4.1	+2.4
literature (α-Ti) [73]		
relative misfit in 10^{-3}	+4.7	+16.8

6.4 Evaluation of tribological properties

Numerous surface properties are investigated in section 5.3 (page 59). This reflects the complexity of a tribosystem and the multiple surface properties affecting the wear and friction behavior (section 2.1, page 2). Directional interdependencies between the studied surface properties exist. For example, a high surface hardness often leads to a low wear rate. In contrast, a low wear rate does not cause a high surface hardness. In this case, the wear rate can be considered a dependent variable, while the hardness is an independent variable. The terms independent and dependent variables are restricted to the scope of the experiment and the investigated surface properties. They can alternatively be understood as input and output variables. A design structure matrix is a valuable analysis tool to reveal interdependencies and identify dependent and independent variables [155]. Table 22 provides a design structure matrix with all the properties studied for Ti6Al4V and TiZrNbHfTa specimens in their initial state and after various oxidation processes. Dependent variables are: behavior in the knee joint wear test, wear coefficient (calo wear), wear rate (ball-on-disk), and friction coefficient (ball-on-disk).

Table 22: Design structure matrix revealing the interdependencies of the investigated tribological surface properties. The top left field depicts how to interpret the matrix.

A does not effect A (itself) A does not effect B A effects B A effects B and C B does not effect A or C C does not affect A or B → A is independent → B and C are dependent		surface morphology	layer adhesion	surface hardness	surface roughness	behavior in knee joint wear test	wear coefficient (calo wear)	wear trace (ball-on-disk)	wear rate (ball-on-disk)	friction coefficient (ball-on-disk)
surface morphology										
layer adhesion										
surface hardness										
surface roughness										
behavior in knee joint wear test										
wear coefficient (calo wear)										
ball-on-disk measurements (by Beyza Öztürk)	wear trace									
	wear rate									
	friction coefficient									

With the dependent and independent variables being defined based on Table 22, the respective surface properties need to be rated. A simple rating system is deployed since rating certain surface properties, like the surface morphology, involves a subjective interpretation. The ratings 1 (poor), 2 (intermediate), and 3 (good) are used. To give an overall relative ranking between the different oxidation processes and to compare Ti6Al4V with TiZrNbHfTa, the decision matrix method, as explained by Chang [156], is used.

Table 23 on page 91 and Table 24 on page 92 are such decision matrices. A ranking only considering dependent variables (Table 23) and an overall ranking including all studied variables (Table 24) are presented. The information on whether or not an oxide layer is present is included. The rating of each surface property is briefly discussed in the following.

Rating:

Surface morphology: Pores, in general, harm the wear resistance of materials [157, 158]. Therefore, single-step and three-step oxidation of Ti6Al4V is rated bad due to the accumulation of pores at the oxide-metal interface (Figure 15, page 25), locally weakening the surface and the oxide layer adhesion. Oxidation at reduced oxygen partial pressure of Ti6Al4V is rated intermediate since the pores are much smaller and not locally concentrated at the oxide-metal interface. The surface morphology of all other systems does not indicate any negative influences on the wear behavior.

Layer adhesion: The layer adhesion classification according to ISO 26443 already defines a rating systematic (Figure 18, page 27; Table 18, page 60). Class 3 is bad, class 2 is intermediate, and class 1 is good. If no oxide layer is present, there is no potential spallation of such a layer, and the rating good is chosen.

Surface hardness: The wear volume of a tribosystem is inversely proportional to the hardness of the softer counterpart [4]. Therefore, high hardness is advantageous. HV 0.01 measurements (Figure 59 a), page 61) are chosen for the evaluation because they better represent the hardness directly at the surface due to lower indentation depths. A hardness below 800 HV is rated bad, a hardness of up to 1200 HV is rated intermediate, and a hardness above 1200 HV is rated good.

Surface roughness: While the initial surface roughness, in the long run, is not affecting friction and wear in many technical systems [4], wear debris created due to the deformation of rough surfaces during the early stage of use can be detrimental in biomedical applications. Therefore, low initial surface roughness is desired. The rating is based on the R_a measurements, with R_a and R_z measurements reflecting the same trend (Figure 60, page 62). R_a values below 0.1 µm are rated good, values between 0.1 µm and 0.2 µm are rated intermediate, and values above 0.1 µm are rated bad.

Behavior in knee joint wear test: This test allows a qualitative evaluation of the surface deterioration using a realistic load scenario of an artificial knee implant (Figure 61, page 63). A specimen is rated bad if an oxide layer systematically detaches over the whole area of contact with the UHMW-PE cylinder, intermediate if only partial spallation due to intrinsic material defects occurs, and good if the surface is defect free except for homogeneous wear traces.

Wear coefficient (calo wear): The wear coefficients (Figure 62, page 63) explicitly express the resistance against wear. The lower the wear coefficient, the better. Median wear coefficients above $5 \cdot 10^{-13}$ m^2N^{-1} are rated bad, values between $5 \cdot 10^{-13}$ m^2N^{-1} and $1 \cdot 10^{-13}$ m^2N^{-1} are rated intermediate, and below $1 \cdot 10^{-13}$ m^2N^{-1} are rated good.

Wear trace (ball-on-disk): A qualitative rating is based on the wear trace impressions (Figure 63, page 64) regarding trace width and homogeneity of appearance. Ti6Al4V in its initial state and after single-step and three-step oxidation possess homogeneous but large wear traces and are rated bad. Ti6Al4V, after the two-step process, has a homogeneous, intermediate-sized wear trace, while oxidation at reduced oxygen partial pressure leads to a narrow wear trace but with discontinuities. Both are rated intermediate. For TiZrNbHfTa, the largest wear trace is observed after the two-step process, which is rated bad comparable to Ti6Al4V in the initial state. TiZrNbHfTa in the initial state is rated intermediate, while the single-step process is rated good due to the overall lowest wear trace width.

Wear rate (ball-on-disk): Similar to the wear coefficient (calo wear), the wear rate (Figure 64 a), page 65) directly expresses the resistance against wear, i.e., the lower the wear rate, the better. A wear rate below $0.5 \cdot 10^{-13}$ m^2N^{-1} is considered as good, between $0.5 \cdot 10^{-13}$ m^2N^{-1} and $1.5 \cdot 10^{-13}$ m^2N as intermediate, and above $1.5 \cdot 10^{-13}$ m^2N as poor.

Coefficient of friction (ball-on-disk): Since friction causes wear of two contacting bodies during relative motion, it should be minimized, and a low coefficient of friction is desired [4]. Friction coefficients below 0.7 are rated good, coefficients between 0.7 and 0.8 are rated intermediate, and coefficients above 0.8 are rated bad. This represents the clustering observed for the experimentally determined coefficients of friction (Figure 64 b), page 65).

Ranking:

The following evaluation outcome is drawn based on the decision matrix shown in Table 23, only considering the dependent variables according to Table 22 (page 88). An evaluation based on a decision matrix including the independent variables, given in Table 24, reflects a similar trend and can provide additional information once an application-related specification sheet exists.

Amongst the Ti6Al4V specimens possessing an oxide layer, oxidation at reduced oxygen partial pressure is ranked best. The decision matrix reveals that the tribological properties obtained via single-step and three-step oxidation of Ti6Al4V are comparable. Therefore, they are ranked equally. If the presence of an oxide layer is not required, two-step oxidation of Ti6Al4V is an attractive option to improve the tribological properties compared to the initial state.

Among the TiZrNbHfTa specimens with an oxide layer, the single-step process is ranked best. Also, in the overall comparison, single-step oxidation of TiZrNbHfTa leads to the best ranking regardless of whether only dependent variables or specimens with an oxide layer are considered. If an oxide layer is not a prerequisite, rolled TiZrNbHfTa in the initial state is ranked higher than TiZrNbHfTa after the two-step process.

Table 23: Decision matrix with the rated properties (dependent variables) obtained after various oxidation processes applied to Ti6Al4V and TiZrNbHfTa. Two rankings are derived: One considering all tested specimens and one only considering specimens with an oxide layer.

properties	Ti6Al4V					TiZrNbHfTa		
oxidation process	initial state	single-step	two-step	three-step	partial pressure	initial state	**single-step**	two-step
behavior in knee joint wear test	3	1	3	1	3	3	**2**	3
wear coefficient (calo wear)	1	1	3	1	1	3	**3**	3
wear rate (ball-on-disk)	1	2	1	2	3	2	**3**	1
friction coefficient (ball-on-disk)	3	1	2	1	1	2	**2**	2
presence of an oxide layer	no	yes	no	yes	yes	no	**yes**	yes
rating	8	4	9	5	8	8	**10**	9
ranking (all.)	3	5	2	4	3	3	**1**	2
ranking (with oxide layer only)	-	5	-	4	3	-	**1**	2

Table 24: Decision matrix with the rated properties (dependent and independent variables) obtained after various oxidation processes applied to Ti6Al4V and TiZrNbHfTa. Two rankings are derived: One considering all tested specimens and one only considering specimens with an oxide layer.

properties	Ti6Al4V					TiZrNbHfTa		
oxidation process	initial state	single-step	two-step	three-step	partial pressure	initial state	**single-step**	two-step
surface morphology	3	1	3	1	2	3	**3**	3
layer adhesion	3	1	3	2	3	3	**3**	3
surface hardness	1	1	2	2	2	1	**3**	3
surface roughness	3	1	2	1	2	2	**2**	1
behavior in knee joint wear test	3	1	3	1	3	3	**2**	3
wear coefficient (calo wear)	1	1	3	1	1	3	**3**	3
wear trace (ball-on-disk)	1	1	2	1	2	2	**3**	1
wear rate (ball-on-disk)	1	2	1	2	3	2	**3**	1
friction coefficient (ball-on-disk)	3	1	2	1	1	2	**2**	2
presence of an oxide layer	no	yes	no	yes	yes	no	**yes**	yes
rating	19	10	21	12	19	21	**24**	20
ranking (all.)	4	6	2	5	4	2	**1**	3
ranking (with oxide layer only)	-	5	-	4	3	-	**1**	2

7 Conclusions

Ti6Al4V

- The oxygen concentration-depth and correlated hardness-depth profiles can be tailored through a single-step, two-step, or three-step process and oxidation at reduced oxygen partial pressure. The largest oxygen diffusion depths, in combination with a gradual oxygen concentration decrease underneath an oxide layer, are achieved via three-step oxidation and oxidation at reduced oxygen partial pressure. The chosen oxidation process also affects the surface appearance, surface morphology, surface grain constitution, surface roughness, subsurface microstructure, and surface hardness.
- Besides the shape of the oxygen concentration- and hardness-depth profiles, the oxide layer morphology turns out to be important for its adhesion. The formation of large pores in the oxide layer close to the oxide-metal interface after the single-step and the three-step process is disadvantageous compared to the fine, homogeneously distributed pores resulting from oxidation at reduced oxygen partial pressure. While the three-step process leads to a slightly improved oxide layer adhesion compared to the single-step process, the adhesion is best after oxidation at reduced oxygen partial pressure.

➢ Oxidation at reduced oxygen partial pressure, after the removal of needle-shaped surface oxide grains, leads to the best wear behavior. The wear coefficient (calo wear) and the wear rate (ball-on-disk) are the lowest of all tested Ti6Al4V specimens.

TiZrNbHfTa

- As-cast and rolled & annealed TiZrNbHfTa with coarse grains (grain size $\gtrsim$ 50 µm) exhibit catastrophic oxidation during oxidation in air at 600 °C. This is due to a localized phase decomposition at the (sub)grain boundaries, rapid oxygen diffusion along the grain boundaries, and localized oxygen dissolution or internal oxidation at the grain boundaries leading to localized internal stresses and intergranular cracking.
- Cold-rolled ultrafine-grained TiZrNbHfTa (grain size ~200 nm) forms an adherent, micrometer-sized surface oxide layer during oxidation in air in the temperature range of 550 °C to 650 °C. A homogeneous phase decomposition of the initial single-phase bcc material occurs throughout the specimen with a homogeneous oxygen inward diffusion causing internal oxidation of Hf and Zr in an oxygen-enriched zone beneath the surface oxide layer. A native oxide layer forms on TiZrNbHfTa at ambient conditions.
- During oxidation of ultrafine-grained rolled TiZrNbHfTa, the mass gain and growth of an oxygen-enriched zone, including a surface oxide layer, follow a parabolic rate law.
- Two-step oxidation of TiZrNbHfTa is possible. Instead of dissolving oxygen from a surface oxide layer, as for Ti6Al4V, the internal oxides in the oxygen-enriched zone get reduced. Due to the dissolved oxygen, Hf- and Zr- rich Ti-containing hcp precipitates of several micrometer size form in a Nb- and Ta- rich bcc matrix while the substrate is single phase bcc. An overall decreasing hardness over depth in the oxygen diffusion zone is obtained while the oxygen concentration and hardness between bcc matrix and hcp precipitates differs.

- Single-step and two-step oxidation of TiZrNbHfTa both lead to the presence of a micrometer-sized surface oxide layer. While the surface appearance and surface morphology are similar, differences in surface roughness, surface hardness, and subsurface microstructure occur. The subsurface microstructure influences the oxygen concentration-depth and hardness-depth profiles. Also, the substrate is affected by the process being single-phase bcc after the two-step process and two-phase bcc/hcp on a nanometer-scale after the single-step process. A three-step process is not expected to work because catastrophic oxidation similar to rolled & annealed material will likely occur during an additional final oxidation step. Oxidation at reduced oxygen partial pressure leads to identical results to the single-step process.
- Single-step oxidation of rolled, ultrafine-grained TiZrNbHfTa is ranked best amongst all the studied specimens. It leads to surfaces with good oxide layer adhesion, tremendous hardness, and superior wear behavior with respect to wear volume.

8 Summary

This work investigates four different oxidation processes to modify the surface of Ti6Al4V and the equimolar high entropy alloy TiZrNbHfTa. The aim is to generate hard, adherent oxide layers with an underlying pronounced oxygen diffusion zone exhibiting a gradual hardness decrease. This can positively affect the tribological behavior of both alloy systems and, in particular, improve their wear resistance. The studied oxidation processes are: a single-step process consisting of oxidation in air, a two-step process in which oxidation in air is followed by an oxide reduction under vacuum, a three-step process in which the oxide reduction is followed by another oxidation step, and an oxidation process at reduced oxygen partial pressure.

Single-step oxidation of Ti6Al4V (680 °C, 16 h, in air) leads to an oxide layer predominantly of TiO_2 rutile. Large pores accumulating at the oxide-metal interface result in poor oxide layer adhesion. The achieved oxygen diffusion zone, causing a gradual hardness decrease, extends only to a depth of ~ 20 µm. Overall, the tribological performance is poor.

After two-step oxidation of Ti6Al4V (single-step + 850 °C, 6 h, vacuum), the oxide layer is successfully reduced, while the oxygen diffusion zone is significantly enhanced (~85 µm). The oxygen concentration in shallow depths of ~10 at.% is lower compared to the single-step process (~20 at.%). Despite the absence of an oxide layer, the two-step process improves the tribological performance compared to Ti6Al4V in the initial state.

Three-step oxidation of Ti6Al4V (two-step + 680 °C, 16 h, in air) results in an oxygen concentration- and hardness-depth profile representing a superposition of the profiles obtained via the single-step and the two-step processes. This positively affects oxide layer adhesion, while large pores accumulating at the oxide-metal interface are responsible for an overall poor tribological performance.

Oxidation at reduced oxygen partial pressure (850 °C, 2 h, $p_{O2} \approx 1 \cdot 10^{-13}$ Pa) leads to the best result. With just one process step, an oxygen concentration- and hardness-depth profile analogous to the three-step process can be obtained. Due to the absence of a pore allocation at the oxide-metal interface, a multilayered oxide layer with good oxide layer adhesion and the best wear behavior of all Ti6Al4V specimens is achieved.

This work demonstrates that by properly choosing an oxidation process with suitable parameters, one can significantly influence: the surface composition and morphology, the layer adhesion, the formation of an oxygen diffusion zone leading to a gradual hardness decrease, the surface hardness, and the wear behavior. For the first time to the author's knowledge, the vast potential of oxidation at reduced oxygen partial pressure to improve the tribological performance of Ti6Al4V is described and understood in detail.

Until now, oxidation of TiZrNbHfTa is poorly investigated and only harmful catastrophic oxidation has been reported. Coarse-grained TiZrNbHfTa (grain size $\gtrsim$ 50 µm) studied in this work also exhibits catastrophic oxidation at 600 °C in air. In contrast, a micrometer-sized, compact surface oxide layer forms on cold-rolled ultrafine-grained TiZrNbHfTa (grain size

~200 nm). Based on these novel findings, two mechanisms linking the oxidation behavior of TiZrNbHfTa to its microstructure are proposed.

In the case of coarse-grained material, local stress concentrations at the grain boundaries result in intergranular cracking and scale spallation at the surface. According to this work, such local stress concentrations at the grain boundaries occur due to a localized phase decomposition at the grain boundaries, rapid oxygen diffusion along the grain boundaries, and localized oxygen dissolution and internal oxidation at the grain boundaries.

For ultrafine-grained material, a rapid phase decomposition occurs underneath the micrometer-sized surface oxide layer. This results in a two-phase microstructure on the nanometer scale, consisting of a body-centered cubic phase and a hexagonal close-packed phase. The microstructure is still homogeneous on the micrometer scale, which is why a homogeneous inward diffusion of oxygen occurs over the entire sample surface. Localized stress concentrations are avoided, and catastrophic oxidation is not observed.

Single-step oxidation of ultrafine-grained TiZrNbHfTa (600 °C, 8 h, in air) can therefore be used as a surface hardening method. It leads to an adherent surface oxide layer (~2 µm) forming on top of an oxygen-enriched zone (~30 µm) with internal hafnium and zirconium oxides.

The two-step oxidation of TiZrNbHfTa (550 °C, 24 h, in air + 1200 °C, 1 h, vacuum + quenching) works fundamentally different from that of Ti6Al4V. The vacuum heat treatment at 1200 °C reduces the internal oxides formed during the single-step process while the surface oxide layer remains present. Oxygen released by the reduction of the internal oxides gets dissolved and stabilizes hexagonal close-packed precipitates in a body-centered cubic matrix in a subsurface region of ~85 µm depth. The substrate becomes single-phase. While the surface hardness and the hardness in the subsurface region are increased compared to the initial state, the wear resistance remains below that obtained after single-step oxidation.

Due to the phase transformations occurring during oxidation of TiZrNbHfTa, a three-step oxidation process is not promising. In contrast to Ti6Al4V, oxidation at reduced oxygen partial pressure leads to similar results as the single-step process.

Aiming for increased surface hardness to improve the wear resistance, single-step oxidation of ultrafine-grained rolled TiZrNbHfTa is very promising. Compared to the initial rolled state (~350 HV0.5), the surface hardness can be increased by more than four times via single-step oxidation (~1520 HV0.5). Pores occur neither in the surface oxide layer nor the oxygen-enriched zone, and the layer adhesion is good. This results in an excellent wear resistance superior to that of all other TiZrNbHfTa and Ti6Al4V samples.

With the first-ever successful application of single-step and two-step oxidation of TiZrNbHfTa to the author's knowledge in this work, two new surface-hardening approaches are available for TiZrNbHfTa. The superior tribological properties compared to Ti6Al4V make TiZrNbHfTa an exciting alternative for future biocompatible components with high wear resistance requirements. This finding is an important step towards artificial joint implants with an increased service life.

9 Zusammenfassung

In dieser Arbeit werden vier verschiedene Oxidationsprozesse zur Oberflächenmodifikation von Ti6Al4V und der äquimolaren Hochentropielegierung TiZrNbHfTa untersucht. Ziel ist es, harte, haftende Oxidschichten auf einer ausgeprägten Sauerstoffdiffusionszone mit graduellem Härteverlauf zu generieren. Dies soll sich positiv auf das tribologische Verhalten auswirken und Verschleiß minimieren. Zu den untersuchten Prozessen zählen: ein einstufiger Prozess bestehend aus Oxidation an Luft, ein zweistufiger Prozess bei dem auf die Oxidation an Luft eine Oxidreduktion unter Vakuum folgt, ein dreistufiger Prozess bei dem auf die Oxidreduktion eine erneute Oxidation an Luft erfolgt und eine Oxidation bei reduziertem Sauerstoffpartialdruck.

Der einstufige Prozess (680 °C, 16 h, Luft) führt bei Ti6Al4V zu einer Oxidschicht überwiegend aus TiO_2-Rutil. An der Oxid-Metall-Grenzfläche treten große Poren auf, was zu einer schlechten Schichthaftung führt. Die erzielte Sauerstoffdiffusionszone mit graduellem Härteverlauf reicht lediglich ~20 µm tief. Insgesamt ist das tribologische Verhalten schlecht.

Die zweistufige Oxidation (einstufig + 850 °C, 6 h, Vakuum) führt zu einer erfolgreichen Reduktion der Oxidschicht bei gleichzeitiger Vergrößerung der Sauerstoffdiffusionszone (~85 µm). Die Sauerstoffkonzentration in geringen Tiefen ist mit ~10 at.% im Vergleich zum einstufigen Prozess (~20 at.%) reduziert. Insgesamt stellt sich dennoch eine Aufhärtung der Oberfläche ein, welche sich verschleißminimierend auswirkt.

Durch die dreistufige Oxidation (zweistufig + 680 °C, 16 h, Luft) wird ein Sauerstoffkonzentrations- und Härte-Tiefenprofil erzielt, welches eine Superposition der Profile des einstufigen und zweistufigen Prozesses darstellt. Dies wirkt sich positiv auf die Schichthaftung aus. Jedoch bildet sich erneut eine TiO_2-Rutil Oxidschicht mit großen Poren im Bereich der Oxid-Metall-Grenzfläche aus, was sich in einem schlechten tribologischen Verhalten niederschlägt.

Oxidation bei reduziertem Sauerstoffpartialdruck (850 °C, 2 h, $p_{O2} \approx 1 \cdot 10^{-13}$ Pa) führt zum besten Ergebnis. Durch nur einen Prozessschritt kann ein Sauerstoffkonzentrations- und Härte-Tiefenprofil analog zum dreistufigen Prozess erreicht werden. Da an der Oxid-Metall-Grenzfläche keine Allokation von Poren auftritt, besitzt die mehrschichtige Oxidschicht eine gute Schichthaftung und die höchste Verschleißbeständigkeit unter den Ti6Al4V Proben.

Diese Arbeit zeigt, dass durch die Gestaltung des Oxidationsprozesses ein signifikanter Einfluss auf die Oberflächenzusammensetzung und -morphologie, die Schichthaftung, die Ausprägung einer Sauerstoffdiffusionszone samt eines graduellen Härteverlaufs, die Oberflächenhärte, sowie die Verschleißeigenschaften genommen werden kann. Nach Kenntnis des Autors erstmals wird dabei das enorme Potenzial der Oxidation bei reduziertem Sauerstoffpartialdruck zur Verbesserung der tribologischen Eigenschaften von Ti6Al4V beschrieben.

Das Oxidationsverhalten von TiZrNbHfTa war bislang kaum verstanden. Bisher wurde ausschließlich schädliche, katastrophale Oxidation beobachtet. Auch in dieser Arbeit tritt bei Oxidation von grobkörnigem TiZrNbHfTa (Korngröße $\gtrsim$ 50 µm) in Luft bei 600 °C katastrophale Oxidation auf. Dagegen bildet sich bei kaltgewalztem ultrafeinkörnigem Material (Korngröße ~200 nm) eine kompakte, mikrometerdicke Oxiddeckschicht aus. Auf Basis dieser

neuartigen Beobachtung werden zwei Mechanismen vorgeschlagen, die das Oxidationsverhalten von TiZrNbHfTa mit dessen Mikrostruktur in Verbindung bringen.

Bei grobkörnigem Material führen lokale Spannungskonzentrationen an den Korngrenzen zu intergranularer Rissbildung und zu Abplatzungen an der Oberfläche während der Oxidation. Die lokalen Spannungskonzentrationen sind zurückzuführen auf eine lokale Phasenentmischung und schnelle Sauerstoffeindiffusion entlang der Korngrenzen sowie innere Oxidation und interstitielles Lösen des Sauerstoffs an den Korngrenzen.

Bei ultrafeinkörnigem Material dagegen kommt es unterhalb der Oxiddeckschicht in kurzer Zeit zu einer Phasenentmischung. Dies führt zu einer zweiphasigen Struktur auf Nanometerebene, bestehend aus einer kubisch-raumzentrierten und einer hexagonal-dichtest-gepackten Phase. Auf Mikrometerbetrachtungsebene ist das Gefüge jedoch homogen, weshalb es zu einer homogenen Eindiffusion von Sauerstoff über die gesamte Probenoberfläche kommt. Lokale Spannungskonzentrationen, und damit katastrophale Oxidation, werden dadurch vermieden.

Einstufige Oxidation von ultrafeinkörnigem TiZrNbHfTa (600 °C, 8 h, Luft) kann daher als Oberflächenhärtungsmethode eingesetzt werden. Sie führt zu einer haftenden Oxiddeckschicht (~2 µm) auf einer sauerstoffreichen Zone (~30 µm) mit inneren Hafnium- und Zirkonoxiden.

Die zweistufige Oxidation von TiZrNbHfTa (550 °C, 24 h, Luft + 1200 °C, 1 h, Vakuum + Abschrecken) verläuft grundsätzlich verschieden zu der von Ti6Al4V. Die Vakuumwärmebehandlung bei 1200 °C reduziert die im einstufigen Prozess entstanden inneren Oxide, wobei die Oxiddeckschicht vorhanden bleibt. Die Reduktion der inneren Oxide setzt Sauerstoff frei. Dieser geht in Lösung und stabilisiert hexagonal-dichtest-gepackte Ausscheidungen in einer kubisch-raumzentrierten Matrix in der Randzone (~85 µm). Das Substrat wird einphasig. Trotz im Vergleich zum Ausgangszustand gesteigerter Oberflächenhärte und Härte in der Randzone ist die erzielte Verschleißbeständigkeit verglichen mit dem einstufigen Prozess geringer.

Aufgrund der Phasenumwandlungen während der Oxidation von TiZrNbHfTa ist die dreistufige Oxidation nicht zielführend. Oxidation bei reduziertem Sauerstoffpartialdruck führt, anders als bei Ti6Al4V, zu vergleichbaren Ergebnissen wie die einstufige Oxidation.

Bezüglich des Ziels die Oberflächenhärte zu steigern, um Verschleiß zu minimieren, ist die einstufige Oxidation von ultrafeinkörnigem TiZrNbHfTa sehr vielversprechend. Diese kann die Oberflächenhärte verglichen mit dem Ausgangsmaterial (~350 HV0.5) mehr als vervierfachen (~1520 HV0.5). Poren treten weder in der Oxiddeckschicht noch in der sauerstoffreichen Zone darunter auf, was zu guter Schichthaftung führt. Dies resultiert in exzellenter Verschleißbeständigkeit, welche der der anderen TiZrNbHfTa und Ti6Al4V Proben deutlich überlegen ist.

Mit dem nach Kenntnis des Autors erstmalig erfolgreichen Einsatz der einstufigen und zweistufigen Oxidation von TiZrNbHfTa in dieser Arbeit stehen zwei neue Ansätze zur Oberflächenhärtung von TiZrNbHfTa zur Verfügung. Die überlegenen tribologischen Eigenschaften im Vergleich zu Ti6Al4V machen TiZrNbHfTa zu einer attraktiven Alternative für biokompatible Bauteile mit hohen Verschleißbeständigkeitsanforderungen. Diese Erkenntnis ist ein wichtiger Schritt auf dem Weg zu künstlichen Gelenken mit deutlich längerer Lebensdauer.

10 Literature

[1] OECD; *Health at a glance 2021 – OECD indicators*, (2022) doi:10.1787/ae3016b9-en.

[2] Statista; *Anzahl der Implantationen künstlicher Kniegelenke in deutschen Krankenhäusern in den Jahren 2005 bis 2021*, (2022) de.statista.com/statistik/daten/studie/785084/umfrage/implantationen-kuenstlicher-kniegelenke-in-deutschen-krankenhaeusern/; accessed: 23.12.2022.

[3] Statista; *Anzahl der Implantationen künstlicher Kniegelenke in deutschen Krankenhäusern nach Altersgruppe im Jahr 2021*, (2022) de.statista.com/statistik/daten/studie/785126/umfrage/implantationen-kuenstlicher-kniegelenke-in-deutschen-krankenhaeusern-nach-alter/; accessed: 23.12.2022.

[4] Menezes, P.L.; Nosonovsky, M.; Ingole, S.P.; Kailas, S.V.; Lovell, M.R.; *Tribology for Scientists and Engineers – From Basics to Advanced Concepts*; Springer New York, New York, NY, (2013) ISBN:9781461419440.

[5] Lütjering, G.; Williams, J.C.; *Titanium*, Engineering materials and processes; Springer-Verlag, Berlin Heidelberg, (2007) ISBN:9783540713975.

[6] Lin N., Xie R., Zou J., Qin J., Wang Y., Yuan S., Li D., Zhao L., Zhang L., Wang Z., Ma Y., Han P., Tian W., Liu X., Wang Z., Tang B.; *Surface damage mitigation of titanium and its alloys via thermal oxidation: A brief review*; Reviewes on Advanced Materials Science 58, (2019) 132-146 doi:10.1515/rams-2019-0012.

[7] Güleryüz H., Atar E., Seahjani F., Çimenoğlu H.; *An overview on surface hardening of titanium alloys by diffusion of interstitial atoms*; Diffusion Foundations 4, (2015) 103-116 doi:10.4028/www.scientific.net/DF.4.103.

[8] Dearnley P.A., Dahm K.L., Çimenoğlu H.; *The corrosion–wear behaviour of thermally oxidised CP-Ti and Ti–6Al–4V*; Wear 256, (2004) 469-479 doi:10.1016/S0043-1648(03)00557-X.

[9] Mosbacher M., Hilzenthaler M., Galetz M., Glatzel U.; *Oxygen diffusion hardened zirconium alloy ZrNb7 – Tribological properties derived from Calo wear and wheel on flat experiments*; Tribology International 165, (2022) 107304 doi:10.1016/j.triboint.2021.107304.

[10] Geetha M., Singh A.K., Asokamani R., Gogia A.K.; *Ti based biomaterials, the ultimate choice for orthopaedic implants – A review*; Progress in Materials Science 54, (2009) 397-425 doi:10.1016/j.pmatsci.2008.06.004.

[11] Gueye M., Ammar-Merah S., Nowak S., Decorse P., Chevillot-Biraud A., Perrière L., Couzinie J.P., Guillot I., Dirras G.; *Study of the stability under in vitro physiological conditions of surface silanized equimolar HfNbTaTiZr high-entropy alloy: A first step toward bio-implant applications*; Surface and Coatings Technology 385, (2020) 125374 doi:10.1016/j.surfcoat.2020.125374.

[12] Motallebzadeh A.; *Evaluation of mechanical properties and in vitro biocompatibility of TiZrTaNbHf refractory high-entropy alloy film as an alternative coating for TiO2 layer on NiTi alloy*; Surface and Coatings Technology 448, (2022) 128918 doi:10.1016/j.surfcoat.2022.128918.

[13] Okamoto H.; *O-Ti (Oxygen-Titanium)*; Journal of Phase Equilibria and Diffusion 32, (2011) 473-474 doi:10.1007/s11669-011-9935-5.

[14] Wang C., Zinkevich M., Aldinger F.; *On the thermodynamic modeling of the Zr–O system*; Calphad 28, (2004) 281-292 doi:10.1016/j.calphad.2004.09.002.

[15] Abriata J.P., Garcés J., Versaci R.; *The O−Zr (Oxygen-Zirconium) system*; Bulletin of Alloy Phase Diagrams 7, (1986) 116-124 doi:10.1007/BF02881546.

[16] Rudy E., Stecher P.; *Zum Aufbau des Systems Hafnium-Sauerstoff*; Journal of the Less Common Metals 5, (1963) 78-89 doi:10.1016/0022-5088(63)90045-6.

[17] Okamoto H.; *Hf-O (Hafnium-Oxygen). In: Massalski, T.B.; Okamoto, H.; Subramanian, P.R. et al.* (eds.): Binary alloy phase diagrams. ASM International. ASM International, Metals Park, Ohio, (1990).

[18] Chang C.-H., Titus M.S., Yeh J.-W.; *Oxidation behavior between 700 and 1300 °C of refractory TiZrNbHfTa high-entropy alloys containing aluminum*; Advanced Engineering Materials 20, (2018) 1700948 doi:10.1002/adem.201700948.

[19] Dwivedi, D.K.; *Surface Engineering – Enhancing Life of Tribological Components*; Springer India, New Delhi, (2018) ISBN:9788132237778.

[20] Blau, P.J.; *Tribosystem Analysis – A Practical Approach to the Diagnosis of Wear Problems*; CRC Press, Taylor & Francis Group, Boca Raton, (2016) ISBN:9781498700511.

[21] Thomas J.B.; *Titanium.* White, W.M. (ed.): Encyclopedia of Geochemistry, Encyclopedia of Earth Sciences Series. Springer International Publishing, Cham, (2018) 1445-1451.

[22] Shackelford, J.F.; Alexander, W.; *CRC Materials Science and Engineering Handbook*; CRC Press, (2000) ISBN:9780429117862.

[23] Brunette, D.M.; Tengvall, P.; Textor, M.; Thomsen, P.; *Titanium in Medicine – Material Science, Surface Science, Engineering, Biological Responses and Medical Applications*, Engineering Materials; Springer, Berlin, (2001) ISBN:9783642631191.

[24] Titanium Metals Corporation; *Processing and properties of TIMETAL 6-4*, (1998) timet.com/assets/local/documents/technicalmanuals/TIMETAL_6-4_Properties.pdf; accessed: 29.10.2019.

[25] Zhang Z.X., DONG H., BELL T., Xu B.; *The effect of treatment condition on boost diffusion of thermally oxidised titanium alloy*; Journal of Alloys and Compounds 431, (2007) 93-99 doi:10.1016/j.jallcom.2006.05.045.

[26] Biswas A., Dutta Majumdar J.; *Surface characterization and mechanical property evaluation of thermally oxidized Ti-6Al-4V*; Materials Characterization 60, (2009) 513-518 doi:10.1016/j.matchar.2008.12.014.

[27] Anilkumar S., Aneela R., Srikanth, Vadali V. S. S.; *Construction of Phase Diagrams for AlxHfNbTaTiZr Refractory High Entropy Alloy*; Transactions of the Indian Institute of Metals 71, (2018) 901-907 doi:10.1007/s12666-017-1221-8.

[28] Zabler S.; *Interstitial oxygen diffusion hardening — A practical route for the surface protection of titanium*; Materials Characterization 62, (2011) 1205-1213 doi:10.1016/j.matchar.2011.10.012.

[29] Keller J.C., Stanford C.M., Wightman J.P., Draughn R.A., Zaharias R.; *Characterizations of titanium implant surfaces. III*; Journal of Biomedical Materials Research 28 (1994) 939-946 doi:10.1002/jbm.820280813.

[30] Shah F.A., Trobos M., Thomsen P., Palmquist A.; *Commercially pure titanium (cp-Ti) versus titanium alloy (Ti6Al4V) materials as bone anchored implants - Is one truly better than the other?*; Materials science & engineering. C, Materials for biological applications 62 (2016) 960-966 doi:10.1016/j.msec.2016.01.032.

[31] Yeh J.-W., Chen S.-K., Lin S.-J., Gan J.-Y., Chin T.-S., Shun T.-T., Tsau C.-H., Chang S.-Y.; *Nanostructured high-entropy alloys with multiple principal elements: Novel alloy design concepts and outcomes*; Advanced Engineering Materials 6, (2004) 299-303 doi:10.1002/adem.200300567.

[32] Cantor B., Chang I.T.H.; *Microstructural development in equiatomic multicomponent alloys*; Materials Science and Engineering: A 375-377, (2004) 213-218 doi:10.1016/j.msea.2003.10.257.

[33] Murty, B.S.; Yeh, J.W.; Ranganathan, S.; *High entropy alloys*; Butterworth-Heinemann, London, (2014) ISBN:9780128002513.

[34] Senkov O.N., Miracle D.B., Chaput K.J., Couzinie J.-P.; *Development and exploration of refractory high entropy alloys—A review*; Journal of Materials Research 33, (2018) 3092-3128 doi:10.1557/jmr.2018.153.

[35] Cheng K.-H., Lai C.-H., Lin S.-J., Yeh J.-W.; *Recent progress in multi-element alloy and nitride coatings sputtered from high-entropy alloy targets*; Annales de Chimie Science des Matériaux 31, (2006) 723-736 doi:10.3166/acsm.31.723-736.

[36] Yeh J.-W.; *Alloy design strategies and future trends in high-entropy alloys*; JOM 65, (2013) 1759-1771 doi:10.1007/s11837-013-0761-6.

[37] Biswas K., Yeh J.-W., Bhattacharjee P.P., DeHosson J.T.; *High entropy alloys: Key issues under passionate debate*; Scripta Materialia 188, (2020) 54-58 doi:10.1016/j.scriptamat.2020.07.010.

[38] Miracle D.B.; *High-entropy alloys: A current evaluation of founding ideas and core effects and exploring "nonlinear alloys"*; JOM 69, (2017) 2130-2136 doi:10.1007/s11837-017-2527-z.

[39] Zhang J., Gadelmeier C., Sen S., Wang R., Zhang X., Zhong Y., Glatzel U., Grabowski B., Wilde G., Divinski S.V.; *Zr diffusion in BCC refractory high entropy alloys: A case of 'non-sluggish' diffusion behavior*; Acta Materialia 233, (2022) 117970 doi:10.1016/j.actamat.2022.117970.

[40] Otto F., Yang Y., Bei H., George E.P.; *Relative effects of enthalpy and entropy on the phase stability of equiatomic high-entropy alloys*; Acta Materialia 61, (2013) 2628-2638 doi:10.1016/j.actamat.2013.01.042.

[41] Inui H., Kishida K., Le Li, Manzoni A.M., Haas S., Glatzel U.; *Uniaxial mechanical properties of face-centered cubic single- and multiphase high-entropy alloys*; MRS Bulletin 47, (2022) 168-174 doi:10.1557/s43577-022-00280-y.

[42] George E.P., Raabe D., Ritchie R.O.; *High-entropy alloys*; Nature Reviews Materials 4, (2019) 515-534 doi:10.1038/s41578-019-0121-4.

[43] Senkov O.N., Scott J.M., Senkova S.V., Miracle D.B., Woodward C.F.; *Microstructure and room temperature properties of a high-entropy TaNbHfZrTi alloy*; Journal of Alloys and Compounds 509, (2011) 6043-6048 doi:10.1016/j.jallcom.2011.02.171.

[44] Otto F., Dlouhý A., Pradeep K.G., Kuběnová M., Raabe D., Eggeler G., George E.P.; *Decomposition of the single-phase high-entropy alloy CrMnFeCoNi after prolonged anneals at intermediate temperatures*; Acta Materialia 112, (2016) 40-52 doi:10.1016/j.actamat.2016.04.005.

[45] Schuh B., Völker B., Todt J., Schell N., Perrière L., Li J., Couzinié J.P., Hohenwarter A.; *Thermodynamic instability of a nanocrystalline, single-phase TiZrNbHfTa alloy and its impact on the mechanical properties*; Acta Materialia 142, (2018) 201-212 doi:10.1016/j.actamat.2017.09.035.

[46] Barker, H.; Okamoto, H.; Henry, S.D.; Davidson, G.M.; Flemming, M.A.; Kacprzak, L.; Lampman, H.F. (eds.); *ASM Handbook – Volume 3 Alloy Phase Diagramms*; ASM International, Materials Park, Ohio, (1992).

[47] Murray J.L.; *Calculation of the titanium-aluminum phase diagram*; Metallurgical and Materials Transactions A 19, (1988) 243-247 doi:10.1007/BF02652532.

[48] Couzinié J.P., Dirras G., Perrière L., Chauveau T., Leroy E., Champion Y., Guillot I.; *Microstructure of a near-equimolar refractory high-entropy alloy*; Materials Letters 126, (2014) 285-287 doi:10.1016/j.matlet.2014.04.062.

[49] Lin C.-M., Juan C.-C., Chang C.-H., Tsai C.-W., Yeh J.-W.; *Effect of Al addition on mechanical properties and microstructure of refractory AlxHfNbTaTiZr alloys*; Journal of Alloys and Compounds 624, (2015) 100-107 doi:10.1016/j.jallcom.2014.11.064.

[50] Dirras G., Lilensten L., Djemia P., Laurent-Brocq M., Tingaud D., Couzinié J.-P., Perrière L., Chauveau T., Guillot I.; *Elastic and plastic properties of as-cast equimolar TiHfZrTaNb high-entropy alloy*; Materials Science and Engineering: A 654, (2016) 30-38 doi:10.1016/j.msea.2015.12.017.

[51] Senkov O.N., Semiatin S.L.; *Microstructure and properties of a refractory high-entropy alloy after cold working*; Journal of Alloys and Compounds 649, (2015) 1110-1123 doi:10.1016/j.jallcom.2015.07.209.

[52] Juan C.-C., Tsai M.-H., Tsai C.-W., Hsu W.-L., Lin C.-M., Chen S.-K., Lin S.-J., Yeh J.-W.; *Simultaneously increasing the strength and ductility of a refractory high-entropy alloy via grain refining*; Materials Letters 184, (2016) 200-203 doi:10.1016/j.matlet.2016.08.060.

[53] Senkov O.N., Pilchak A.L., Semiatin S.L.; *Effect of cold deformation and annealing on the microstructure and tensile properties of a HfNbTaTiZr refractory high entropy alloy*; Metallurgical and Materials Transactions A 49, (2018) 2876-2892 doi:10.1007/s11661-018-4646-8.

[54] Lilensten L., Couzinié J.-P., Perrière L., Hocini A., Keller C., Dirras G., Guillot I.; *Study of a bcc multi-principal element alloy: Tensile and simple shear properties and underlying deformation mechanisms*; Acta Materialia 142, (2018) 131-141 doi:10.1016/j.actamat.2017.09.062.

[55] Eleti R.R., Raju V., Veerasham M., Reddy S.R., Bhattacharjee P.P.; *Influence of strain on the formation of cold-rolling and grain growth textures of an equiatomic HfZrTiTaNb refractory high entropy alloy*; Materials Characterization 136, (2018) 286-292 doi:10.1016/j.matchar.2017.12.034.

[56] Laplanche G., Gadaud P., Perrière L., Guillot I., Couzinié J.P.; *Temperature dependence of elastic moduli in a refractory HfNbTaTiZr high-entropy alloy*; Journal of Alloys and Compounds 799, (2019) 538-545 doi:10.1016/j.jallcom.2019.05.322.

[57] Wang S., Wu M., Da Shu, Zhu G., Wang D., Sun B.; *Mechanical instability and tensile properties of TiZrHfNbTa high entropy alloy at cryogenic temperatures*; Acta Materialia 201, (2020) 517-527 doi:10.1016/j.actamat.2020.10.044.

[58] Gadelmeier C., Yang Y., Glatzel U., George E.P.; *Creep strength of refractory high-entropy alloy TiZrHfNbTa and comparison with Ni-base superalloy CMSX-4*; Cell Reports Physical Science, (2022) 100991 doi:10.1016/j.xcrp.2022.100991.

[59] Chen S.-M., Ma Z.-J., Qiu S., Zhang L.-J., Zhang S.-Z., Yang R., Hu Q.-M.; *Phase decomposition and strengthening in HfNbTaTiZr high entropy alloy from first-principles calculations*; Acta Materialia 225, (2022) 117582 doi:10.1016/j.actamat.2021.117582.

[60] Chen S.Y., Tong Y., Tseng K.-K., Yeh J.-W., Poplawsky J.D., Wen J.G., Gao M.C., Kim G., Chen W., Ren Y., Feng R., Li W.D., Liaw P.K.; *Phase transformations of HfNbTaTiZr high-entropy alloy at intermediate temperatures*; Scripta Materialia 158, (2019) 50-56 doi:10.1016/j.scriptamat.2018.08.032.

[61] Iroc L.K., Tukac O.U., Tanrisevdi B.B., El-Atwani O., Tunes M.A., Kalay Y.E., Aydogan E.; *Design of oxygen-doped TiZrHfNbTa refractory high entropy alloys with enhanced strength and ductility*; Materials & Design 223, (2022) 111239 doi:10.1016/j.matdes.2022.111239.

[62] Niinomi M., Nakai M., Hieda J.; *Development of new metallic alloys for biomedical applications*; Acta Biomaterialia 8 (2012) 3888-3903 doi:10.1016/j.actbio.2012.06.037.

[63] Braic V., Balaceanu M., Braic M., Vladescu A., Panseri S., Russo A.; *Characterization of multi-principal-element (TiZrNbHfTa)N and (TiZrNbHfTa)C coatings for biomedical applications*; Journal of the mechanical behavior of biomedical materials 10 (2012) 197-205 doi:10.1016/j.jmbbm.2012.02.020.

[64] Peighambardoust N.S., Alamdari A.A., Unal U., Motallebzadeh A.; *In vitro biocompatibility evaluation of Ti1.5ZrTa0.5Nb0.5Hf0.5 refractory high-entropy alloy film for orthopedic implants: Microstructural, mechanical properties and corrosion behavior*; Journal of Alloys and Compounds 883, (2021) 160786 doi:10.1016/j.jallcom.2021.160786.

[65] Kofstad, P.; *High Temperature Corrosion*; Elsevier, London, (1988) ISBN:1851661549.

[66] Gold, V.; *The IUPAC Compendium of Chemical Terminology*; International Union of Pure and Applied Chemistry (IUPAC), Research Triangle Park, NC, (2019) ISBN:0967855098.

[67] Bürgel, R.; Jürgen Maier, H.; Niendorf, T.; *Handbuch Hochtemperatur-Werkstofftechnik*; Vieweg+Teubner, Wiesbaden, (2011) ISBN:9783834813886.

[68] Shreir, L.L.; Burstein, G.T.; Jarman, R.A.; *Corrosion*; Butterworth-Heinemann, Oxford, (1994) ISBN:0750610778.

[69] University of Cambridge; *The interactive Ellingham diagram*, (2004-2022) doitpoms.ac.uk/tlplib/ellingham_diagrams/interactive.php; accessed: 12.08.2022.

[70] Crank, J.; *The Mathematics of Diffusion*, Oxford science publications; Oxford, Oxford University Press, (1986) ISBN:0198534116.

[71] Samsonov, G.V. (ed.); *Handbook of the Physicochemical Properties of the Elements*; Springer International Publishing, Cham, (2012).

[72] Strafford K.N., Towell J.M.; *The interaction of titanium and titanium alloys with nitrogen at elevated temperatures. I. The kinetics and mechanism of the titanium-nitrogen reaction*; Oxidation of Metals 10, (1976) 41-67 doi:10.1007/BF00611698.

[73] Baillieux J., Poquillon D., Malard B.; *Observation using synchrotron X-ray diffraction of the crystallographic evolution of α-titanium after oxygen diffusion*; Philosophical Magazine Letters 95, (2015) 245-252 doi:10.1080/09500839.2015.1014876.

[74] Vaché N., Monceau D.; *Oxygen diffusion modeling in titanium alloys: New elements on the analysis of microhardness profiles*; Oxidation of Metals 93 (2020) 215-227 doi:10.1007/s11085-020-09956-9.

[75] Okamoto H.; *Nb-O (Niobium-Oxygen). In: Massalski, T.B.; Okamoto, H.; Subramanian, P.R. et al.* (eds.): Binary alloy phase diagrams. ASM International. ASM International, Metals Park, Ohio, (1990).

[76] Okamoto H.; *O-Ta (Oxygen-Tantalum). In: Massalski, T.B.; Okamoto, H.; Subramanian, P.R. et al.* (eds.): Binary alloy phase diagrams. ASM International. ASM International, Metals Park, Ohio, (1990).

[77] Garg S.P., Krishnamurthy N., Awasthi A., Venkatraman M.; *The O-Ta (Oxygen-Tantalum) system*; Journal of Phase Equilibria 17, (1996) 63-77 doi:10.1007/BF02648373.

[78] Mosbacher M., Scherm F., Glatzel U.; *Oxygen diffusion kinetics of an advanced three step heat treatment for zirconium alloy ZrNb7*; Surface and Coatings Technology 339, (2018) 139-146 doi:10.1016/j.surfcoat.2018.02.015.

[79] Dickes D., Öztürk B., Völkl R., Galetz M.C., Glatzel U.; *Improving the adhesion of a hard oxide layer on Ti6Al4V by a three-step thermal oxidation process*; Advanced Engineering Materials (2021) p. 2100864 doi:10.1002/adem.202100864.

[80] Dong H., Li X.Y.; *Oxygen boost diffusion for the deep-case hardening of titanium alloys*; Materials Science and Engineering: A 280, (2000) 303-310 doi:10.1016/S0921-5093(99)00697-8.

[81] Frangini S., Mignone A., Riccardis F. de; *Various aspects of the air oxidation behaviour of a Ti6Al4V alloy at temperatures in the range 600–700 °C*; Journal of Materials Science 29 (1994) 714-720 doi:10.1007/BF00445984.

[82] Du H.L., Datta P.K., Lewis D.B., Burnell-Gray J.S.; *Air oxidation behaviour of Ti6Al4V alloy between 650 and 850°*; Corrosion Science 36, (1994) 631-642 doi:10.1016/0010-938X(94)90069-8.

[83] Dong H., Bloyce A., Morton P.H., Bell T.; *Surface engineering to improve tribological performance of Ti–6Al–4V*; Surface Engineering 13, (1997) 402-406 doi:10.1179/sur.1997.13.5.402.

[84] Güleryüz H., Cimenoğlu H.; *Effect of thermal oxidation on corrosion and corrosion-wear behaviour of a Ti-6Al-4V alloy*; Biomaterials 25 (2004) 3325-3333 doi:10.1016/j.biomaterials.2003.10.009.

[85] Guleryuz H., Cimenoglu H.; *Surface modification of a Ti–6Al–4V alloy by thermal oxidation*; Surface and Coatings Technology 192, (2005) 164-170 doi:10.1016/j.surfcoat.2004.05.018.

[86] Guleryuz H., Cimenoglu H.; *Oxidation of Ti–6Al–4V alloy*; Journal of Alloys and Compounds 472, (2009) 241-246 doi:10.1016/j.jallcom.2008.04.024.

[87] Xiong D., Yang Y., Deng Y.; *Bio-tribological properties of UHMWPE against surface modified titanium alloy*; Surface and Coatings Technology 228, (2013) S442-S445 doi:10.1016/j.surfcoat.2012.05.033.

[88] Lin N., Zhou P., Wang Y., Zou J., Ma Y., Wang Z., Tian W., Yau X., Tang B.; *Thermal oxidation of Ti6Al4V alloy with enhanced wear and corrosion resistance for oil and gas application: effect of temperature*; Surface Review and Letters 22, (2015) 1550033 doi:10.1142/S0218625X1550033X.

[89] Zhang Y., Ma G.-R., Zhang X.-C., Li S., Tu S.-T.; *Thermal oxidation of Ti-6Al–4V alloy and pure titanium under external bending strain: Experiment and modelling*; Corrosion Science 122, (2017) 61-73 doi:10.1016/j.corsci.2017.01.009.

[90] Cao L., Liu J., Wan Y., Yang S., Gao J., Pu J.; *Low-friction carbon-based tribofilm from poly-alpha-olefin oil on thermally oxidized Ti6Al4V*; Surface and Coatings Technology 337, (2018) 471-477 doi:10.1016/j.surfcoat.2018.01.057.

[91] Yazdi R., Ghasemi H.M., Abedini M., Wang C., Neville A.; *Oxygen diffusion layer on Ti–6Al–4V alloy: scratch and dry wear resistance*; Tribology Letters 67, (2019) 445 doi:10.1007/s11249-019-1214-3.

[92] Kumar S., Sankara Narayanan T., Ganesh Sundara Raman S., Seshadri S.K.; *Thermal oxidation of Ti6Al4V alloy: Microstructural and electrochemical characterization*; Materials Chemistry and Physics 119, (2010) 337-346 doi:10.1016/j.matchemphys.2009.09.007.

[93] Dong H., Bell T.; *Enhanced wear resistance of titanium surfaces by a new thermal oxidation treatment*; Wear 238, (2000) 131-137 doi:10.1016/S0043-1648(99)00359-2.

[94] Szota M., Lukaszewicz A., Kosinski K.; *The influence of parameters of heat treatment on thickens and roughness of oxide layers on titanium alloy Ti6Al4V*; Revista de Chemie 69, (2018) 2850-2853.

[95] Ashrafizadeh A., Ashrafizadeh F.; *Structural features and corrosion analysis of thermally oxidized titanium*; Journal of Alloys and Compounds 480, (2009) 849-852 doi:10.1016/j.jallcom.2009.02.079.

[96] Yazdanian M.M., Edrisy A., Alpas A.T.; *Vacuum sliding behaviour of thermally oxidized Ti–6Al–4V alloy*; Surface and Coatings Technology 202, (2007) 1182-1188 doi:10.1016/j.surfcoat.2007.05.069.

[97] Cao L., Wan Y., Yang S., Pu J.; *The tribocorrosion and corrosion properties of thermally oxidized Ti6Al4V alloy in 0.9 wt.% NaCl physiological saline*; Coatings 8, (2018) 285 doi:10.3390/coatings8080285.

[98] Vaché N., Cadoret Y., Dod B., Monceau D.; *Modeling the oxidation kinetics of titanium alloys: Review, method and application to Ti-64 and Ti-6242s alloys*; Corrosion Science, (2021) 109041 doi:10.1016/j.corsci.2020.109041.

[99] Bacroix B., Lahmari M., Inglebert G., Caron I.L.; *A modified oxygen boost diffusion treatment for Ti alloys and associated tribological properties with respect to biological environment*; Wear 271, (2011) 2720-2727 doi:10.1016/j.wear.2011.05.016.

[100] Zhou Y., Zhang Q.Y., Liu J.Q., Cui X.H., Mo J.G., Wang S.Q.; *Wear characteristics of a thermally oxidized and vacuum diffusion heat treated coating on Ti–6Al–4V alloy*; Wear 344-345, (2015) 9-21 doi:10.1016/j.wear.2015.10.015.

[101] Wang L., Zhang Q.Y., Li X.X., Cui X.H., Wang S.Q.; *Severe-to-mild wear transition of titanium alloys as a function of temperature*; Tribology Letters 53, (2014) 511-520 doi:10.1007/s11249-013-0289-5.

[102] Du H.L., Datta P.K., Lewis D.B., Burnell-Gray J.S.; *High-temperature corrosion of Ti and Ti-6Al-4V alloy*; Oxidation of Metals 45, (1996) 507-527 doi:10.1007/BF01046849.

[103] Motallebzadeh A., Peighambardoust N.S., Sheikh S., Murakami H., Guo S., Canadinc D.; *Microstructural, mechanical and electrochemical characterization of TiZrTaHfNb and Ti1.5ZrTa0.5Hf0.5Nb0.5 refractory high-entropy alloys for biomedical applications*; Intermetallics 113, (2019) 106572 doi:10.1016/j.intermet.2019.106572.

[104] Jayaraj J., Thinaharan C., Ningshen S., Mallika C., Kamachi Mudali U.; *Corrosion behavior and surface film characterization of TaNbHfZrTi high entropy alloy in aggressive nitric acid medium*; Intermetallics 89, (2017) 123-132 doi:10.1016/j.intermet.2017.06.002.

[105] Hruška P., Lukáč F., Cichoň S., Vondráček M., Čížek J., Fekete L., Lančok J., Veselý J., Minárik P., Cieslar M., Melikhova O., Kmječ T., Liedke M.O., Butterling M., Wagner A.; *Oxidation of amorphous HfNbTaTiZr high entropy alloy thin films prepared by DC magnetron sputtering*; Journal of Alloys and Compounds, (2020) 157978 doi:10.1016/j.jallcom.2020.157978.

[106] Sheikh S., Bijaksana M.K., Motallebzadeh A., Shafeie S., Lozinko A., Gan L., Tsao T.-K., Klement U., Canadinc D., Murakami H., Guo S.; *Accelerated oxidation in ductile refractory high-entropy alloys*; Intermetallics 97, (2018) 58-66 doi:10.1016/j.intermet.2018.04.001.

[107] Wenderoth M., Glatzel U., Völkl R.; *Experimental studies of internal oxidation in a Ni-Zr-Y alloy.* Schnapp, J.D. (ed.): Thüringer Werkstofftag 2002 – Vorträge und Poster. Thüringer Werkstofftag, Schriftenreihe Werkstoffwissenschaften Heft 17. Köster, Berlin, (2002) 210-215.

[108] Okano Y.; *Scanning Electron Microscopy. In:* The Surface Science Society of Japan (ed.): Compendium of surface and interface analysis, Springer eBook Collection. Springer, Singapur, (2018) 563-569.

[109] Sakamae H.; *Electron Probe Microanalysis. In:* The Surface Science Society of Japan (ed.): Compendium of surface and interface analysis, Springer eBook Collection. Springer, Singapur, (2018) 139-142.

[110] Kawai J.; *Total Reflection X-Ray Fluorescence. In:* The Surface Science Society of Japan (ed.): Compendium of surface and interface analysis, Springer eBook Collection. Springer, Singapur, (2018) 763-768.

[111] Chapon P., Gaiaschi S., Shimizu K.; *Glow Discharge Optical Emission Spectrometry. In:* The Surface Science Society of Japan (ed.): Compendium of surface and interface analysis, Springer eBook Collection. Springer, Singapur, (2018) 219-228.

[112] Unnam J., Shenoy R.N., Clark R.K.; *Oxidation of commercial purity titanium*; Oxidation of Metals 26, (1986) 231-252 doi:10.1007/BF00659186.

[113] Wilde M., Fukutani K.; *Nuclear Reaction Analysis. In:* The Surface Science Society of Japan (ed.): Compendium of surface and interface analysis, Springer eBook Collection. Springer, Singapur, (2018) 405-411.

[114] Amsel G., Béranger G., Gélas B. de, LACOMBE P.; *Use of the nuclear reaction O 16 (d, p)O 17 to study oxygen diffusion in solids and its application to zirconium*; Journal of Applied Physics 39, (1968) 2246-2255 doi:10.1063/1.1656538.

[115] Tomitori M.; *Atom Probe Field Ion Microscope. In:* The Surface Science Society of Japan (ed.): Compendium of surface and interface analysis, Springer eBook Collection. Springer, Singapur, (2018) 27-32.

[116] Nakamura M.; *X-Ray Photoelectron Spectroscopy. In:* The Surface Science Society of Japan (ed.): Compendium of surface and interface analysis, Springer eBook Collection. Springer, Singapur, (2018) 833-842.

[117] Waseda, Y.; Matsubara, E.; Shinoda, K.; *X-ray diffraction crystallography – Introduction, examples and solved problems*, Material Science Chemistry; Springer, Berlin, (2011) ISBN:978-3-642-16634-1.

[118] DIN EN ISO 26443:2016-09; *Fine ceramics (advanced ceramics, advanced technical ceramics) - Rockwell indentation test for evaluation of adhesion of ceramic coatings – German version EN ISO 26443:2016*.

[119] DIN EN ISO 4288:1998-04; *Geometrical product specifications (GPS) - Surface texture: Profile method - Rules and procedures for the assessment of surface texture – German version EN ISO 4288:1997*.

[120] DIN EN ISO 4287:2010-07; *Geometrical Product Specifications (GPS) - Surface texture: Profile method - Terms, definitions and surface texture parameters – German version EN ISO 4287:1998*.

[121] Galetz M.C., Seiferth S.H., Theile B., Glatzel U.; *Potential for adhesive wear in friction couples of UHMWPE running against oxidized zirconium, titanium nitride coatings, and cobalt-chromium alloys*; Journal of Biomedical Materials Research Part B: Applied Biomaterials 93B (2010) 468-475 doi:10.1002/jbm.b.31604.

[122] Galetz M.C., Glatzel U.; *Molecular deformation mechanisms in UHMWPE during tribological loading in artificial joints*; Tribology Letters 38, (2010) 1-13 doi:10.1007/s11249-009-9563-y.

[123] ISO 14243-3:2014-11; *Implants for surgery - Wear of total knee-joint prostheses - Part 3: Loading and displacement parameters for wear-testing machines with displacement control and corresponding environmental conditions for test*.

[124] DIN EN ISO 26424:2016-11; *Fine ceramics (advanced ceramics, advanced technical ceramics) - Determination of the abrasion resistance of coatings by a micro-scale abrasion test – German version EN ISO 26424:2016*.

[125] Senkov O.N., Scott J.M., Senkova S.V., Meisenkothen F., Miracle D.B., Woodward C.F.; *Microstructure and elevated temperature properties of a refractory TaNbHfZrTi alloy*; Journal of Materials Science 47, (2012) 4062-4074 doi:10.1007/s10853-012-6260-2.

[126] Dickes D., Öztürk B., Baier F., Berger P., George E.P., Völkl R., Galetz M.C., Glatzel U.; *Surface hardening of TiZrNbHfTa high entropy alloy via oxidation*; Corrosion Science, (2023) 111159 doi:10.1016/j.corsci.2023.111159.

[127] Qu J., Blau P.J., Howe J.Y., Meyer III H.M.; *Oxygen diffusion enables anti-wear boundary film formation on titanium surfaces in zinc-dialkyl-dithiophosphate (ZDDP)-containing lubricants*; Scripta Materialia 60, (2009) 886-889 doi:10.1016/j.scriptamat.2009.02.009.

[128] Poquillon D., Armand C., Huez J.; *Oxidation and oxygen diffusion in Ti–6Al–4V alloy: Improving measurements during SIMS analysis by rotating the sample*; Oxidation of Metals 79 (2013) 249-259 doi:10.1007/s11085-013-9360-8.

[129] Sefer, B.; *Oxidation and alpha-case phenomena in titanium alloys used in aerospace industry – Ti-6Al-2Sn-4Zr-2Mo and Ti-6Al-4V*, Licentiate thesis / Luleå University of Technology; Luleå University of Technology, Luleå, (2014) ISBN:978-91-7439-928-8.

[130] Ciszak C., Popa I., Brossard J.-M., Monceau D., Chevalier S.; *NaCl induced corrosion of Ti-6Al-4V alloy at high temperature*; Corrosion Science 110, (2016) 91-104 doi:10.1016/j.corsci.2016.04.016.

[131] Maeda K., Suzuki S., Ueda K., Kitashima T., Bhattacharya S.K., Sahara R., Narushima T.; *Experimental and theoretical study of the effect of Si on the oxidative behavior of Ti-6Al-4V alloys*; Journal of Alloys and Compounds 776, (2019) 519-528 doi:10.1016/j.jallcom.2018.10.291.

[132] Casadebaigt A., Hugues J., Monceau D.; *High temperature oxidation and embrittlement at 500–600 °C of Ti-6Al-4V alloy fabricated by Laser and Electron Beam Melting*; Corrosion Science 175, (2020) 108875 doi:10.1016/j.corsci.2020.108875.

[133] Dong E., Yu W., Cai Q., Cheng L., Shi J.; *High-temperature oxidation kinetics and behavior of Ti–6Al–4V Alloy*; Oxidation of Metals 88, (2017) 719-732 doi:10.1007/s11085-017-9770-0.

[134] Casadebaigt A., Hugues J., Monceau D.; *Influence of microstructure and surface roughness on oxidation kinetics at 500–600 °C of Ti–6Al–4V alloy fabricated by additive manufacturing*; Oxidation of Metals 90, (2018) 633-648 doi:10.1007/s11085-018-9859-0.

[135] Hertl C., Werner E., Thull R., Gbureck U.; *Oxygen diffusion hardening of cp-titanium for biomedical applications*; Biomedical Materials 5 (2010) p. 54104 doi:10.1088/1748-6041/5/5/054104.

[136] Rahmel A., Schütze M., Quadakkers W.J.; *Fundamentals of TiAl oxidation - A critical review*; Materials and Corrosion/Werkstoffe und Korrosion 46, (1995) 271-285 doi:10.1002/maco.19950460503.

[137] Bagot P., Radecka A., Magyar A.P., Gong Y., Bell D.C., Smith G., Moody M.P., Dye D., Rugg D.; *The effect of oxidation on the subsurface microstructure of a Ti-6Al-4V alloy*; Scripta Materialia 148, (2018) 24-28 doi:10.1016/j.scriptamat.2018.01.015.

[138] Schütze M.; *Stress Effects in High Temperature Oxidation.* Cottis, R.A. (ed.): Basic concepts, high temperature corrosion, Shreir's corrosionv. 1. Elsevier, (2010) 153-179.

[139] Huntz A.M., Schütze M.; *Stresses generated during oxidation sequences and high temperature fracture*; Materials at High Temperatures 12, (1994) 151-161 doi:10.1080/09603409.1994.11689481.

[140] Evans H.E.; *Stress effects in high temperature oxidation of metals*; International Materials Reviews 40, (1995) 1-40 doi:10.1179/imr.1995.40.1.1.

[141] Mantha L.S., MacDonald B., Mu X., Mazilkin A., Ivanisenko J., Hahn H., Lavernia E.J., Katnagallu S., Kübel C.; *Grain boundary segregation induced precipitation in a non equiatomic nanocrystalline CoCuFeMnNi compositionally complex alloy*; Acta Materialia 220, (2021) 117281 doi:10.1016/j.actamat.2021.117281.

[142] Lai, G.Y.; *High-temperature corrosion and materials applications*; ASM International, Materials Park, OH, (2008)) ISBN:9780871708533.

[143] Gorr B., Schellert S., Müller F., Christ H.-J., Kauffmann A., Heilmaier M.; *Current status of research on the oxidation behavior of refractory high entropy alloys*; Advanced Engineering Materials, (2021) 2001047 doi:10.1002/adem.202001047.

[144] Backman L., Gild J., Luo J., Opila E.J.; *Part I: Theoretical predictions of preferential oxidation in refractory high entropy materials*; Acta Materialia 197, (2020) 20-27 doi:10.1016/j.actamat.2020.07.003.

[145] Backman L., Gild J., Luo J., Opila E.J.; *Part II: Experimental verification of computationally predicted preferential oxidation of refractory high entropy ultra-high temperature ceramics*; Acta Materialia 197, (2020) 81-90 doi:10.1016/j.actamat.2020.07.004.

[146] Lo K.-C., Murakami H., Glatzel U., Yeh J.-W., Gorsse S., Yeh A.-C.; *Elemental effects on the oxidation of refractory compositionally complex alloys*; International Journal of Refractory Metals and Hard Materials 108, (2022) 105918 doi:10.1016/j.ijrmhm.2022.105918.

[147] Song B., Yang Y., Rabbani M., Yang T.T., He K., Hu X., Yuan Y., Ghildiyal P., Dravid V.P., Zachariah M.R., Saidi W.A., Liu Y., Shahbazian-Yassar R.; *In situ oxidation studies*

of high-entropy alloy nanoparticles; ACS nano 14 (2020) 15131-15143 doi:10.1021/acsnano.0c05250.

[148] Stepanov N.D., Yurchenko N., Zherebtsov S.V., Tikhonovsky M.A., Salishchev G.A.; *Aging behavior of the HfNbTaTiZr high entropy alloy*; Materials Letters 211, (2018) 87-90 doi:10.1016/j.matlet.2017.09.094.

[149] Wu Y., Wang Q., Lin D., Chen X., Wang T., Wang W.Y., Wang Y., Hui X.; *Phase stability and deformation behavior of TiZrHfNbO high-entropy alloys*; Frontiers in Materials 7, (2020) doi:10.3389/fmats.2020.589052.

[150] Wu H.H., Wisesa P., Trinkle D.R.; *Oxygen diffusion in hcp metals from first principles*; Physical Review B 94, (2016) doi:10.1103/PhysRevB.94.014307.

[151] Hornberger H., Randow C., Fleck C.; *Fatigue and surface structure of titanium after oxygen diffusion hardening*; Materials Science and Engineering: A 630, (2015) 51-57 doi:10.1016/j.msea.2015.02.006.

[152] Dao T.T., Pouletaut P.; *A hertzian integrated contact model of the total knee replacement implant for the estimation of joint contact forces*; Journal of Computational Medicine 2015 (2015) 1-9 doi:10.1155/2015/945379.

[153] Berthaud M., Popa I., Chassagnon R., Heintz O., Lavková J., Chevalier S.; *Study of titanium alloy Ti6242S oxidation behaviour in air at 560°C: Effect of oxygen dissolution on lattice parameters*; Corrosion Science 164, (2020) 108049 doi:10.1016/j.corsci.2019.06.004.

[154] Ye Y.X., Ouyang B., Liu C.Z., Duscher G.J., Nieh T.G.; *Effect of interstitial oxygen and nitrogen on incipient plasticity of NbTiZrHf high-entropy alloys*; Acta Materialia 199, (2020) 413-424 doi:10.1016/j.actamat.2020.08.065.

[155] Lindemann, U.; *Methodische Entwicklung technischer Produkte*; Springer Berlin Heidelberg, Berlin, Heidelberg, (2009) ISBN:9783642014222.

[156] Chang K.-H.; *Chapter 2 - Decisions in Engineering Design. In: Chang, K.-H.* (ed.): Design Theory and Methods using CAD/CAE – The Computer Aided Engineering Design Series, The Computer Aided Engineering Design Series. Elsevier Science, Burlington, (2014) 39-101.

[157] Chen Q., Li D.Y., Cook B.; *Is porosity always detrimental to the wear resistance of materials?—A computational study on the effect of porosity on erosive wear of TiC/Cu composites*; Wear 267, (2009) 1153-1159 doi:10.1016/j.wear.2008.12.058.

[158] Sinha A., Farhat Z.; *Effect of surface porosity on tribological properties of sintered pure Al and Al 6061*; Materials Sciences and Applications 06, (2015) 549-566 doi:10.4236/msa.2015.66059.

11 Acknowledgment

Even though the successful completion of this thesis is due to a personal strive and a considerable investment of working hours, it would never have been possible without the many people supporting me in both my private and working environments. Each and everyone deserves my thanks, which I will express individually and personally. However, this work contains contributions and input that explicitly enabled this thesis, helped to enrich the scope of this thesis, or improved this thesis in various ways. I am therefore glad and thankful to acknowledge:

The financial support of the German Research Foundation DFG (project number 270293189; GL 181/41-2 and GA 1704/12-2).

The input and feedback of the project team led by Prof. Dr.-Ing. Uwe Glatzel (University of Bayreuth, Metals & Alloys) and PD Dr.-Ing Mathias C. Galetz (DECHEMA-Forschungsinstitut, Materials and Corrosion) and the core team members Dr.-Ing. Rainer Völkl (University of Bayreuth, Metals & Alloys) and Beyza Öztürk (DECHEMA-Forschungsinstitut, Materials and Corrosion).

The provision of cold-rolled TiZrNbHfTa material by Easo P. George (Oak Ridge National Laboratory, Materials Science and Technology Division) and as-cast TiZrNbHfTa material by Dr.-Ing. Christian Gadelmeier (University of Bayreuth, Metals & Alloys).

The provision of EPMA oxygen mappings of oxidized TiZrNbHfTa used in Figure 35 and the experimental ball-on-disk tribometer results used in Figure 63 and Figure 64 by Beyza Öztürk (DECHEMA-Forschungsinstitut, Materials and Corrosion).

The provision of the experimentally determined XPS data of TiZrNbHfTa in various states as used in Figure 45 and Figure 54 by Felix Baier (University of Bayreuth, Experimental Physics XI) and the access to the XPS/UPS facility (PHI 5000 VersaProbe III system) at the Device Engineering KeyLab at the Bavarian Polymer Institute, University of Bayreuth.

The provision of experimentally determined NRA oxygen concentration-depth profile data of TiZrNbHfTa after oxidation as used in Figure 42 by Pascal Berger (Université Paris-Saclay, CEA, CNRS, NIMBE).

The provision of the experimentally determined APT data of matrix and precipitates in TiZrNbHfTa after two-step oxidation used in Figure 52, Figure 53, and Table 15 by Yujun Zhao in the group of Prof. Dr. Tong Li (Ruhr University Bochum, Institute for Materials).

The proofreading by Dr.-Ing. Felix Schleifer and feedback to selected sections by Jun. Prof. Dr.-Ing. Anke Silvia Ulrich and Dr.-Ing. Rainer Völkl (University of Bayreuth, Metals & Alloys).